

## ABSTRACT

CHENG, GUANGMING. In Situ Investigation of Deformation Mechanisms in Crystalline Nanowires. (Under the direction of Dr. Yong Zhu).

Nanowires (NWs) are among the most important building blocks for a wide range of nanotechnology applications. The operation and reliability of NW-based devices call for the investigation of the mechanical properties and deformation behaviors of NWs. In this thesis, we focus on the mechanical behaviors of three types of NWs, SiC, ZnO and Ag NWs, including fracture mechanism of SiC NWs, anelasticity of crystalline NWs, deformation mechanism of Ag NWs, and recoverable plasticity in twinned Ag NWs.

Quantitative mechanical characterization of SiC NWs reveals that the size effect on fracture strength of SiC NWs is attributed to the size-dependent defect density rather than the surface effect that is common for single crystalline NWs. The SiC NWs are synthesized using the vapor-liquid-solid process with growth direction of  $\langle 111 \rangle$ . They consist of three types of structures, pure face-centered cubic (3C) structure, 3C structure with an inclined stacking fault, and highly defective structure, in a periodic fashion along the NW length. The SiC NWs are found to deform linear elastically until brittle fracture. Their fracture origin is identified in the 3C structures with inclined stacking faults, rather than the highly defective structures. The fracture strength increases as the NW diameter decreases from 45 to 17 nm, approaching the theoretical strength of 3C SiC.

We report large anelastic behavior in single crystalline NWs. *In situ* bending tests of individual NWs showed that, upon removal of the bending load and instantaneous recovery of the elastic strain, a substantial portion of the total strain gradually recovers with time. We attribute the observed large anelasticity to stress-gradient-induced migration of point defects, as supported by electron energy loss spectroscopy measurements and also by the fact that no

anelastic behavior could be observed under tension. We model this behavior through a theoretical framework by point defect diffusion under high initial strain gradient and short diffusion distance, expanding the classic Gorsky theory. Finally, we show that ZnO single crystalline NWs exhibit a high damping merit index, suggesting crystalline NWs with point defects are promising for damping applications.

We reveal transition of deformation modes in bi-twinned Ag NWs with a single twin boundary (TB) running parallel to the NW length direction. Localized dislocation slip and detwinning-twinning deformation depend on the volume ratio between the two twin variants and the cross-sectional aspect ratio. Specifically, in bi-twinned Ag NWs with balanced grain volume ratios localized dislocation propagation across the entire cross-section lead to permanent slip and limited fracture strain, while in those with small volume ratios, twinning propagation takes place following a detwinning process leading to superplasticity through reorientation of the NW. Both experimental and theoretical results corroborated that interaction of multiple localized dislocations at the TB mainly governs the detwinning process. A criterion is proposed for determining the deformation modes in face-centered cubic metallic NWs containing an internal TB with certain cross-sectional aspect ratio.

Metallic NWs with internal TBs running parallel to the NW length exhibit unusual time-dependent mechanical behavior owing to the interaction of dislocations with TBs. *In situ* TEM tensile experiments show that bi-twinned Ag NWs undergo stress relaxation upon loading at a stress level close to the yield point and plastic strain recovery upon unloading. Both experimental and simulation results confirmed that stress relaxation originates from the nucleation of dislocations from the free surface, while strain recovery is due to the reverse motion of dislocations driven by the repulsive force from the TB. Marked difference was found

in the plasticity in bi- and penta-twinned Ag NWs in terms of the stress relaxation, strain recovery and the interaction between dislocations and TBs, which is attributed to the difference in their microstructures.

© Copyright 2016 Guangming Cheng

All Rights Reserved

In Situ Investigation of Deformation Mechanisms in Crystalline Nanowires

by  
Guangming Cheng

A dissertation submitted to the Graduate Faculty of  
North Carolina State University  
in partial fulfillment of the  
requirements for the degree of  
Doctor of Philosophy

Mechanical Engineering

Raleigh, North Carolina

2016

APPROVED BY:

---

Dr. Yong Zhu  
Committee Chair

---

Dr. Mohammed A. Zikry

---

Dr. Chih-Hao Chang

---

Dr. Elizabeth Dickey

## **DEDICATION**

To my wife, Haiyan Qian

To my two sweet babies, Alice C. Qian and Andrew C. Qian

## BIOGRAPHY

Guangming Cheng was born in Hanshan, Anhui, China. In July 2003, he received his bachelor degree in the Department of Material Science and Engineering from Hefei University of Technology. In January 2010, he obtained his first PhD degree in Materials Physics and Chemistry from Institute of Metal Research, Chinese Academy of Sciences, for his research on characterization of microstructure and electronic structure of Nb/Nb<sub>5</sub>Si<sub>3</sub> composites. In April 2010, he joined Dr. Yuntian Zhu's group as a postdoctoral scholar in the Department of Material Science and Engineering, North Carolina State University, working on irradiation-induced evolution of defects and microstructures in nanocrystalline body-centered cubic Mo. In September 2013, he started his second PhD program under the advisory of Dr. Yong Zhu in the Department of Mechanical and Aerospace Engineering, North Carolina State University, with research focus on *in situ* investigation of deformation mechanisms in crystalline nanowires.

## ACKNOWLEDGMENTS

First and foremost, I would like to express my sincere gratitude to my advisor Dr. Yong Zhu, who introduced me into the area of nanomechanics and nanotechnology, and shared with me his knowledge in this area. This work would not have been possible without his guidance and support.

I would like to thank my committee members, Dr. Chih-Hao Chang, Dr. Mohammed A. Zikry and Dr. Elizabeth Dickey for their insightful thoughts and suggestions on my research. The guidance and effort from all committee members are indispensable and greatly appreciated. Special thanks goes to Dr. Elizabeth Dickey for providing me valuable suggestions on improvement of my research works and communications with others.

Many thanks to Dr. Gunther Richter at Max Planck Institute for Intelligent Systems (Germany) for providing Ag NWs, Dr. Wei Lu at University of Michigan for providing Si NWs, Dr. Yi Gu at Washington State University for providing ZnO NWs, Dr. Hancheng Huang at Northeast University for providing SiC NWs and Dr. Wiley at Duke for providing Ag NWs. I would like to thank our collaborators, Mr. Sheng Yin, Dr. Chunyang Miao, Dr. Hamed Haftbaradaran, Prof. Huajian Gao at Brown University and Dr. Xiaoyan Li at Tsinghua University (China) for molecular dynamic simulations and theoretical modeling; Dr. Jing Li and Prof. Elizabeth C. Dickey at Dept. of Material Science and Engineering, NCSU for electron energy loss spectrum analysis; Dr. Xiaohan Sang at Oak Ridge National Lab, for the help of MATLAB codes for image processing.

I also would like to acknowledge the use of the Analytical Instrumentation Facility (AIF) at North Carolina State University, which is supported by the State of North Carolina

and the National Science Foundation (award number ECCS-1542015). Many thanks should be delivered to Dr. Yang Liu, Dr. Roberto Garcia, Dr. Chuanzhen Zhou, Dr. Fred Stevie and Dr. Charles Mooney for offering the technical services, training and managements for all the important experimental resources to my research projects, and Oak Ridge National Lab for allowing me to use their instrument and providing technique support.

I would like to acknowledge the financial support by the National Science Foundation (NSF) under Award Nos. CMMI-1030637 and 1301193.

I would like to express my deepest gratitude to Dr. Yuntian Zhu at Dept. of Material Science and Engineering, NCSU for his guidance and patience in helping to foster my interests as a scientist and for the use of the instruments in his lab to process the experiments during my graduate study.

I would like to thank my previous and current colleagues in our research group, Dr. Qinquan Qin, Dr. Tao Jiang, Dr. Tzu-Hsuan Chang, Dr. Shanshan Yao, Mr. Russell Mailen, Ms. Amanda Myers, Mr. Felipe Robles Poblete, Mr. Zheng Cui, Mr. Jianxun Cui and Mr. Chengjun Li. I am lucky to be in a lab with great people like you and I enjoyed the time with you all. Special appreciation to Dr. Qinquan Qin, he is the guide to introduce me into our group and the pioneer to work on the in situ TEM stage. With his help, I have learnt how to manipulate a so tiny object (nanowire) in a scanning electron microscope. Special thanks to Dr. Tzu-Hsuan Chang. I am going to miss all the hard time and pleasant time we went through in the experiments we did together.

I would like to thank Dr. Weiwei Jian, Dr. Jun Wang, Dr. Weizong Xu, Dr. Xiaolong Ma, Mr. Xiaotian Fang, and Mr. Haotian Deng, for their very kind help, excellent advice,

collaboration, and stimulating discussions during my graduate study. I wish to thank all my dear friends inside and outside North Carolina State University for bringing me so many fond memories during my graduate life.

Last but not least, I would like to thank my family for their unconditional love and support. Thanks from the bottom of my heart to my wife, Haiyan Qian. I could never have accomplished this without her. And I would like to bring my best wishes to my two sweet babies, Alice C. Qian and Andrew C. Qian, to grow up healthy and happy. I would also like to bless my family members in China. Many thanks to their supports and hope they have a healthy and happy life.

# TABLE OF CONTENTS

LIST OF TABLES .....	xi
LIST OF FIGURES .....	xii
CHAPTER 1 INTRODUCTION.....	1
1.1 One Dimensional Nanomaterials .....	1
1.2 Nanowire Synthesis .....	2
1.2.1 SiC NWs .....	6
1.2.2 Ag NWs .....	9
1.2.3 ZnO NWs .....	8
1.3 Mechanical Characterization .....	12
1.3.1 Size Dependent Mechanical Behavior in NWs.....	12
1.3.2 Anelasticity in Crystalline NWs .....	14
1.3.3 Deformation Mechanisms in Metallic NWs .....	18
1.3.4 Reversible Plasticity in Twinned Metallic NWs.....	21
1.4 <i>In Situ</i> Nanomechanical Testing Techniques.....	24
1.4.1 Manipulator and Sensor Based Techniques .....	25
1.4.2 MEMS Based Techniques.....	28

CHAPTER 2 MECHANICAL PROPERTIES OF SILICON CARBIDE NANOWIRES: EFFECT OF SIZE-DEPENDENT DEFECT DENSITY .....	33
2.1 Introduction.....	33
2.2 Materials and Methods.....	35
2.2.1 Sample Synthesis and Characterization .....	35
2.2.2 <i>In Situ</i> SEM Mechanical Testing .....	36
2.3 Results.....	36
2.4 Conclusions.....	47
CHAPTER 3 LARGE ANELASTICITY AND ENERGY DISSIPATION IN SINGLE CRYSTALLINE NANOWIRES .....	48
3.1 Introduction.....	49
3.2 Materials and Methods.....	49
3.2.1 Synthesis of ZnO and Si NWs .....	49
3.2.2 <i>In Situ</i> SEM Testing.....	50
3.2.3 TEM, HRTEM and STEM/EELS Experiments.....	50
3.2.4 Theoretical Model .....	50
3.3 Results.....	51
3.4 Conclusions.....	63

CHAPTER 4	TWINNING, DETWINNING AND SUPERPLASTICITY IN CRYSTALLINE METAL NANOWIRES .....	64
4.1	Introduction.....	65
4.2	Materials and Methods.....	67
4.2.1	Sample Synthesis and Characterization .....	67
4.2.2	<i>In Situ</i> TEM Mechanical Testing.....	67
4.2.3	MD simulations.....	69
4.3	Results.....	70
4.3.1	NW Morphology and <i>In Situ</i> TEM Tensile Testing .....	70
4.3.2	Three Deformation Modes .....	73
4.3.3	Effects of Volume Ratio and Cross-sectional Aspect Ratio .....	82
4.3.4	Effect of Twin Boundaries .....	85
4.4	Conclusions.....	87
CHAPTER 5	RECOVERABLE PLASTICITY IN BI-TWINNED SILVER NANOWIRES	89
5.1	Introduction.....	89
5.2	Materials and Methods.....	92
5.2.1	Sample Synthesis and Characterization .....	92

5.2.2 <i>In Situ</i> TEM Mechanical Testing .....	92
5.2.3 MD Simulations .....	93
5.3 Results.....	94
5.3.1 Characterization of Bi-twinned NWs.....	94
5.3.2 Stress Relaxation in Bi-twinned NWs .....	96
5.3.3 <i>In Situ</i> Observation of Dislocation Nucleation and Retraction.....	100
5.4 Discussions .....	104
5.5 Conclusions.....	108
CHAPTER 6 CONCLUSIONS AND FUTURE WORKS .....	110
6.1 Conclusions.....	110
6.2 Future Works .....	113
REFERENCES .....	116

## LIST OF TABLES

<b>Table 4.1</b> Important features on the GSF curves for various FCC metals .....	82
<b>Table 4.2</b> Mechanical properties of single crystalline, bi- and penta-twinned Ag NWs under uniaxial tensile testing. Note that all the three type NWs have closed cross-sectional areas corresponding to a diameter ranging from 95-120 nm (treated as round shape) so as to avoid the size dependent effect on the Young's modulus .....	86
<b>Table 4.3</b> Summary of the mechanical behaviors of single crystalline, bi- and penta-twinned Ag NWs under uniaxial tensile testing.....	87

## LIST OF FIGURES

- Figure 1.1** Schematic of VLS growth of Si NWs. A Au/Si liquid droplet is first formed above the eutectic temperature (363 °C) of Au and Si. The continued feeding of Si in the vapor phase into the liquid alloy causes oversaturation of the liquid alloy, resulting in nucleation and directional NW growth. [21] ..... 4
- Figure 1.2** Schematic illustration of major experimental steps involved in the preparation of Ag NWs through a polyol process with Pt nanoparticles as the seeds: (A) Formation of bimodal Ag nanoparticles through heterogeneous nucleation on Pt seeds and homogeneous nucleation; (B) evolution of rod-shaped Ag nanostructures as directed by the capping reagent, PVP; and (C) growth of the Ag nanorods into NWs at the expense of small Ag nanoparticles. [55] ..... 5
- Figure 1.3** SEM images of Cu whiskers. (a) Nominal film thicknesses of 45 nm Cu were thermally evaporation deposited at 650 °C with a nominal deposition rate of 0.05 nm/s. The NWs shown in this micrograph have a maximum length of 10  $\mu$ m, and the diameters vary from 30 to 100 nm. (b) NWs formed on one of the cleavage planes. The NWs are free-standing and appear perpendicular to the surface. [38] . 6
- Figure 1.4** (a) SEM image of SiC NWs, with a cross-sectional view in the inset. (b) Bright field TEM image of a SiC NW in three stages (center), with transitions shown at the two corners. [75] ..... 7

**Figure 1.5** Schematic showing the growth mechanism of ZnO NWs, (b) SEM image of ZnO NWs grown on Si (100) substrate. [93] ..... 9

**Figure 1.6** (a) SEM image showing single crystalline or bi-twinned Ag NWs on Si substrate. (b) TEM image of single crystalline Ag NW with growth direction of  $\langle 110 \rangle$ . Scale bar, 200 nm. Right and left insets (scale bar, 100nm) in (b) show the selected area electron diffraction (SAED) pattern taken from  $\langle 110 \rangle$  zone axis and the hexagonal cross-sectional shape from SEM observation, respectively. [102] ..... 10

**Figure 1.7** (a) SEM image showing penta-twinned Ag NWs. (b) TEM image of penta-twinned Ag NWs showing five-fold twinned structure. Scale bar, 200nm. Right and left insets (scale bar, 20nm) in (b) display the corresponding SAED pattern and the pentagonal cross-sectional shape, respectively. [102] ..... 11

**Figure 1.8** (a) Strength plotted as a function of whisker diameter and compared to reported values of strength of pure Cu single crystalline small scale specimens. [38, 109-112] (b) Fracture strength of SiC NWs and whiskers as a function of the diameter. [113-118] ..... 13

**Figure 1.9** (a) Modified Young's modulus as a function of NW diameter. The measured Young's modulus was normalized by the bulk modulus of 84 GPa. [126] (b) Young's modulus versus diameter of ZnO NWs from both tension and buckling tests. The fitting curves from the core-surface model (solid) and the core-shell model (dash) are also plotted. Inset shows the schematic of both models. [127] ..... 14

**Figure 1.10** (a) A schematic illustration of the Gorsky effect. (b) Time dependence of the anelastic strain at different temperatures (Ta + 4.3 at%H). [136]..... 16

**Figure 1.11** A series of TEM images showing the anelastic behavior of a GaAs NW with a diameter of ~25 nm. (a) Before deformation and (b) during deformation, bending contours are marked with arrows. (c) Immediately after the external stress was completely released. Contrast variation is marked by arrows and the gap between the current and original positions of the NW tip is indicated by two dotted arrows. (d,e) The NW gradually reverted to its original shape. Dotted ellipses mark the region for contrast comparison. (f) At the instant when the NW completely returned to its original shape. The inset in (f) shows the whole length of the NW. Scale bar, 200 nm. [139]..... 17

**Figure 1.12** TEM images of a Au NW under the tensile deformation. (a) Two nanotwins initially nucleated during the plastic deformation. (b) High-resolution TEM (HRTEM) image magnified from the magenta square in (a). The twin is composed of two SFs. (c) TEM micrograph showing a twin extended to 1 μm length by twin propagation. (d) HRTEM image magnified from the cyan square in (c), showing a clear TB along the yellow line. (e,f) SAED patterns acquired from two blue dotted circles in (c), the NW lattice is changed from an original <110> (e) to a twinned <100> (f). [151]..... 19

**Figure 1.13** Tensile testing of individual Cu whiskers (a) SEM micrograph of whisker mechanical testing configuration. Whiskers are gripped by e-beam deposited Pt

weldments, the force applied on the specimen is measured by either a poly-Si flexure beam apparatus or a capacitive based transducer, and the local strain is measured by digital image correlation of SEM micrographs obtained during testing. (b,c) SEM micrographs of fracture surfaces of deformed whiskers showing shear (b) and brittle (c) failure. [38] ..... 20

**Figure 1.14** (a) Representative stress-strain curves under repeated unload–reload cycles of a penta-twinned Ag NW with diameter of 85 nm. The strain recovery is defined as the difference between the strain at zero stress if ideal elastic unloading happens (dashed lines) and the actual strain at zero stress. [181] (b) A stress-strain curve for a penta-twinned Ag NW (120 nm in diameter). Note that in both cases the relaxation and recovery steps took 15 min each. [102]..... 23

**Figure 1.15** Experimental evidence of reversible plastic deformation. (a) As the strain increased to 2.7%, the loading process was stopped and the defect was imaged. Note the black arrow as a point of reference for subsequent images. (b) Keeping the same magnification, unloading is performed, leading to the disappearance of the defect. Further loading (c) leads to the nucleation of the defect at the same location. Scale bars, 20 nm. [181] ..... 23

**Figure 1.16** (a) Schematic of a nanomanipulator in SEM chamber. (b) Picking-up a NW by the sharp W tip. .... 26

**Figure 1.17** (a–c) A series of SEM images taken during the tensile test for a Si NW with diameter of 23 nm. Inset of (a): High resolution SEM image of the NW for strain

measurements. (d) SEM image showing that fracture occurs on the NW when the load was applied to a certain value. [2]..... 27

**Figure 1.18** (a) A tensile MEMS based device with co-fabricated thin film sample. Image showing the device glued to (b) a piezo-actuator and (c) mounted on two pins of a TEM straining stage. [212] ..... 29

**Figure 1.19** SEM image of a MEMS based device for mechanical testing. The device includes a V-shaped thermal actuator, a load sensor, and specimen testing region. [201] .. 30

**Figure 1.20** (a) SEM image of a MEMS based device for mechanical testing. The device includes a V-shaped thermal actuator, a load sensor, and specimen testing region. [216] (b) SEM image of a MEMS based thermomechanical testing platform including an on-chip heater based on Joule heating. The device that consists of three parts: comb drive actuator, capacitive load sensor, and heater. (c) Magnified view of the heater as boxed in (b). The arrows indicate the current direction. [219]..... 32

**Figure 2.1** (a) Low-magnified TEM image of a large number of randomly oriented SiC NWs. (b) Histogram of the NW diameter distribution (8–64 nm). (c) Raman spectrum of SiC NWs. .... 37

**Figure 2.2** (a) A low magnification TEM image of an individual SiC NW with the growth direction of  $\langle 111 \rangle$ , the 3C structure with an inclined SF, highly defective structure and pure 3C structure are marked by I, II and III, respectively, and are separated by dashed lines. (b) HRTEM observation of the NW containing 3C structure with a  $19.47^\circ$  SF (segment A) and high-defective structures (segment B), corresponding to

the boxed area in panel (a). Insets are the FFT diffraction patterns taken from areas A and B. Note that a  $19.47^\circ$  SF is present in the 3C segment, marked as SF- $19.47^\circ$ .

(c) A magnified HRTEM image of the highly defective structure corresponding to the boxed area in (b) showing nanotwins, intrinsic SFI and extrinsic SFII in the NW.

..... 39

**Figure 2.3** Bright-field TEM images of SiC NWs with a diameter of 18 and 41 nm in (a) and (b), respectively. Three types of structures, pure 3C structure, 3C structure with a  $19.47^\circ$  SF and highly defective structure, can be seen.  $19.47^\circ$  stacking faults are marked by the blue arrows. .... 40

**Figure 2.4** (a) The MEMS stage used for *in situ* SEM tensile testing of SiC NWs. Inset shows a NW bridged between the actuator and the load sensor. (b) Representative stress – strain curves of SiC NWs. The curve for the NW of 35 nm in diameter includes multiple loading and unloading, showing linear elastic behavior and brittle fracture. Inset shows the fracture surface of a SiC NW. (c) Fracture strength of SiC NWs and whiskers as a function of the diameter. (d) Defect density as a function of NW diameter. Note that the defect density is defined as an average volume percentage of defect parts in a randomly selected segment with a length of 2  $\mu$ m (at least 5 data in each column with a bin size of 10 nm). The range between the dot lines corresponds to the diameter range tested in this work (17-45 nm). .... 41

**Figure 2.5** (a) Low-magnification TEM image of the fracture surface of a SiC NW. (b) HRTEM image of the fracture surface of the SiC NW, corresponding to the marked

area in (a). The loading direction is along the  $\langle 111 \rangle$  direction. The  $19.47^\circ$  SF is labeled as SF- $19.47^\circ$ . Similar fracture surfaces were observed other NWs tested (see the Supporting Information)..... 44

**Figure 2.6** Bright-field TEM images show the fracture surfaces of SiC NWs. The fractures were always in the 3C segments with  $19.47^\circ$  stacking faults (marked by the blue arrows). (a) corresponds to the fracture surface in the text. (b,c) are two additional examples of the fracture surfaces. Insets in (b,c) show the overview of the broken NWs attached on the cantilevers..... 45

**Figure 3.1** *In situ* SEM bending test of an individual ZnO NW. (a) Experimental setup showing an individual ZnO NW that was bent between a MEMS stage (right) and a nanomanipulator tip (left). Scale bar, 100  $\mu\text{m}$ . (b) A sequence of SEM images showing the recovery process of a ZnO NW after the bending load was removed. Scale bar, 2  $\mu\text{m}$ ..... 52

**Figure 3.2** Recovery and damping behaviors of a ZnO NW. (a) Anelastic strain as a function of recovery time for six different durations of holding time. The NW diameter was 54 nm and the initial bending strain was 1.94%. (b) Anelastic strain as a function of recovery time for five different initial bending strains. The holding time was 15 minutes in all five cases. Solid lines in both (a) and (b) represent the fitting data from finite element analysis. Error bars for strain measurement in (a) and (b) were  $\sim 5.4\%$ . (c) Normalized anelastic strain (anelastic strain divided by elastic strain) as a function of recovery time for five ZnO NWs in diameters of 38, 50, 54, 56 and 65

nm with the same holding time of 15 minutes. (d) The maximum anelastic strain as a function of the initial strain for the five ZnO NWs. The holding time was 15 minutes in all cases. Note how, for larger initial strains, the relationship becomes nonlinear. (e) Stress-strain curve of a ZnO NW under tension. (f) Force-displacement curve of a ZnO NW under compression (buckling)..... 53

**Figure 3.3** Anelastic strain as a function of recovery time for different initial bending strains.

In (a), the anelastic strain almost totally recovered (> 98%) within the time of 40 minutes. The NW diameter in (a), (b) and (c) was 54, 38 and 56 nm, respectively. The holding time was 15 min. Solid lines in panels (b) and (c) represent the fitting data from finite element analysis. .... 54

**Figure 3.4** Time-dependent beam curvature for a NW with diameter of 54 nm and initial strain

of 1.75% during bending (with a constant total curvature) and release. The NW is held for 900 s at constant total curvature after the initial strain is applied. The red line ( $\kappa$ ) indicates the total curvature of the NW, while the green ( $\kappa_1$ ) and blue ( $\kappa_2$ ) lines indicate the curvatures induced by non-uniform distributions of type 1 and type 2 defects, respectively. The magenta line is the curvature ( $\kappa_e$ ) due to the elastic part. .... 57

**Figure 3.5** Microstructure and relationship between oxygen difference and bending strain of a

ZnO NW. (a) Overview of an individual ZnO NW of 37 nm in diameter with growth direction of  $\langle 0001 \rangle$ . Inset shows the corresponding SAED pattern, at the zone axis of  $\langle 11\bar{2}0 \rangle$ . Scale bar, 100 nm. (b) HRTEM image showing a perfect atomic

arrangement in the close-packed layers of  $\{0001\}$ . Inset shows the atomic model of a ZnO unit cell. Scale bar, 2 nm. (c) HAADF-STEM image showing a bent NW for EELS analysis. Scale bar, 0.5  $\mu\text{m}$ . (d) Bending strain as a function of positions in the bent ZnO NW. (e) EELS analysis showing the difference in oxygen concentration between outer and inner sides of the bent ZnO NW at different positions. Position #0 was taken from a straight part with zero bending strain. Error bars are from the variation in stoichiometry ( $\sim 0.5$  at.%). (f) Linear relationship between the difference in oxygen concentration (between outer and inner sides) and the total bending strain and the anelastic strain. .... 58

**Figure 3.6** Mechanical behaviors of p-doped Si NWs under bending and compression. (a) Anelastic strain as a function of recovery time for six different durations of holding time. (b) Force-displacement curve of a p-doped Si NW under compression (buckling). .... 62

**Figure 4.1** A comb-drive-actuated MEMS based system for in situ TEM tensile test. (a) Comb-drive-actuated MEMS based device for tensile test. (b) TEM image showing a NW mounted on the device. Two local markers are deposited on the NW surface for displacement (or strain) measurement. .... 68

**Figure 4.2** Characterization of crystalline Ag NWs. (a,b) Schematic drawings of bi-twinned and single crystalline NWs, respectively. (c,d) Cross-sectional TEM images of bi-twinned and single crystalline NWs, respectively. Scale bar, 20 nm. (e) A cross-

sectional HRTEM image of a bi-twinned Ag NW. Inset in (e) is the corresponding selected area electron diffraction (SAED) pattern. Scale bar, 1 nm. .... 71

**Figure 4.3** Mechanical response and microstructure evolution of crystalline Ag NWs under *in situ* TEM tensile test. (a-c) Engineering stress-strain curves of bi-twinned and single crystalline Ag NWs under uniaxial loading-unloading. Insets in (a-c) are the corresponding cross-sectional images of the tested NWs (cut from the undeformed part after the test). Scale bar, 20 nm. (d-f) Snapshots of microstructure evolution of bi-twinned and single crystalline Ag NWs during the loading-unloading processes. The five snapshots corresponding to the stress-strain change are marked in (a-c). The loading direction is  $\langle 110 \rangle$ , which is also the length (or growth) direction of the NWs. Partial dislocations are marked by blue arrows and planar sliding by green arrows. Scale bar, 100 nm. The viewing directions are from the 110 zone axis of the small twin variant in (d), the large twin variant in (e) and the whole grain in (f), which are marked by the yellow arrows in the insets in (a-c), respectively. .... 72

**Figure 4.4** Dislocation slip dominated deformation in bi-twinned Ag NWs. (a) A magnified TEM image showing stacking faults left in the small twin variant at on-zone condition. The surface edge of the small twin variant is marked by the dashed line. Scale bar, 20 nm. (b) Snapshots from MD simulations showing nucleation, propagation of partial dislocations and interaction between the partial and the TB in bi-twinned Ag NWs. (c) Illustration of a double Thompson tetrahedron on the coherent 111 TB in bi-twinned NWs. The front tetrahedron at the front of the TB

represents the matrix slip systems in the dominant twin variant, while the back one represents twin slip systems in the small twin variant. .... 75

**Figure 4.5** Illustration of detwinning-twinning deformation in bi-twinned Ag NWs. (a) A perfect TB in the bi-twinned NW before loading. (b) Detwinning of the bi-twinned NW above a critical load. Note that only HCP atoms are made visible in (a,b). (c) Nucleation of a single crystalline phase in the bi-twinned NW, the side surfaces being reoriented from (111) to (100). (d) Internal structure of the detwinned NW. The FCC atoms have been made transparent. (e) Cross-section of the bi-twinned phase with axial direction of  $\langle 110 \rangle$ . (f) Detailed structure of the newly formed GBs during the detwinning process. (g) Cross-section of the single crystalline phase with axial direction reoriented to  $\langle 001 \rangle$ . (h,i) Fracture morphology of detwinning dominated bi-twinned Ag NWs from experimental and simulation investigations, respectively. A SAED pattern in the inset of (h) indicates the twin relationship between the newly formed single crystalline phase and the original dominant twin variant in the bi-twinned phase. .... 77

**Figure 4.6** MD simulcations showing dislocation evolution for detwinng-twinning deformation in bi-twinned NW. (a-d) Snapshots from MD simulations showing detwinning processes in a bi-twinned NW with small volume ratio. (e) Illustration of an extended jog formed with a new partial  $\delta C$  in plane  $ABC$  for detwinning... 78

**Figure 4.7** Twinning deformation in single crystalline Ag NWs. (a) A high-resolution TEM image of defective structures (nanotwins and SFs) in the deformed part of a single

crystalline Ag NW after the *in situ* tensile testing. Scale bar, 2nm. Insets in (a) are the cross-sectional images of single crystalline Ag NW before and after deformation. Scale bar, 20 nm. (b) Snapshots from MD simulations showing the generation of SFs and nanotwins during the twinning deformation in a single crystalline Ag NW. Leading partials for twinning propagation and SFs or nanotwinns are marked by red and blue arrows, respectively. .... 80

**Figure 4.8** Transition of deformation mechanisms in bi-twinned Ag NWs. (a) Energy difference associated with the detwinning process as a function of the twin volume ratio for a sample with fixed W and H. Inset in (a) shows the cross-section of a typical bi-twinned NW in MD simulation and its corresponding geometrical parameters. (b) The contour plot of energy difference in the detwinning process as a function of  $H/W$  and twin volume ratio  $r$ , along with the simulation and experimental data. For simulation results: the black squares stand for the slip dominated deformation mode, the red rhombuses stand for the detwinning-twinning deformation mode and the blue rhombuses stand for the transitional deformation mode. For experiment data: solid black squares stand for the slip dominated deformation mode and solid red rhombuses stand for the detwinning-twinning deformation mode. .... 83

**Figure 5.1** Microstructure characterization of Ag NWs. (a) SEM image of Ag NWs on Si substrate. Scale bar, 5  $\mu\text{m}$ . (b) Size distribution of Ag NWs.  $\langle 110 \rangle$  oriented bi-twinned NWs are dominant in the examined 113 NWs. (c,d) Schematic drawings of

bi-twinned and single crystalline Ag NWs and corresponding cross-sectional TEM images, respectively. Scale bar, 20 nm. (e,f) Dark- and bright-field TEM images of a bi-twinned Ag NW from longitudinal view. Inset in (e) is the corresponding SAED pattern taken from  $\langle 001 \rangle$  zone axis. Scale bar, 100 nm..... 96

**Figure 5.2** *In situ* measurements of stress and strain evolutions in a bi-twinned Ag NW. (a) Stress-strain curve for the bi-twinned Ag NW under two cycles of loading-relaxation-unloading processes. The relaxation step took 15 minutes. (b) Relaxation curves for the bi-twinned Ag NW. Solid and open symbols correspond to the strain-time and stress-time relationships, respectively. Square and circle symbols correspond to high and low initial stress levels, respectively. .... 98

**Figure 5.3** MD simulation of stress relaxation and strain recovery in a bi-twinned Ag NW. (a) Stress-strain curve of the full loading-relaxation-unloading process. Inset in (a) is an atomic model viewed from transverse and longitudinal direction. (b) Snapshots of partial dislocation nucleation during loading process. (c) Snapshots of partial dislocation retraction during unloading process. Note that only red hexagonal closed packed atoms are shown here and solid lines are dislocation lines by DXA algorithm. .... 100

**Figure 5.4** Mechanical response and microstructure evolution of a bi-twinned Ag NW under *in situ* TEM tensile testing. (a) Stress-strain curve for the bi-twinned Ag NW without a holding process. (b) Microstructure evolution during the load-unload process. (c) Stress-strain curved for the bi-twinned Ag NW with a holding process. The

relaxation step took 5 minutes. (d) Microstructure evolution during the load-hold-unload process. The location of partial dislocations and planar sliding in the NW are marked by blue and green arrows, respectively. Scale bar, 100 nm. .... 102

**Figure 5.5** Mechanical response and microstructure evolution of a single crystalline Ag NW under *in situ* TEM tensile testing. (a) Stress-strain curve for the single crystalline Ag NW. (b) Microstructure evolution during the load-unload process. Permanent planar sliding in the NW is marked by the green arrows. Scale bar, 100 nm. .... 103

**Figure 5.6** Stress-strain curves for the tested NWs in Figure 5.2, 4.4 and 4.5, respectively. (a,b) from bi-twinned NWs. (c) from single crystalline Ag NW. Insets in (a-c) show the cross-sectional TEM images of the tested NWs. All scale bars, 20 nm..... 104

**Figure 5.7** High resolution STEM images shows the atomic alignments from the cross-sectional view of bi and penta-twinned Ag NWs. (a) a bi-twinned Ag NW; (b) a penta-twinned NW. Internal defects (SFs and partials) distributed along the TBs in the penta-twinned Ag NW are marked by the arrows. The insets in (a,b) are the corresponding SAED patterns. All scale bar, 2 nm. .... 106

**Figure 5.8** *In situ* measurements of stress and strain evolutions in a penta-twinned Ag NW (120 nm in diameter). (a) Stress-strain curve for the NW under two cycles of loading-relaxation-unloading-recovery process. The relaxation and recovery steps took 15 minutes. (b) Relaxation curves for the NW at different stress level. Solid and open symbols correspond to the strain-time and stress-time relationships,

respectively. Diamond and triangle symbols correspond to low and high initial stress levels, respectively. .... 107

# CHAPTER 1

## INTRODUCTION

### 1.1 One Dimensional Nanomaterials

One dimensional (1D) nanomaterials such as nanowires (NWs) are widely regarded as among the most important building blocks of bottom-up nanotechnologies owing to their outstanding mechanical properties in addition to electrical, thermal and optical properties. [1-13] As such, they have been demonstrated in a broad range of applications including flexible/stretchable electronics [14-16], optoelectronics [17], energy harvesting and storage [5, 6, 8], ultrasensitive sensors [18, 19], and nanoelectromechanical systems [20, 21]. For examples, Ag NWs are being investigated as the conductive elements in flexible electronic systems. Because of their high conductivity and ease of synthesis, they have been employed in diverse applications such as high-conductivity flexible interconnects, mechanically tunable antennas, and strain sensors. [22-24] By taking advantage of the superior mechanical properties and piezoelectric property of ZnO NWs, a ZnO NW-based nanogenerator has been developed, which can convert ambient vibration, hydraulic energy, and mechanical movement to electricity. [8, 25] Si NWs with rough surfaces can be essentially thermal insulators, but with good electrical conductivity. [26, 27] They can be used as excellent thermoelectric materials in solar cells for converting heat to electricity. [28]

The operation and reliability of the NW-based devices call for a more thorough understanding of the mechanical behaviors of NWs. Due to the size refinement, surface, internal defects such as point defects (vacancy and interstitial) and grain boundaries (including

twin boundaries, TBs) are the main factors to affect the mechanical behaviors of 1D nanomaterials. Size and surface effects are dominant for these small volume materials as the characteristic dimension approaches sub-100 nm. [29-32] On the other hand, as-synthesized NWs typically possess different types of defects such as TBs and stacking faults (SFs). [2, 33] Thus it is of particular interest to study how preexisting defects can affect the mechanical behaviors of NWs.

In this thesis, we focus on the mechanical behaviors of three types of NWs, SiC, ZnO and Ag NWs. We emphasize on the nanomechanics revealed by *in situ* nanomechanical testing under scanning electron microscope (SEM) or transmission electron microscope (TEM), including fracture mechanism of SiC NWs, anelasticity of ZnO NWs, deformation mechanisms of Ag NWs and recoverable plasticity in twinned Ag NWs.

## **1.2 Nanowire Synthesis**

Fabrication of NWs with well-controlled surface, orientation, and size is the first step in the development of NW-based devices. NWs can be prepared by a variety of methods, which can be generally categorized as top-down or bottom-up approaches. [9, 21, 34-40] In the top-down approaches, the NW features are patterned at the surface of bulk materials, such as Si wafers, by a combination of lithography, doping, etching and deposition. [9, 21, 39, 41, 42] Bottom-up approaches produce 1D nanostructures via directed self-assembly of atoms from source materials. [43] They have been widely used for the growth of NWs, producing NWs with relatively smooth surfaces, which can be difficult to achieve using top-down approaches.

The most widely used NW synthetic methods for bottom-up approaches are vapor phase synthesis such as the dominant nanocluster-catalyzed vapor-liquid-solid (VLS) approaches since they can yield NWs with high crystallinity, monodispersity, and controlled morphology. The products can be in the form of single crystals [44, 45], twinned crystals [46-49], and core-shell NWs [50]. For example, in the case of Si NWs [21] (Figure 1.1), a volatile gaseous precursor such as silane  $\text{SiH}_4$  [51] or disilane  $\text{Si}_2\text{H}_6$  [52], serves as the Si source for growth. The Au (or Ag, Pt, Al, etc. [52-54]) nanoclusters are heated above the eutectic temperature for the Au-Si system, resulting in a Au/Si liquid droplet. The continued feeding of Si reactant into the liquid droplet supersaturates the eutectic, leading to nucleation of the solid Si. The solid-liquid interface forms the growth interface, which acts as a sink for the continued Si atoms incorporated into the lattice and the continuous growth of the NW with the droplet riding on the top. During VLS growth, Si NWs are formed in near-equilibrium condition, and the growth processes can thus be considered primarily thermodynamically driven. As a result, the preferred growth direction is the one that minimizes the total free energy.

On the other hand, solution-phase methods based on capping reagents have been commonly used for synthesizing metallic NWs. [55, 56] The shape of a crystal is determined by the relative specific surface energies associated with the facets of this crystal, reflecting the intrinsic symmetry of the corresponding lattice. At equilibrium, a crystal has to be bounded by facets giving a minimum total surface energy, known as the Wulff facets theorem. [57] The shape of a crystal can also be considered in terms of growth kinetics, by which the fastest growing planes should disappear to leave behind the slowest growing planes as the facets of

the product. [58] Therefore, the shape of a crystal can be controlled by introducing appropriate capping reagents to change the free energies of the various crystallographic surfaces and thus to alter their growth rates. For example, Sun *et al.* reported a solution-phase methods that generates Ag NWs, by reducing silver nitrate with ethylene glycol in the presence of poly (vinyl pyrrolidone) (PVP), shown in Figure 1.2. [55] Pt nanoparticles serve as seeds for the heterogeneous nucleation and growth of Ag NWs because of their close match in crystal structure and lattice constants.

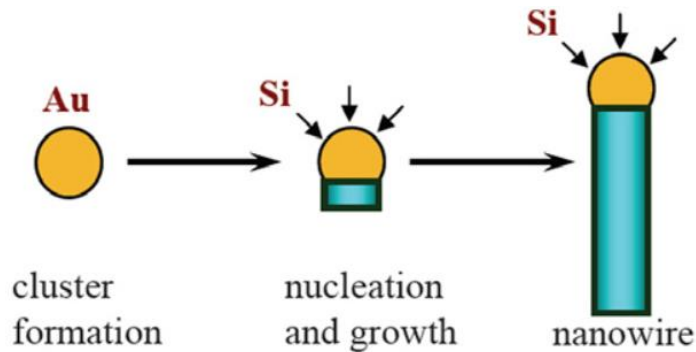


**Figure 1.1** Schematic of VLS growth of Si NWs. A Au/Si liquid droplet is first formed above the eutectic temperature (363 °C) of Au and Si. The continued feeding of Si in the vapor phase into the liquid alloy causes oversaturation of the liquid alloy, resulting in nucleation and directional NW growth. [21]

Furthermore, it has been reported that free-standing, high aspect ratio, single crystalline NWs of a variety of different materials (Cu, Au, Ag, Ag, and Si) have been successfully grown from partially C-coated, oxidized and nonoxidized Si substrates under molecular beam epitaxy (MBE) conditions. [38] Taken Cu NWs as example (Figure 1.3), both elevated substrate

temperatures (on the order of 0.65 TM of the deposited species) and the partial C layer are necessary to achieve NW growth. The effect of C morphology on Cu diffusion [59-61] will influence the location and density of NW nuclei. Since the interfacial energy between Cu and C is high [62], it is energetically unfavorable for nuclei to grow laterally onto the C film. This could help to force the nuclei to grow vertically. Once nuclei have formed, further growth occurs by diffusion of Cu adatoms on the C covered substrate to the existing nuclei and incorporation.

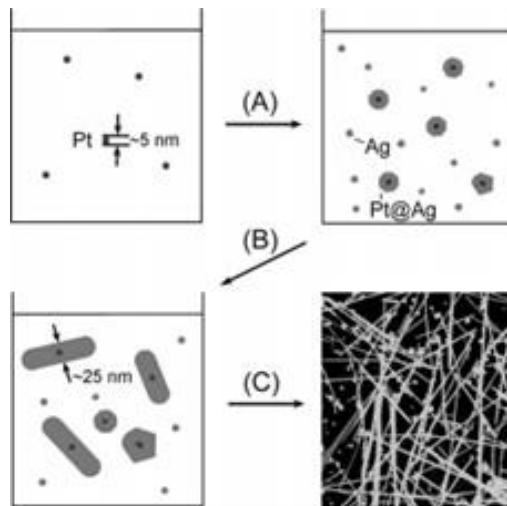


**Figure 1.2** Schematic illustration of major experimental steps involved in the preparation of Ag NWs through a polyol process with Pt nanoparticles as the seeds: (A) Formation of bimodal Ag nanoparticles through heterogeneous nucleation on Pt seeds and homogeneous nucleation; (B) evolution of rod-shaped Ag nanostructures as directed by the capping reagent, PVP; and (C) growth of the Ag nanorods into NWs at the expense of small Ag nanoparticles. [55]

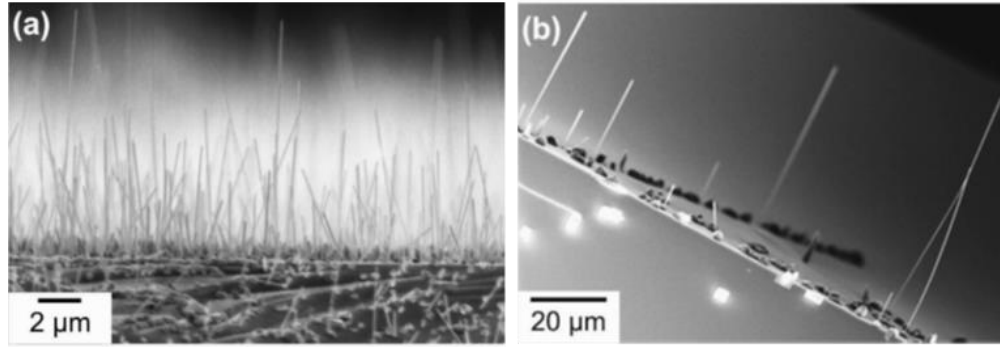


**Figure 1.3** SEM images of Cu whiskers. (a) Nominal film thicknesses of 45 nm Cu were thermally evaporation deposited at 650 °C with a nominal deposition rate of 0.05 nm/s. The NWs shown in this micrograph have a maximum length of 10 μm, and the diameters vary from 30 to 100 nm. (b) NWs formed on one of the cleavage planes. The NWs are free-standing and appear perpendicular to the surface. [38]

### 1.2.1 SiC NWs

As one of the most important compound semiconductors, SiC has shown exceptional properties such as wide (tunable) bandgap, high strength, high thermal conductivity, good thermal shock resistance, low thermal expansion and good chemical inertness. [63-66] These unique properties make SiC recognized as an ideal candidate for power electronics, hostile-environmental electronics, blue light emitting diodes, sensors, composites and heterogenous catalyst supports. [67-72] With low dimensionality, quantum confinement and shape effects, nanoscaled SiC materials are expected to exhibit properties that their bulk counterparts may not have due to increasing surface-to-volume ratio.[72-74] For instance, SiC nanoresonators

are capable of yielding substantially higher frequencies than GaAs and Si counterparts for given dimensions. [74]

Vapor-phase synthesis is the most well-established approach to the formation of SiC NWs, which usually have high crystal integrity, clear and clean faceted structures, and controllable compositions. [40] The common vapor-phase techniques include chemical vapor deposition (CVD), thermal evaporation, heating, combustion, pulsed-laser deposition, arc discharge, electrospinning, and so on. Figure 1.4 shows SiC NWs prepared by using high-temperature thermal evaporation through the VLS process. [75] The source materials are SiO<sub>2</sub> and C powder, plus a small amount of Fe powder as catalyst. The mixture of these materials evaporates at 1500 °C, near the center of an Al<sub>2</sub>O<sub>3</sub> tube. The evaporated source moves downstream with Ar flow and deposits on the substrate at about 800 °C. With numerous polytypes, SiC NWs also contain many SFs or nanotwins within 3C crystalline structure.

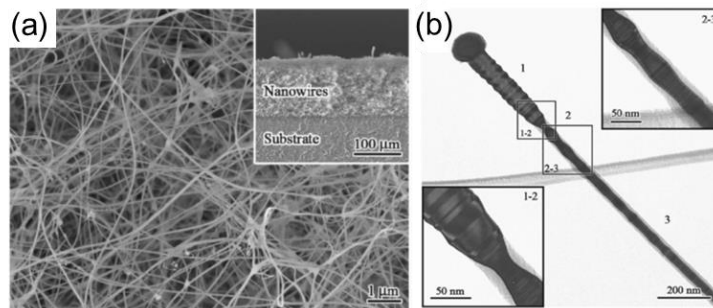


**Figure 1.4** (a) SEM image of SiC NWs, with a cross-sectional view in the inset. (b) Bright field TEM image of a SiC NW in three stages (center), with transitions shown at the two corners. [75]

### 1.2.3 ZnO NWs

ZnO is an important semiconducting and piezoelectric material with a large exciton binding energy and a wide band gap. [76, 77] ZnO NWs have been found broad applications ranging from nanoelectromechanical systems (NEMS) [78, 79] to nanosensors [80, 81] to nanogenerators [82]. ZnO NWs provide an attractive candidate system for fundamental quantization and low-dimensional transport studies [79]. The large surface area of the NWs and bio-safe characteristics of ZnO makes them attractive for gas and chemical sensing and biomedical applications, and the ability to control their nucleation sites makes them candidates for micro-lasers or memory arrays.

ZnO nanostructures can be synthesized by different methods. Most of them are bottom-up methods like wet chemical method, [83-85] chemical or physical vapor deposition, [86-88] pulsed laser deposition and molecular beam epitaxy [89-91]. There is also a top-down approach to fabricate ZnO nanostructures. [92] Among these methods, ZnO nanostructures synthesized via VLS growth mechanism can be well controlled on orientation, position, size, morphology and density, as shown in Figure 1.5. [93] With Au colloids as the catalysts, a mixture of ZnO and graphite powders in a quartz boat was used as the Zn source. [79] The quartz boat was heated to 950 °C by a local heater, and the generated Zn vapor was carried by a flow of Ar to the growth zone, where O<sub>2</sub> was injected to enable the NW growth. The temperature of the growth zone was held at 820 °C during the growth under a constant pressure of 7.5 Torr.

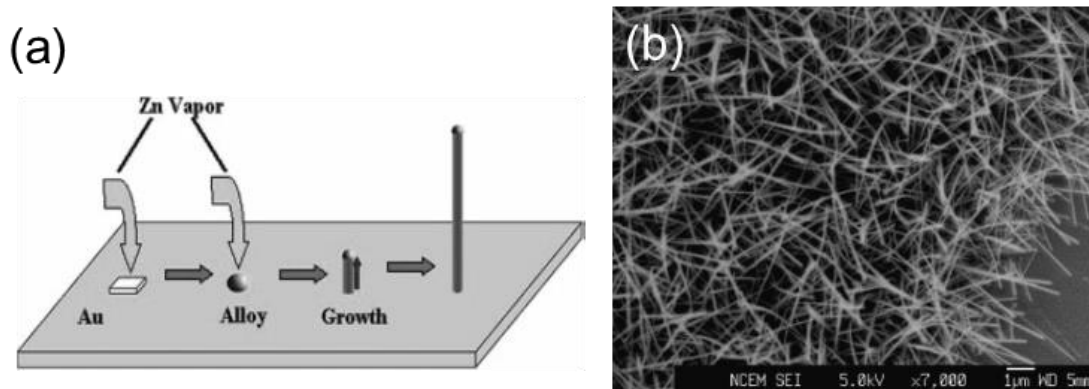


**Figure 1.5** Schematic showing the growth mechanism of ZnO NWs, (b) SEM image of ZnO NWs grown on Si (100) substrate. [93]

### 1.2.2 Ag NWs

Ag NW is an important class of metallic NWs because of its potential use as interconnects in view that bulk silver exhibits the excellent electric and thermal conductivity among metals. Ag NWs have been found broad applications in flexible/stretchable electronics as conductors or electrodes. [22, 94-97] Another interesting property of Ag NWs is the surface plasmon resonance which refers to the collective oscillation of conduction electrons in resonance with incident radiation. [98] Hence, Ag NWs have also been used in a wealth of applications including biosensing and plasmonic waveguiding. [99]

Various methods have been developed to synthesize Ag NWs with or without internal twin boundaries (single crystalline, bi-twinned and penta-twinned) running parallel to the length direction. [38, 100, 101] **Single crystalline and bi-twinned Ag NWs** are often synthesized by physical vapor deposition onto Si substrates under ultrahigh vacuum conditions at elevated temperature. Bare Si substrates were inserted into an ultra-high vacuum molecular

beam epitaxy system with pressures at  $\sim 10^{-10}$  mbar. A Ag source was heated up to 800 °C and deposited at a rate on the order of  $0.01 \text{ nm s}^{-1}$  onto the substrates, which were maintained at 750°C during the deposition process. The NWs grown on Si substrates often have lengths of at least 5 to 25  $\mu\text{m}$  and diameters between 50-150 nm. The bottom-up growth at near-equilibrium conditions results in distinct surface facets, and the NWs show no evidence of taper or visible roughness on the surfaces, as shown in Figure 1.6. [102]

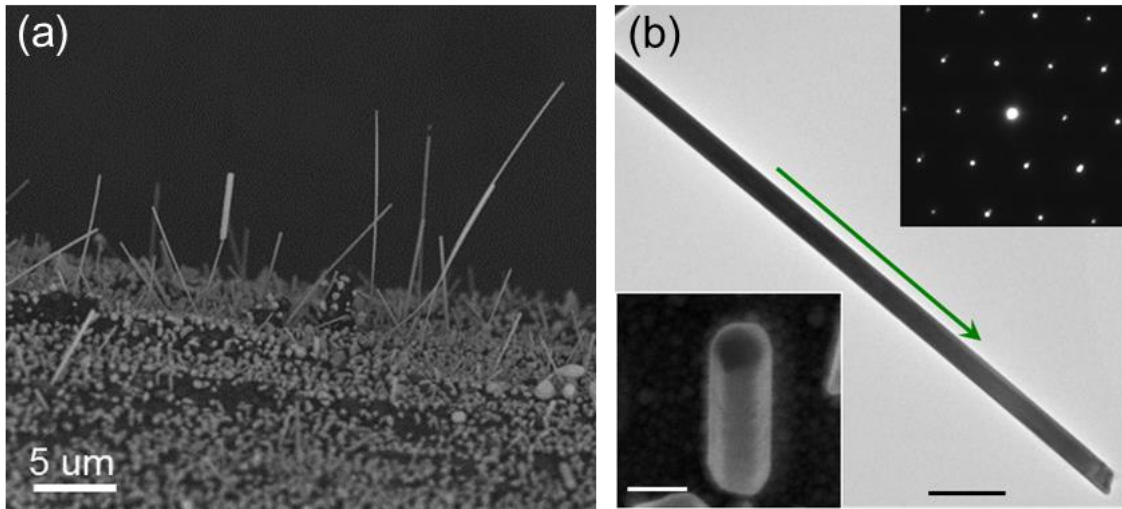


**Figure 1.6** (a) SEM image showing single crystalline or bi-twinned Ag NWs on Si substrate. (b) TEM image of single crystalline Ag NW with growth direction of  $\langle 110 \rangle$ . Scale bar, 200 nm. Right and left insets (scale bar, 100nm) in (b) show the selected area electron diffraction (SAED) pattern taken from  $\langle 110 \rangle$  zone axis and the hexagonal cross-sectional shape from SEM observation, respectively. [102]

**Penta-twinned Ag NWs** are synthesized via a polyol method that generated silver NWs by reducing Ag nitrate with ethylene glycol in the presence of PVP. [55, 90] The key to the formation of 1D nanostructures is the use of PVP as a polymeric capping reagent and the introduction of a seeding step. When Ag nitrate is reduced in the presence of seeds (Pt or Ag nanoparticles of a few nanometers across), Ag nanoparticles with a bimodal size distribution are produced via heterogeneous and homogeneous nucleation processes, respectively. In the following step, Ag nanoparticles with larger sizes will grow at the expense of smaller ones through the Ostwald ripening process. In the presence of PVP, most Ag particles can be confined and directed to grow into NWs with uniform diameters. Figure 1.7 shows penta-twinned Ag NWs synthesized via solution-phase methods. [102]

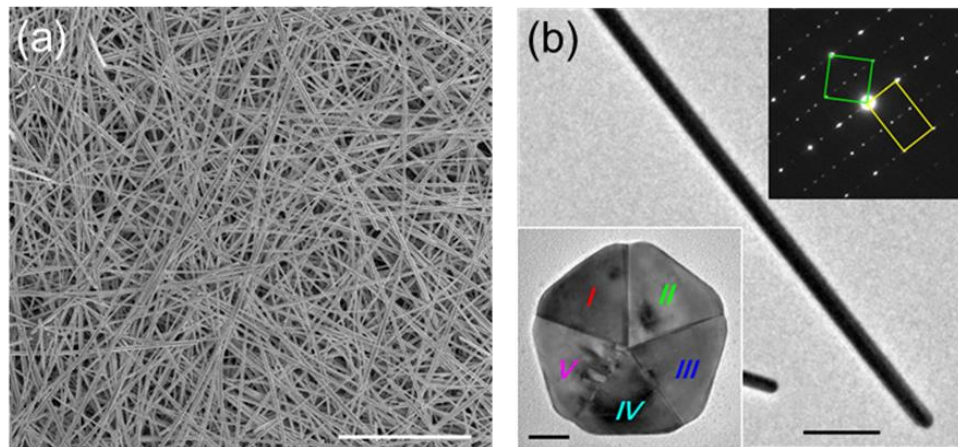


**Figure 1.7** (a) SEM image showing penta-twinned Ag NWs. (b) TEM image of penta-twinned Ag NWs showing five-fold twinned structure. Scale bar, 200nm. Right and left insets (scale bar, 20nm) in (b) display the corresponding SAED pattern and the pentagonal cross-sectional shape, respectively. [102]

## 1.3 Mechanical Characterization

### 1.3.1 Size Dependent Mechanical Behavior in NWs

The “smaller is stronger” trend has been observed in a number of crystalline metallic and semiconductor NWs, where the surface effect plays a dominant role as the sample size decreases into nanoscale. [2, 33, 38, 103-108] Figure 1.8 shows the strength of metal Cu [38, 109-112] and semiconductor SiC [113-118] whiskers as a function of the diameter. As the whisker diameter decreases from micrometers to tens of nanometers, the fracture strength increases and tends to approach the theoretical strength of the materials.

On the other hand, surface plays a dominant role in the size effect on elasticity of NWs owing to the large aspect ratio of surface and volume. [119-122] Due to a competition of factors such as bond saturation and redistribution of electron density, surfaces can be either elastically stiffer or softer than the underlying bulk material. [123, 124] In addition, surface stresses, which also arise from the coordination number reduction of surface atoms, cause deformation of not only the surfaces but also the underlying bulk material to maintain the overall equilibrium [125], which changes the elastic properties of the NWs (nonlinear elasticity). The surface stresses can cause surface reconstruction that further changes the surface elasticity and surface stress. [30, 124] Figure 1.9 show the Young’s modulus of Ag [126] and ZnO [127] NWs as a function of the diameter. Both showed a clear size effect – the Young’s modulus increases with decreasing the NW diameter when the diameter is below ~100 nm, which was attributed to the surface elasticity.

Size effect on the strength and Young's modulus of 1D nanomaterials has been well investigated in the past decades. [2, 33, 38, 103-105] However, effect of internal defects in the NWs on the mechanical behavior of 1D nanomaterials have been scarcely studied. As mentioned before [75], SiC NWs have quite complicated microstructures due to the co-existence of polytypes [64]. SiC could be face-centered cubic (FCC) (i.e., 3C or  $\beta$ -SiC), hexagonal-close-packed (i.e., 2H-SiC) or other highly-ordered structures (e.g., 4H and 6H). SFs and nanotwins are also common in SiC due to the low SF energy. Therefore, it is of important relevance to identify which polytype or microstructure is more prone to fracture. In Chapter 2, we reveal the effect of size-dependent defect density on the mechanical properties of SiC NWs via *in situ* tensile testing and microstructure characterization of SiC NWs before and after deformation.

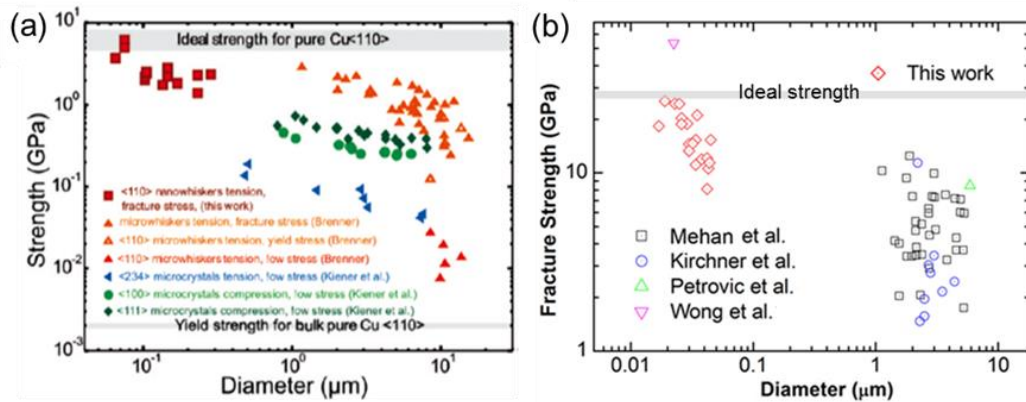


**Figure 1.8** (a) Strength plotted as a function of whisker diameter and compared to reported values of strength of pure Cu single crystalline small scale specimens. [38, 109-112] (b) Fracture strength of SiC NWs and whiskers as a function of the diameter. [113-118]

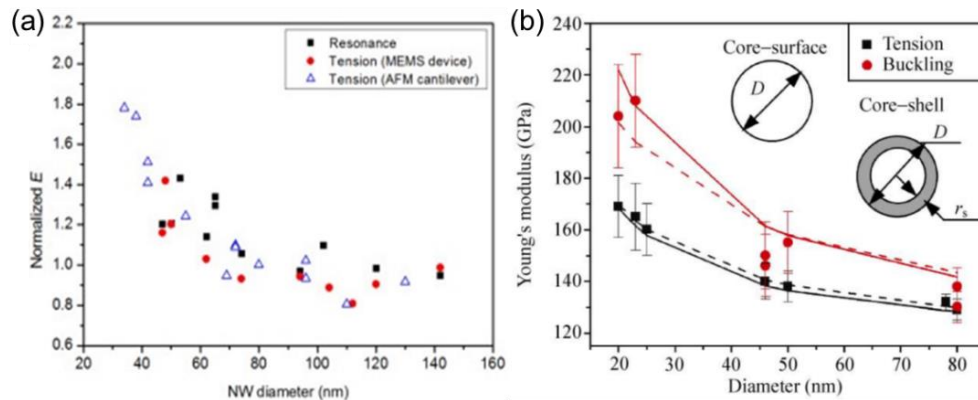


**Figure 1.9** (a) Modified Young's modulus as a function of NW diameter. The measured Young's modulus was normalized by the bulk modulus of 84 GPa. [126] (b) Young's modulus versus diameter of ZnO NWs from both tension and buckling tests. The fitting curves from the core-surface model (solid) and the core-shell model (dash) are also plotted. Inset shows the schematic of both models. [127]

### 1.3.2 Anelasticity in Crystalline NWs

When materials are subjected to an external stress, they will experience elastic deformation followed by irreversible plastic deformation (for ductile materials) when the external stress is higher than the yield stress of the materials and finally fracture. The elastic deformation is reversible, that is, the materials will resume their original shapes once the applied stress is retracted. In most materials, the recovery is immediate, but in some materials there is a delay in shape recovery after the applied stress has been removed. This time-dependent behavior is called anelasticity. [128] Anelastic materials exhibit gradual full recovery of deformation once a load is removed, leading to efficient dissipation of internal

mechanical energy [129]. As a consequence, anelastic materials are being investigated for energy damping applications. [130, 131]

Anelasticity has been observed in alloys [132-134], ceramics [134] and bulk metallic glasses [135] owing to migration of point defects, phase transformation, motion of grain boundary, etc. In general, anelasticity is due to time-dependent structural evolution at the microscopic and atomic scales that are attendant to the deformation. For example, point defects which cause a change of lattice parameter and have a relatively high mobility give rise to a relaxation process which has been called the Gorsky relaxation [129]. A schematic illustration of the Gorsky effect is shown in Figure 1.10a. [136] In a gradient of dilatation caused for instance by bending a beam-shaped sample, the interstitials will migrate from the compression to the dilatation region (for vacancies the opposite direction) thus building up a gradient in defect concentration which manifests itself macroscopically as a time-dependent reversible strain. Figure 1.10b shows the time dependence of the anelastic strain of Ta with 4.3 at.% H at different temperatures. At macroscopic scale, however, anelasticity is usually very small or negligible, especially in single crystalline materials [137, 138].

Anelasticity was frequently observed in nanocrystalline (NC) metallic materials associated with their large content of GBs. For instance, in NC Au, the large anelastic strain was considered to be caused by cooperative motion of atoms in the GBs. [133] Anelasticity was also observed in NWs recently. [139, 140] For example, Figure 1.11 presents a series of TEM images showing the anelastic behavior of a GaAs NW with a diameter of  $\sim 25$  nm. [139] The anelasticity of GaAs NWs was considered to be attributed to the amorphous surface layer. However, the detailed mechanism remain elusive.

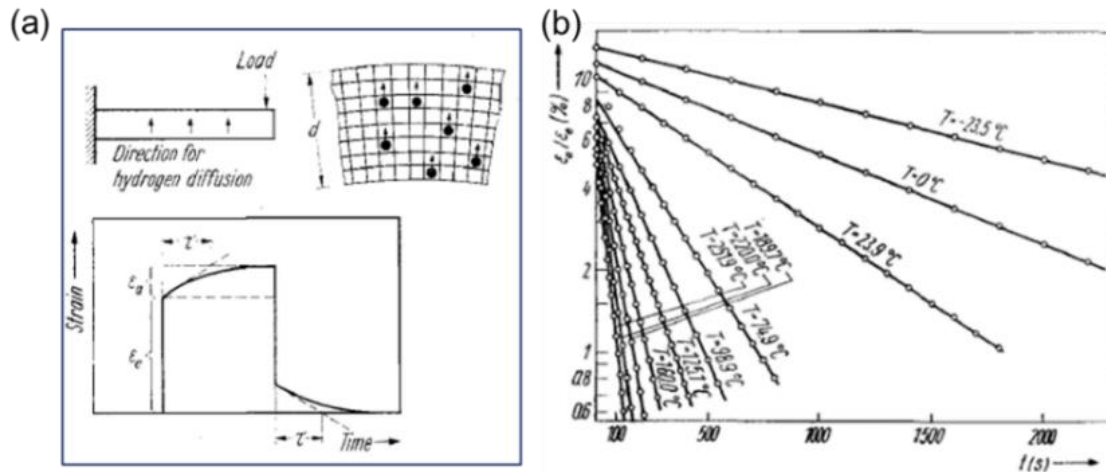


**Figure 1.10** (a) A schematic illustration of the Gorsky effect. (b) Time dependence of the anelastic strain at different temperatures ( $\text{Ta} + 4.3 \text{ at}\% \text{H}$ ). [136]

So far a vast majority of research on the mechanical properties of NWs has been focused on size-dependent elastic modulus and strength [2, 29, 32, 38, 141], with very few studies on time dependent responses [139, 140]. In Chapter 3, we report an unexpected phenomenon of large anelastic relaxation and energy dissipation in single crystalline NWs under bending. The large anelastic behavior in single crystalline ZnO NWs is governed by stress-gradient-induced migration of point defects. The observed anelasticity was attributed to a type of nonlinear Gorsky relaxation that involves the diffusion of two types of point defects under an inhomogeneous stress field.

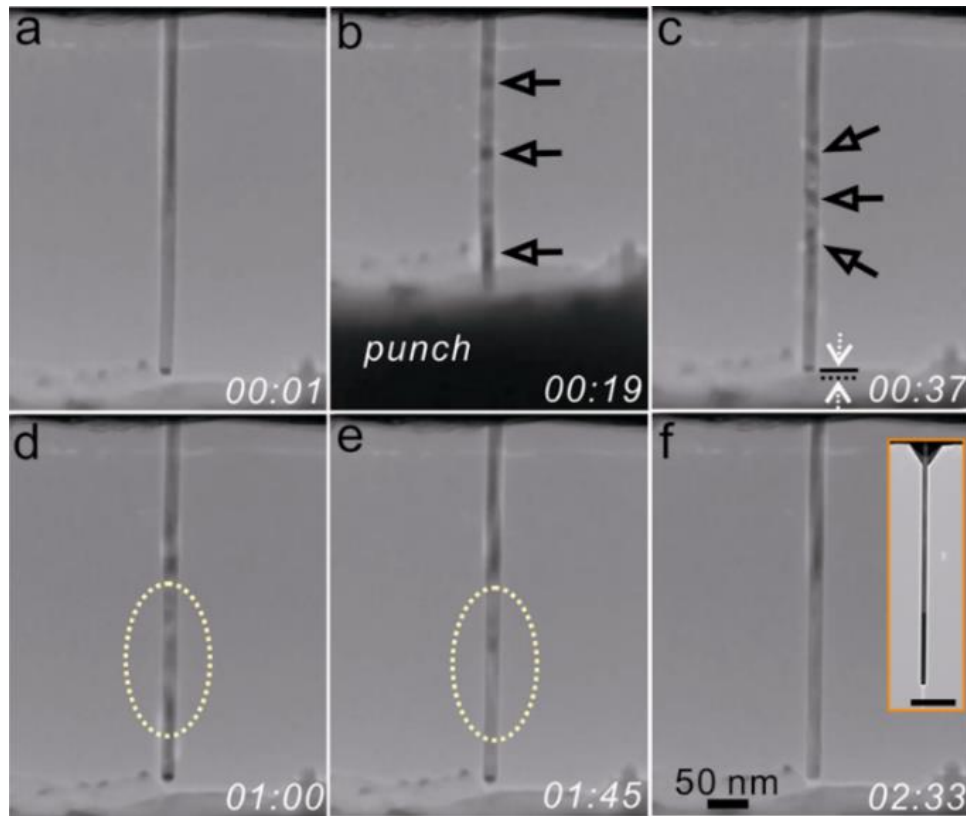


**Figure 1.11** A series of TEM images showing the anelastic behavior of a GaAs NW with a diameter of  $\sim 25$  nm. (a) Before deformation and (b) during deformation, bending contours are marked with arrows. (c) Immediately after the external stress was completely released. Contrast variation is marked by arrows and the gap between the current and original positions of the NW tip is indicated by two dotted arrows. (d,e) The NW gradually reverted to its original shape. Dotted ellipses mark the region for contrast comparison. (f) At the instant when the NW completely returned to its original shape. The inset in (f) shows the whole length of the NW. Scale bar, 200 nm. [139]

### 1.3.3 Deformation Mechanisms in Metallic NWs

The onset of plastic deformation in metallic materials relies on the nucleation of dislocations. Shrinking the size of metallic structures not only leads to an increase of mechanical strength but also to a change of deformation mode. [142-148] For metals, a transition from dislocation slip to deformation twinning has been reported when their characteristic size (grain size or wire diameter) decreases into nanometer scale. [146, 149, 150] Twinning deformation has been demonstrated to be dominant in single crystalline FCC metallic NWs as a result of superplasticity. [150-152] For example, Figure 1.12 shows the twinning deformation in a defect-free Au NW under tensile deformation. [152] The NW showed superplastic deformation induced by coherent twin propagation, completely reorientating the crystal from  $\langle 110 \rangle$  to  $\langle 100 \rangle$ . However, dislocation slip has also been observed in FCC metallic NWs leading to limited plastic deformation, shown in Figure 1.13. [38] Deformation twinning and dislocation slip are in direct competition since both occur through dislocation processes operating on the same set of slip systems. [143, 153] Additionally, detwinning has been considered as an alternative deformation mode when twins are present in the tested nanostructures under compressive [154] or tensile [155] load. What factor determines the deformation mode in metallic NWs is still the subject of ongoing discussions. [143, 144, 153]

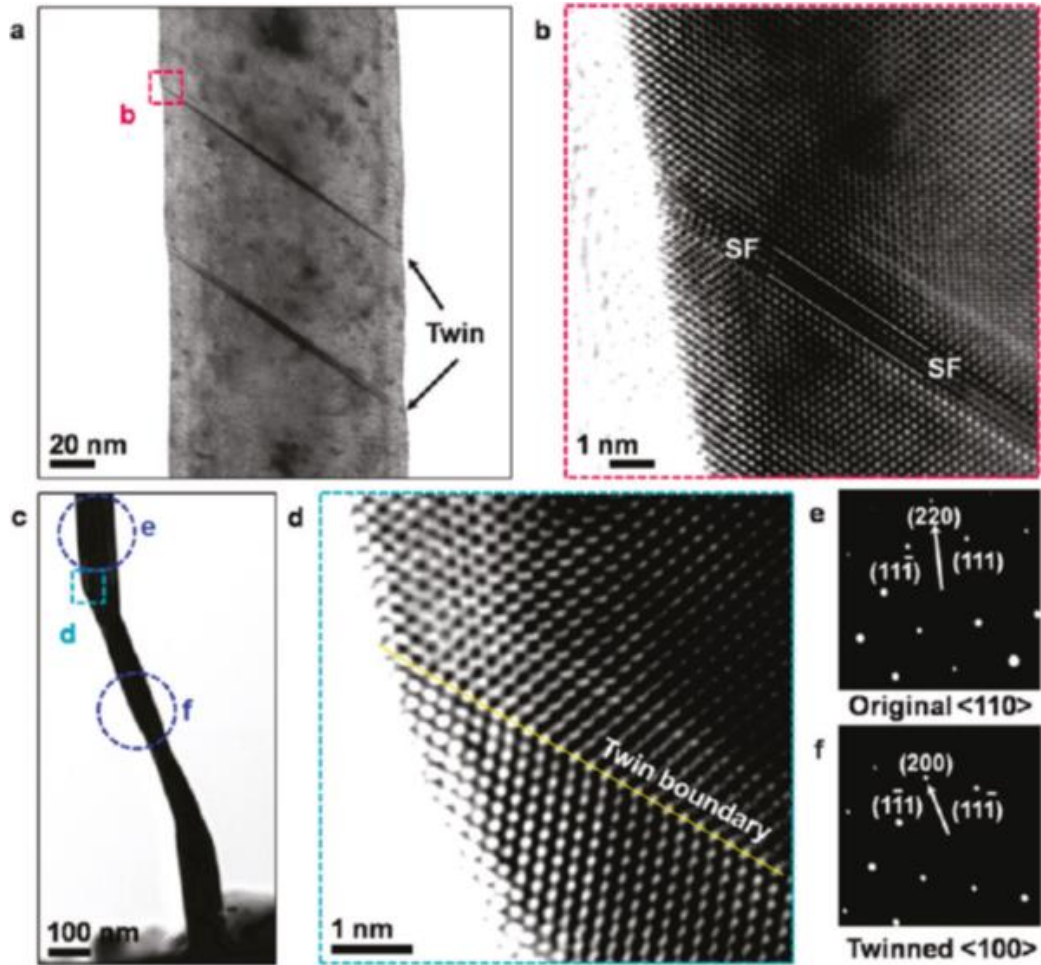


**Figure 1.12** TEM images of a Au NW under the tensile deformation. (a) Two nanotwins initially nucleated during the plastic deformation. (b) High-resolution TEM (HRTEM) image magnified from the magenta square in (a). The twin is composed of two SFs. (c) TEM micrograph showing a twin extended to 1  $\mu\text{m}$  length by twin propagation. (d) HRTEM image magnified from the cyan square in (c), showing a clear TB along the yellow line. (e,f) SAED patterns acquired from two blue dotted circles in (c), the NW lattice is changed from an original  $\langle 110 \rangle$  (e) to a twinned  $\langle 100 \rangle$  (f). [152]

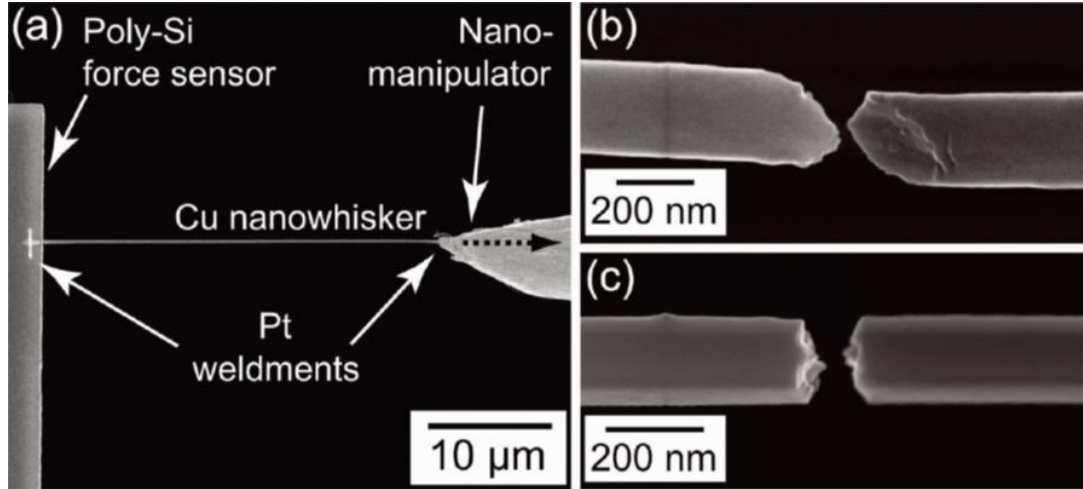


**Figure 1.13** Tensile testing of individual Cu whiskers (a) SEM micrograph of whisker mechanical testing configuration. Whiskers are gripped by e-beam deposited Pt weldments, the force applied on the specimen is measured by either a poly-Si flexure beam apparatus or a capacitive based transducer, and the local strain is measured by digital image correlation of SEM micrographs obtained during testing. (b,c) SEM micrographs of fracture surfaces of deformed whiskers showing shear (b) and brittle (c) failure. [38]

NWs with internal TBs have recently received much attention, owing to the capability of the TBs to contribute to hardening by acting as effective barriers to dislocation motion. NWs with perpendicular, inclined or parallel TBs with respect to the NW length direction have been studied recently. [103, 106, 155-159] The effective hardening due to the perpendicular TBs requires uniformly small twin spacing across the entire length of NWs, [159] thus imposing a challenge to the NW synthesis. The inclined TBs in NWs are prone to migrate, causing the coarsening of NWs through detwinning due to the finite resolved shear stress on the inclined

TBs when the NW is axially loaded. [155] For the parallel TBs, penta-twinned NWs – each NW has five twin segments joined along a common quintuple line in the axial direction – have shown pronounced strain hardening. [106] However, the penta-twinned structure introduces a complicated internal stress field and additional preexisting defects such as SFs. [102, 106] In addition, overlap of the five twin variants makes the *in situ* TEM not efficient in capturing the dislocation dynamics. A simple TB structure in NWs would be ideal to investigate the deformation mechanisms especially TB-dislocation interactions at the confined volume. In Chapter 4, we reveal transition of deformation modes in crystalline Ag NWs by combining *in situ* TEM tensile testing and atomistic modeling.

#### **1.3.4 Reversible Plasticity in Twinned Metallic NWs**

Recent studies have revealed substantial time-dependent and partially reversible deformation behaviors in small-scale materials with characteristic length scale below 100 nanometers [160], especially nanocrystalline metal thin films [161-164]. These behaviors have been attributed to the coupling and competition of reversible dislocation activities and grain boundary (GB)-mediated processes at different temperature and strain rates [139, 165-170]. More recently, atomistic simulations predicted a reversible transition between two crystal orientations during loading, leading to shape memory and pseudoelastic behaviors for several FCC single crystalline metallic NWs [171-174]. This phenomenon was attributed to the formation of defect-free twins facilitated by relatively low SF energy, nanometer size scale and surface stress.

However, there has been relatively little study on time-dependent responses of NWs under sustained and cyclic loadings, in spite of the obvious importance of this subject to the function and reliability of NW-based devices. As well accepted for metallic NWs, dislocation nucleation from free surfaces has been identified as a dominant deformation mechanism, in contrast to the forest dislocation dynamics in bulk materials [143, 146, 153, 174-181]. Recently, researchers have revealed recoverable plasticity in penta-twinned Ag NWs governed by dislocation nucleation and retraction, as shown in Figure 1.14. [102, 182] Figure 1.14a shows representative stress-strain curves of the cyclic behavior of the penta-twinned Ag NW. [182] A strong Bauschinger effect, that is, asymmetric plastic flow, and partial recovery of the plastic deformation upon unloading were observed in the NW. Further insights into the reversible plastic behavior are obtained by *in situ* TEM investigations, which demonstrated the reversible nature of the plastic deformation in these penta-twinned NWs governed by dislocation nucleation and retraction during the loading-unloading processes, as shown in Figure 1.15. [182]

A complete recoverable plasticity has been observed in penta-twinned Ag NWs, with stress relaxation on loading and complete strain recovery on unloading, shown in Figure 1.14b. [102] Interaction between dislocations and multiple TBs were considered to contribute to the full plastic strain recovery in the penta-twinned NWs. Recoverable plasticity has also been predicted in bi-twinned Ag NWs [102] with a single TB running parallel to the NW length direction but there is lack of experimental evidence and the interaction between dislocation and single TB remains elusive. In Chapter 5, we report recoverable plasticity in bi-twinned Ag NWs via *in situ* TEM tensile testing.

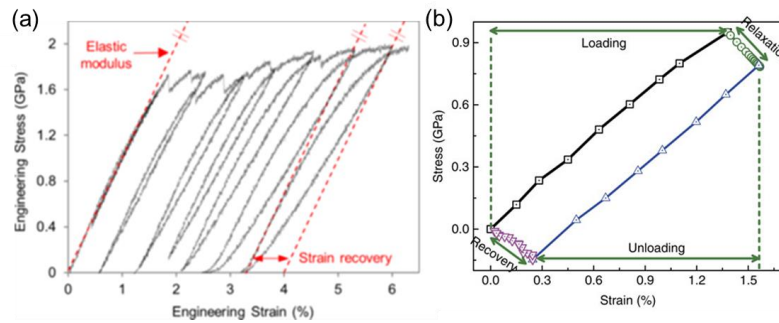


**Figure 1.14** (a) Representative stress-strain curves under repeated unload–reload cycles of a penta-twinned Ag NW with diameter of 85 nm. The strain recovery is defined as the difference between the strain at zero stress if ideal elastic unloading happens (dashed lines) and the actual strain at zero stress. [182] (b) A stress-strain curve for a penta-twinned Ag NW (120 nm in diameter). Note that in both cases the relaxation and recovery steps took 15 min each. [102]

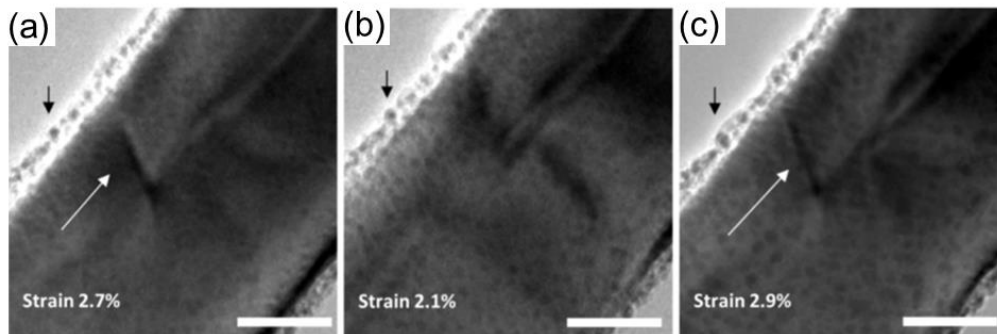


**Figure 1.15** Experimental evidence of reversible plastic deformation. (a) As the strain increased to 2.7%, the loading process was stopped and the defect was imaged. Note the black arrow as a point of reference for subsequent images. (b) Keeping the same magnification, unloading is performed, leading to the disappearance of the defect. Further loading (c) leads to the nucleation of the defect at the same location. Scale bars, 20 nm. [182]

#### 1.4 *In Situ* Nanomechanical Testing Techniques

The emergence of 1D nanomaterials as fundamental constituents of advanced materials and as key building blocks of next-generation electronic and electromechanical devices calls for the investigation of the mechanical properties and the deformation behaviors of materials at nanoscale. The major challenge of conducting quantitative mechanical testing on 1D nanomaterials comes from the sample size under study. The characteristic sample size ranges from several nanometers to several hundred nanometers. This leads to extreme challenges in manipulating and positioning the sample, which is one of the key steps in testing an individual sample at nanoscale. The very small sample size also leads to challenges in precise stress and strain measurement. Electron microscopes have been platforms to perform *in situ* nanomechanical testing due to their high-resolution capability. Coupling this capability with *in situ* mechanical deformation enables researchers to have a better understanding of the mechanical behaviors of nanostructures.

A number of approaches have been developed to realize *in situ* mechanical deformation in electron microscopes. In 1968, *in situ* indentation experiments were carried out in SEM by using a very fine stylus as an indenter to measure the mechanical properties of metal surfaces, where loads as low as 2  $\mu\text{N}$  could be applied. [183] With some modification of *in situ* indentation techniques in SEM, a series of *in situ* deformation experiments – including indentation, compression, and bending – were conducted in either an SEM or a TEM in 1970. [184] This was the first use of contact probes inside a TEM. Later, the use of actuated piezo-

driven diamond indenters led to the rapid development of *in situ* deformation techniques. [47, 114, 159, 185-198]

In this section, we review recent advances in experimental techniques for *in situ* nanomechanical testing on 1D nanomaterials, focusing on *in situ* SEM/TEM testing techniques. Because, *in situ* SEM/TEM techniques can allow real time observation of the sample and reach nanometer resolution. *In situ* SEM manipulation of 1D nanomaterials is also an important technique to prepare samples for *in situ* TEM mechanical testing. From the testing setup view point, we categorize these techniques into manipulator and sensor based techniques, and MEMS based techniques.

#### **1.4.1 Manipulator and Sensor Based Techniques**

To conduct mechanical testing of 1D nanomaterials, it is required to select a suitable individual nanostructure from the source substrate, clamp the nanostructure and transfer it to desired destination. Electron microscopy provides real time imaging capability with nanometer resolution for manipulating and a nanomanipulator is necessary to complete the manipulating process. A nanomanipulator based on multi-axes piezo actuation can operate in both coarse micrometer resolution mode and fine nanometer resolution mode, which gives the manipulator a large travel range in three axes directions and accurate positioning capability when needed. Various nanomanipulators have been developed to serve this purpose. [199, 200] A nanomanipulator from Klocke Nanotechnik has been widely used by many research groups [2, 201, 202] to explore nanomechanics area, as shown in Figure 1.16. Li *et al.* [203] have used

several nanomanipulators from Kleindiek Nanotechnik to form a multi-probe platform inside SEM to perform a more complex mechanical testing system.

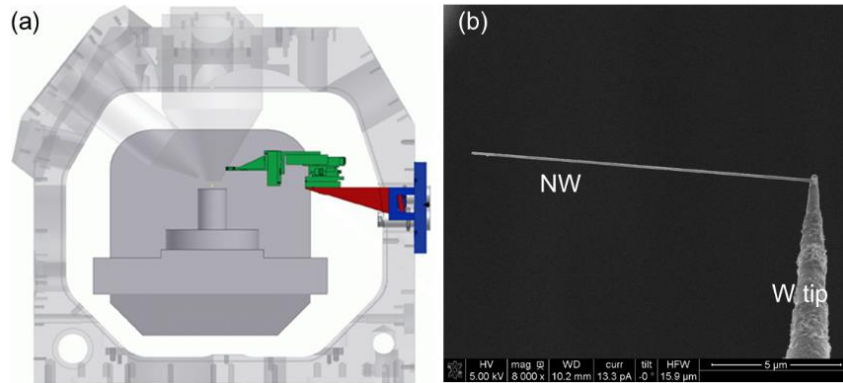


**Figure 1.16** (a) Schematic of a nanomanipulator in SEM chamber. (b) Picking-up a NW by the sharp W tip.

The nanomanipulator could serve as a loading mechanism during mechanical testing. Besides the nanomanipulator, a force sensor is needed to form a complete mechanical testing system. Force sensors can measure how much force is applied to the sample. With the geometry of the sample known from SEM image characterization, one can calculate the applied stress. Atomic Force microscope (AFM) cantilever is the most commonly used force sensor. With the nanomanipulator and force sensor available in SEM chamber, the testing setup is ready to perform mechanical testing on nanomaterials. [204-207] Figure 1.17 shows *in situ* mechanical testing by using a stiffer AFM cantilever with very sharp tip and a metal probe from the manipulator. [2] The mechanical properties of Si NWs [2], ZnO NWs [127, 200], Cu whiskers [38], Au NWs [152], and Ag NWs [103], have been measured using this testing setup. In some

cases, the AFM cantilever can serve as both manipulator probe and sensor. [208, 209] For example, Zhu *et al.* [209] used an AFM cantilever to bend ZnO NWs with a large range of diameter (85-542 nm). They were able to quantitatively measure the fracture strain, strength, and flexibility of ZnO NWs.

The nanomanipulator and force sensor based technique provides plenty of room for manipulation of 1D nanomaterials. This can save time in picking up and mounting the samples. A drawback of this technique is that for most testing setups both stress and strain measurements are deduced from microscopic images, which limit the possibility of simultaneously measuring stress and strain. The size of this testing setup also limits the possibility of putting it into TEM for *in situ* TEM testing to get more accurate measurements or investigate the deformation mechanisms. One solution is to develop a MEMS based device suitable for mechanical testing.

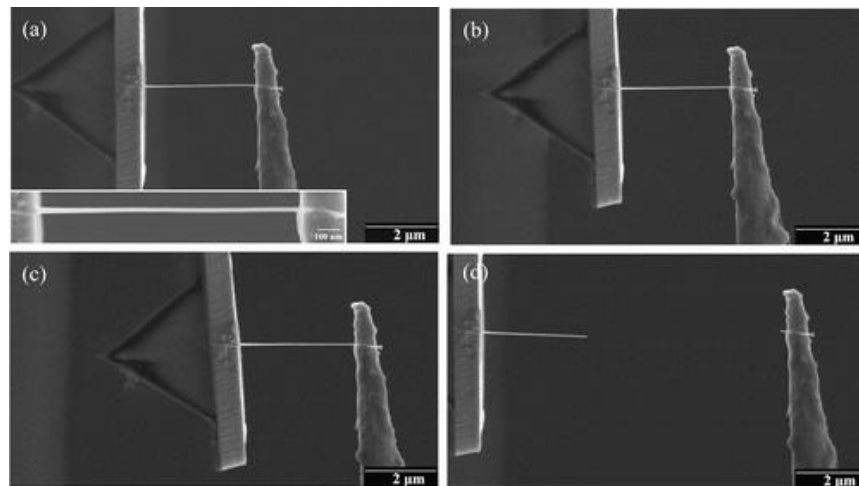


**Figure 1.17** (a–c) A series of SEM images taken during the tensile test for a Si NW with diameter of 23 nm. Inset of (a): High resolution SEM image of the NW for strain

measurements. (d) SEM image showing that fracture occurs on the NW when the load was applied to a certain value. [2]

### **1.4.2 MEMS Based Techniques**

MEMS based device has the advantage of sensing the load without taking images and possesses a size of several tens or hundreds micrometers. Besides, MEMS based device can achieve load and displacement measurements with resolution of nano-Newton and nanometer or better. And it allows us to monitor the microstructure evolution in the sample during the testing under SEM/TEM. It appears to be the most advanced alternative for conducting mechanical testing on nanomaterials. The fabrication of MEMS based device uses traditional microfabrication techniques, which can create various geometries for mechanical testing purposes. A MEMS based device for mechanical testing usually includes three parts: actuator, sensor, and sample testing region. Based on the difference in actuation mechanism, these MEMS based devices can be divided into two categories: external load actuated MEMS based device and electronic actuated MEMS based device.

The external load actuated MEMS based devices do not have integrated actuation mechanism. They only provide mechanical connections to an external load. External load is usually applied by a piezo-actuator to pull or push the MEMS based device to generate a desirable mechanical motion on the sample testing part. [210-213] Figure 1.18a shows such a MEMS based device to characterize mechanical properties of thin film. [213] The rectangular shaped test chip has one pin hole on each end. The test chip can be glued to a piezo-actuator (Figure 1.18b) or mounted on two pins on a TEM straining stage (Figure 1.18c). Force

measurement of this device need to image the deflection of force sensor beam, which is indicated by relative distance between markers A, B and fixed beam (shown in inset of Figure 1.18a). Lou *et al.* [195] developed a MEMS based device to convert compressive force from a nanoindenter to pure tensile loading. In this setup, force measurement is recorded by the nanoindenter. By utilizing the push-to-pull design, this device is able to perform mechanical testing on different 1D nanomaterials.

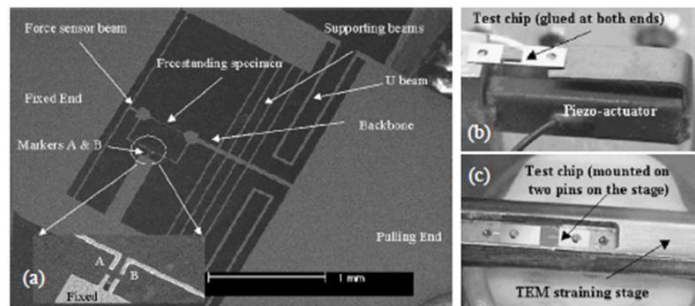


**Figure 1.18** (a) A tensile MEMS based device with co-fabricated thin film sample. Image showing the device glued to (b) a piezo-actuator and (c) mounted on two pins of a TEM straining stage. [213]

For electronic actuated MEMS based devices, thermal actuation and electrostatic force actuation are the most common used actuation mechanisms. These devices provide electrical connection to outside electric signal (e.g. current or voltage). In a thermal actuator, mechanical motion is generated by joule heating. [202, 214-217] Under actuation voltage or current, the temperature increases on the device, this leads to thermal expansion of the components. By carefully designing the structure of the actuator, one can get controllable displacement output.

Zhu *et al.* [202] developed a thermally actuated MEMS based device, which consists of a V-shaped thermal actuator and a capacitor load sensor, as shown in Figure 1.19. To minimize temperature increase near specimen testing area, the design of heat sink beams is necessary in the thermal actuator. [218, 219] By measuring the capacitance change of a series of capacitors, they demonstrated a load resolution of 12 nN for their system.

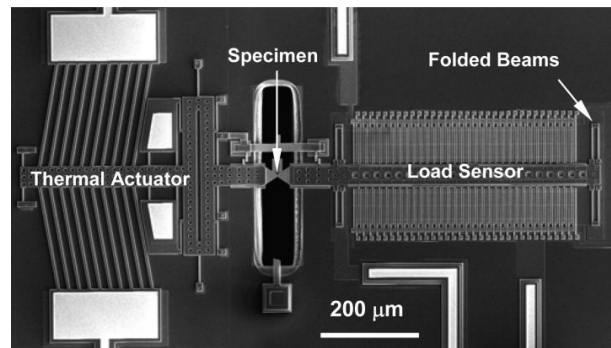


**Figure 1.19** SEM image of a MEMS based device for mechanical testing. The device includes a V-shaped thermal actuator, a load sensor, and specimen testing region. [202]

In an electrostatic force actuator, the mechanical motion is generated by the electrostatic force between a movable part and fixed part when there is an electrical potential difference between these two parts. An example of this kind of actuator is the comb drive actuator [220, 221], as shown in Figure 1.20b. Comb drive actuator is able to generate mechanical motion without involving temperature, which is an advantage over the thermal actuator (Figure 1.20a) [217]. However, due to relatively small force generated by each pair of comb, a large number of combs are needed. This leads to a relative larger in the size for comb drive actuator than thermal actuator. On the other hand, capacitive load sensing can measure

force without taking image and has high resolution in force measurement. Therefore, it has been widely used in both thermal actuated and electrostatic force actuated MEMS based mechanical testing devices as sensing mechanism.

New development in MEMS based device for mechanical testing of 1D nanomaterials is being directed to involve not just stress field but also multi-physical effects in one experiment. [222] 1D nanostructures have been demonstrated as the building blocks of next-generation electronics and sensors. For device applications it is inevitable for nanostructures to experience different temperatures. Thus, it is of relevance to characterize their thermomechanical behavior. Chen *et al.* [3] integrated their MEMS based platform inside a vacuum cryostat including a heater, a cooling channel with liquid nitrogen circulation and a PID temperature controller. Their setup is capable of achieving a temperature range from 77 to 475 K, with the largest  $0.035 \text{ K min}^{-1}$  drift. Based on the setup, a temperature dependent stress-strain behavior was found in defect-free  $\langle 110 \rangle$  Pd NWs. Kang *et al.* [223] conducted a bending experiment on top-down fabricated Si NW using a MEMS based device with controllable temperature. They reported clear plastic deformation when temperature increased to  $293 \text{ }^\circ\text{C}$  for a 720 nm Si NW. Chang *et al.* [220] recently developed a MEMS based thermomechanical platform with an on-chip heater for the *in situ* mechanical testing of 1D nanostructures from room temperature to 600 K. The MEMS based platform consists of a comb drive actuator, a capacitive load sensor, a specimen gap, and a heater based on Joule heating in close proximity to the specimen gap, as shown in Figure 1.20b. The entire platform is symmetric to ensure the same temperature on both sides of the specimen to avoid temperature gradient and heat flow through the specimen; note that the capacitive sensor is also in the form

of a comb drive, identical in geometry to the comb drive actuator. Based on the setup, the mechanical properties of single crystalline Si NWs were tested inside a SEM at different temperatures to investigate their brittle to ductile transition behavior.

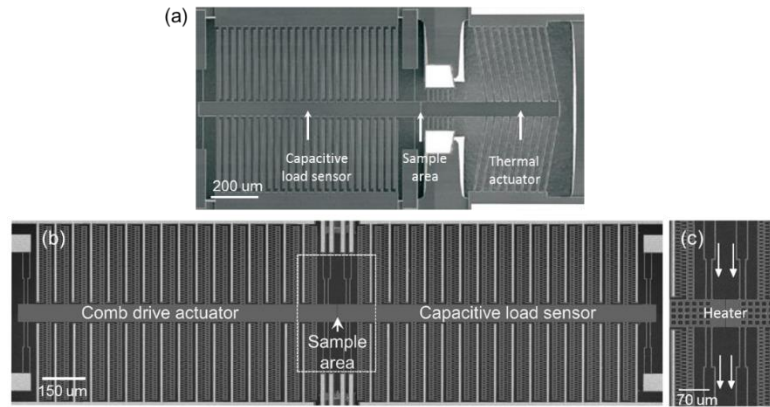


**Figure 1.20** (a) SEM image of a MEMS based device for mechanical testing. The device includes a V-shaped thermal actuator, a load sensor, and specimen testing region. [217] (b) SEM image of a MEMS based thermomechanical testing platform including an on-chip heater based on Joule heating. The device that consists of three parts: comb drive actuator, capacitive load sensor, and heater. (c) Magnified view of the heater as boxed in (b). The arrows indicate the current direction. [220]

## CHAPTER 2

### MECHANICAL PROPERTIES OF SILICON CARBIDE NANOWIRES: EFFECT OF SIZE-DEPENDENT DEFECT DENSITY

We report quantitative mechanical characterization of silicon carbide (SiC) nanowires (NWs) via *in situ* tensile tests inside scanning electron microscopy (SEM) using a microelectromechanical system. The NWs are synthesized using the vapor-liquid-solid process with growth direction of  $\langle 111 \rangle$ . They consist of three types of structures, pure face-centered cubic (3C) structure, 3C structure with an inclined stacking fault (SF), and highly defective structure, in a periodic fashion along the NW length. The SiC NWs are found to deform linear elastically until brittle fracture. Their fracture origin is identified in the 3C structures with inclined SFs, rather than the highly defective structures. The fracture strength increases as the NW diameter decreases from 45 to 17 nm, approaching the theoretical strength of 3C SiC. The size effect on fracture strength of SiC NWs is attributed to the size-dependent defect density rather than the surface effect that is common for single crystalline NWs.

#### 2.1 Introduction

Silicon carbide (SiC) has high mechanical strength, high thermal conductivity, and variable band gaps, in addition to other superior properties such as radiation resistance. [64-66] These properties make SiC a suitable material operating at high temperature, high power and high frequency as well as in harsh environments. SiC NWs have been used in a number of

mechanical and electronic applications. [7, 72] For instance, a small addition of SiC NWs into a SiC whisker-reinforced matrix was found to double the toughness of the nanocomposite. [73] SiC nanoresonators are capable of yielding substantially higher frequencies than GaAs and Si counterparts for given dimensions. [74] The operation and reliability of these nanoscale structures and devices depend on the mechanical properties of SiC NWs, which are expected to be different from their bulk counterparts due to increasing surface-to-volume ratio.

However, investigations on the mechanical properties of SiC NWs have been scarce. Han et al. performed qualitative *in situ* transmission electron microscopy (TEM) tension tests of SiC NWs and found substantial plasticity at room temperature (e.g.,  $\langle 111 \rangle$  SiC NWs experience over 200% elongation before fracture). [224] This observation is surprising in view that SiC whiskers are brittle at room temperature, and possibly due to electron-irradiation-induced phase transformation from crystalline to amorphous structure. Among the atomistic simulations, discrepancies also exist on the brittle or ductile nature of SiC NWs. Molecular dynamics (MD) simulations showed that SiC NWs deform elastically under tensile loading followed by brittle failure. [225] Wang et al. simulated the mechanical properties of SiC NWs with several different microstructures. [226] They found that almost all the microstructures lead to brittle failure with one exception. In that case, plastic deformation was predicted in 3C structure with an intergranular amorphous film parallel to the (111) plane and inclined at an angle of  $19.47^\circ$  with respect to the NW axis.

Lieber and co-workers reported the first measurement of the fracture strength of SiC NWs using atomic force microscopy based bending tests. [114] They reported that the maximum fracture strength of SiC NWs was 53.4 GPa, which is much larger than the

corresponding values for bulk SiC and microscale SiC whiskers. However, the fracture strength of SiC NWs was not studied systematically as a function of the NW size. In addition, SiC NWs have quite complicated microstructures due to the co-existence of polytypes. [46] SiC could be face-centered cubic (i.e., 3C or  $\beta$ -SiC), hexagonal-close-packed (i.e., 2H-SiC) or other highly-ordered structures (e.g., 4H and 6H). Stacking faults are also common in SiC due to the low SF energy. Therefore, it is of important relevance to identify which polytype or microstructure is more prone to fracture.

Here we report, for the first time, quantitative stress – strain measurements of SiC NWs via *in situ* tensile testing inside scanning electron microscopy (SEM). The NWs tested were synthesized using the vapor-liquid-solid (VLS) process with growth direction of  $\langle 111 \rangle$ . The SiC NWs consist of three types of structures, pure face-centered cubic (3C) structure, 3C structure with an inclined SF, and highly defective structure, in a periodic fashion along the NW length. Our tensile tests showed that the SiC NWs deformed linear elastically until brittle fracture. The fracture origin in SiC NWs was identified in the 3C segments with inclined SFs. The fracture strength increased as the NW diameter decreased, up to over 25 GPa, approaching the theoretical strength of 3C SiC.

## **2.2 Materials and Methods**

### **2.2.1 Sample Synthesis and Characterization**

The SiC NWs were synthesized by using high-temperature thermal evaporation through the VLS process. [75] The source materials are SiO<sub>2</sub> and C powder, with Fe powder

as catalyst. The mixture of these materials evaporates at 1500 °C, moves downstream with argon flow and deposits on an Al<sub>2</sub>O<sub>3</sub> substrate at about 800 °C.

The samples for TEM experiments were prepared by depositing SiC NWs from a dispersion of NWs in ethanol onto the copper grids covered with lacey carbon film (no Formvar). TEM/HRTEM observations were performed on JEOL 2010F with a Schottky field emission gun (FEG) operating at 200 keV.

### **2.2.2 *In Situ* SEM Mechanical Testing**

*In situ* mechanical testing inside a SEM was carried out using a MEMS based material testing system, which consists of a thermal actuator, a capacitive load sensor and a gap in between for mounting samples. The displacement markers are deposited using electron-beam-induced deposition of carbon. Ag NWs were mounted on the testing stage using a nanomanipulator (Klocke Nanotechnik, Germany) inside a FEI Nova 600 dual beam and clamped by carbon deposition. The loading and unloading strain rates for *in situ* SEM tensile testing were ~0.1 %/s.

## **2.3 Results**

Figure 2.1a shows a low-magnification TEM image of the SiC NWs. The NW growth direction is <111>. Most NWs are straight, while some are kinky. The straight NWs are globally uniform in diameter along the growth direction except local undulations. Figure 2.1b shows a histogram of the NW diameter based on 500 NWs. It can be seen that the SiC NWs

range from a few nanometer to ~60 nm in diameter with the average diameter of ~25 nm. Figure 2.1c shows a Raman spectrum of the SiC NWs. The spectrum exhibits two stronger and broadening peaks at 789 and 955  $\text{cm}^{-1}$ . The peak centered at 789  $\text{cm}^{-1}$  was attributed to a transverse optical (TO) modes and the one at 955  $\text{cm}^{-1}$  to the longitudinal optical (LO) modes. [227] With respect to the bulk 3C-SiC (796 and 972  $\text{cm}^{-1}$ ), the Raman frequency is shifted about 7-17  $\text{cm}^{-1}$ , which is attributed to the presence of polytypic admixtures (e.g., nanotwins or SFs are equivalent to a polytypic admixture). [72]

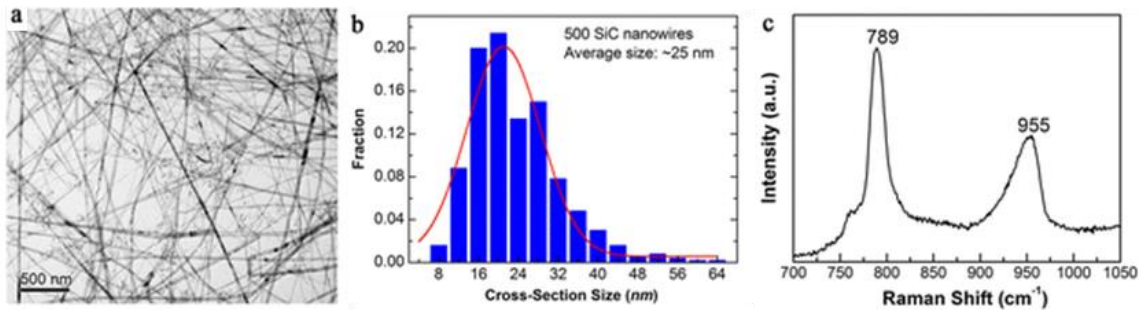


**Figure 2.1** (a) Low-magnified TEM image of a large number of randomly oriented SiC NWs. (b) Histogram of the NW diameter distribution (8–64 nm). (c) Raman spectrum of SiC NWs.

TEM imaging of individual SiC NWs indicates that the NW consists of pure 3C structures, 3C structures with inclined SFs (i.e.,  $19.47^\circ$  with respect to the NW axis) and highly defective structures in a periodic fashion. Figure 2.2a shows a low-magnification TEM image of the NW with the growth direction of  $\langle 111 \rangle$ , where the 3C structure with a  $19.47^\circ$  SF, highly defective structure and pure 3C structure are marked by I, II and III, respectively, and are separated by dashed lines. TEM images of more NWs with the three types of structures are

provided in Figure 2.3. Figure 2.2b is a high-resolution TEM (HRTEM) image corresponding to the boxed area in Figure 2.2a. The two segments indicated by A and B in Figure 2.2b are 3C structure with a  $19.47^\circ$  SF (labeled as SF- $19.47^\circ$ ) and highly defective structure, respectively. The insets in Figures 2.2b are the corresponding fast Fourier transformed (FFT) diffraction patterns taken from the areas A and B along zone axis of  $\langle 110 \rangle$ . Figure 2.2c is a magnified HRTEM image corresponding to the boxed area in segment B (Figure 2.2b), which contains several types of distinctive atomic structures including nanotwins, intrinsic SFI and extrinsic SFII. Such defective structures might contribute to the Raman shift in Figure 2.1c. An interesting question would be which segment fails first upon tensile loading on the NW. Details of the fracture surfaces will be further studied by postmortem TEM observations in the following part.

*In situ* SEM tensile tests of SiC NWs were performed using a microelectromechanical system (MEMS). [202, 217, 228] The MEMS stage consists of a thermal actuator and a differential capacitive load sensor with a gap in between (Figure 2.4a). The inset shows an individual SiC NW that is mounted across the gap. The MEMS stage was fabricated at MEMSCAP (Durham, NC) using the Silicon-on-Insulator Multi-User MEMS Processes (SOI-MUMPs). During each test, load is applied using the thermal actuator on one side of the specimen and is measured using the differential capacitive load sensor on the other side. [229] An individual NW was picked from the as-grown substrate using a nanomanipulator (Klocke Nanotechnik, Germany) inside SEM and mounted onto the MEMS stage. [202] The NW was clamped on the MEMS stage by electron beam induced deposition of carbonaceous materials in the SEM chamber. During each test, a sequence of SEM images was taken. The NW strain

was then calculated by digital image correlation of the SEM images, giving a resolution of 0.03%. [2, 103, 127] With a force resolution of 12 nN, [202] the stress resolution ranged from 52.9 to 7.5 MPa for the NW diameter ranging from 17 to 45 nm.

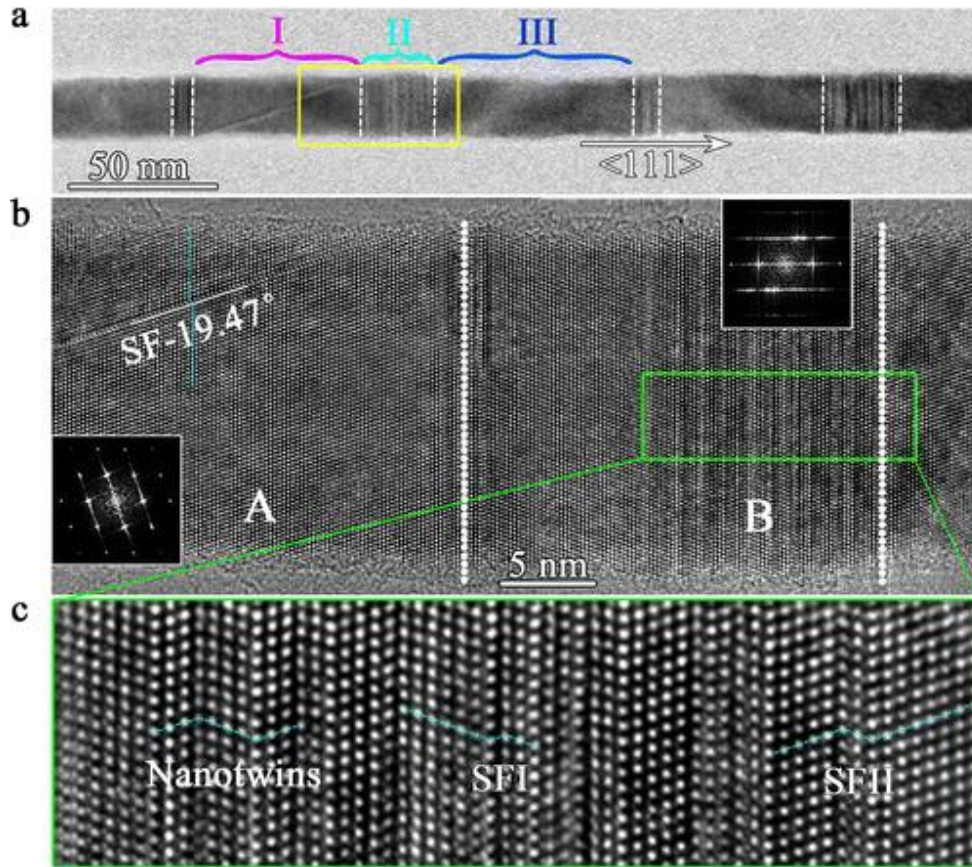


**Figure 2.2** (a) A low magnification TEM image of an individual SiC NW with the growth direction of  $\langle 111 \rangle$ , the 3C structure with an inclined SF, highly defective structure and pure 3C structure are marked by I, II and III, respectively, and are separated by dashed lines. (b) HRTEM observation of the NW containing 3C structure with a  $19.47^\circ$  SF (segment A) and high-defective structures (segment B), corresponding to the boxed area in panel (a). Insets are the FFT diffraction patterns taken from areas A and B. Note that a  $19.47^\circ$  SF is present in the

3C segment, marked as SF-19.47°. (c) A magnified HRTEM image of the highly defective structure corresponding to the boxed area in (b) showing nanotwins, intrinsic SFI and extrinsic SFII in the NW.

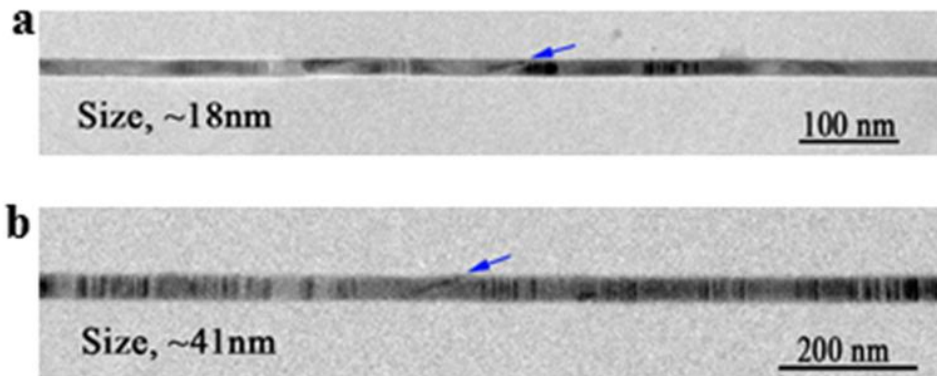


**Figure 2.3** Bright-field TEM images of SiC NWs with a diameter of 18 and 41 nm in (a) and (b), respectively. Three types of structures, pure 3C structure, 3C structure with a 19.47° SF and highly defective structure, can be seen. 19.47° stacking faults are marked by the blue arrows.

To study the size effects on the fracture strength of SiC NWs, a total of 18 NWs with diameters ranging from 17 to 45 nm were tested. All the NWs exhibited more or less linear elastic behavior until apparent brittle fracture occurred. Figure 2.4b shows three representative stress – strain curves of the SiC NWs. The inset shows the fracture surface of a SiC NW that is typical of brittle fracture. In particular, multiple loading and unloading were conducted on some of the NWs (e.g., the one with diameter of 35 nm), which confirmed that the SiC NWs are linear elastic until brittle fracture.

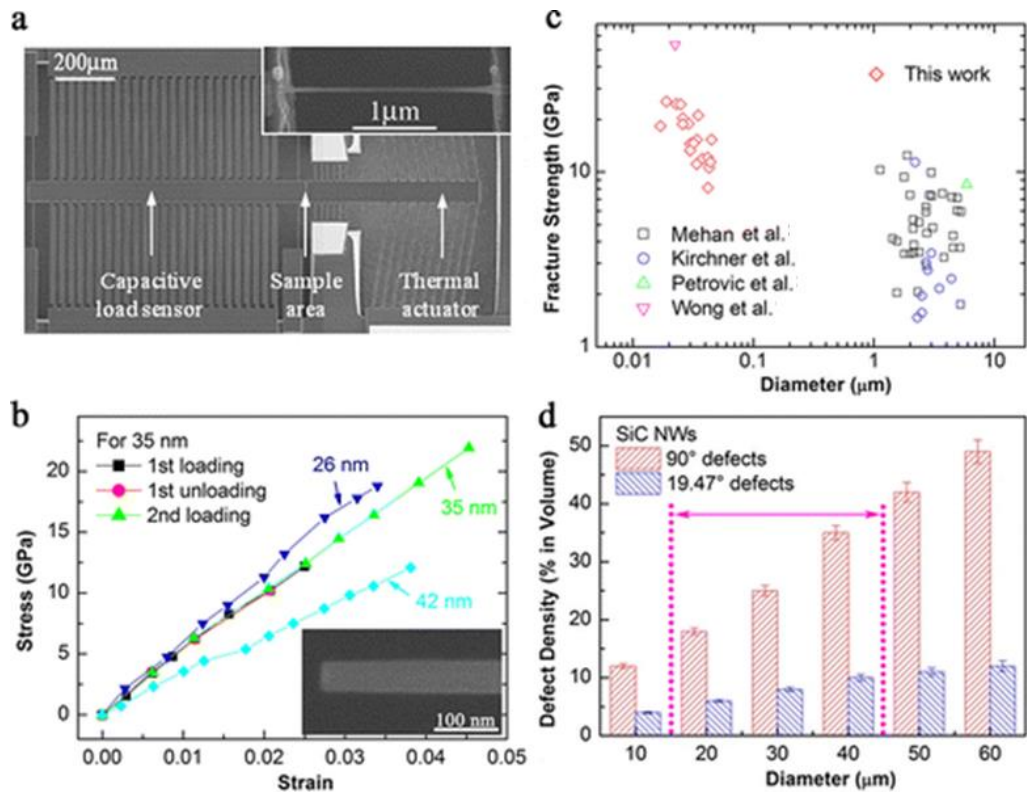


**Figure 2.4** (a) The MEMS stage used for *in situ* SEM tensile testing of SiC NWs. Inset shows a NW bridged between the actuator and the load sensor. (b) Representative stress – strain curves of SiC NWs. The curve for the NW of 35 nm in diameter includes multiple loading and unloading, showing linear elastic behavior and brittle fracture. Inset shows the fracture surface of a SiC NW. (c) Fracture strength of SiC NWs and whiskers as a function of the diameter. (d) Defect density as a function of NW diameter. Note that the defect density is defined as an average volume percentage of defect parts in a randomly selected segment with a length of 2 μm (at least 5 data in each column with a bin size of 10 nm). The range between the dot lines corresponds to the diameter range tested in this work (17-45 nm).

Figure 2.4c shows the measured fracture strength as a function of the NW diameter. The fracture strength was strongly size dependent, increasing from 8.1 to 25.3 GPa as the diameter decreased from 45 to 17 nm. The highest fracture strength in our experiments is very close to the theoretical fracture strength of 3C SiC, 28.5 GPa, in the  $\langle 111 \rangle$  direction. [226] Figure 2.4c also includes the fracture strength data of the SiC whiskers. [114-118] The collective data of whiskers and NWs show clear strengthening trend with decreasing diameter. The “smaller is stronger” trend has been observed in a number of single crystalline semiconductor and metallic NWs, where the surface effect plays the dominant role and the size effect can be interpreted by Weibull-type weakest link framework. [2, 33, 38, 103, 104] Note that while the weakest link explanation is typically employed for brittle materials, it has been applied to metallic NWs in view of the dislocation nucleation from free surfaces and nearly absence of preexisting dislocations in the NWs. [38, 103]

However, no clear size effect on the Young’s modulus was observed. The measured Young’s moduli exhibited a large scatter (from 166 to 1270 GPa) with the average value of 531 GPa. The average value is in the range for bulk SiC (503 – 600 GPa) and the range of scatter is consistent with that of SiC whiskers (from 276 to 1516 GPa).[118] The large scatter for both SiC NWs and whiskers is likely due to the co-existence of polytypes and various types of defects.

Figure 2.4d shows the defect density as a function of the NW diameter. There are two types of defects (3C structure with a  $19.47^\circ$  SF and highly defective structure). As the diameter becomes smaller, the defect density of both types of defects reduces. Out of the three types of structures in SiC NWs, the pure 3C is the strongest, the highly defective structure is the second

strongest, and the 3C structure with a  $19.47^\circ$  SF is the weakest, as predicted by MD simulations. [226] Our experimental results are consistent with the MD predictions. As shown in Figure 2.4d, when the NW diameter becomes smaller, the density of 3C structure with  $19.47^\circ$  SFs decreases, which leads to increase in fracture strength. Therefore, the size effect on fracture strength of SiC NWs is attributed to the size-dependent defect density (i.e., of the 3C structure with  $19.47^\circ$  SFs), rather than the surface effect that is common for single crystalline NWs.

Postmortem TEM images showed that the fracture surfaces are perpendicular to the loading direction  $\langle 111 \rangle$ , which is typical of brittle fracture (Figure 2.5a). It is very interesting to note that the crack always initiated and propagated in a segment of 3C structure with a  $19.47^\circ$  SF, based on our post-mortem HRTEM observations of 12 NWs (see additional examples in Figure 2.6). One reason is that the 3C segments are slightly tapered during synthesis and thus narrower than the twinned regions as synthesized (Figure 2.2a), leading to slightly higher stress in such segments. It should be emphasized that the slightly narrower fracture end in Figure 2.5b was as synthesized, not an indication of necking.

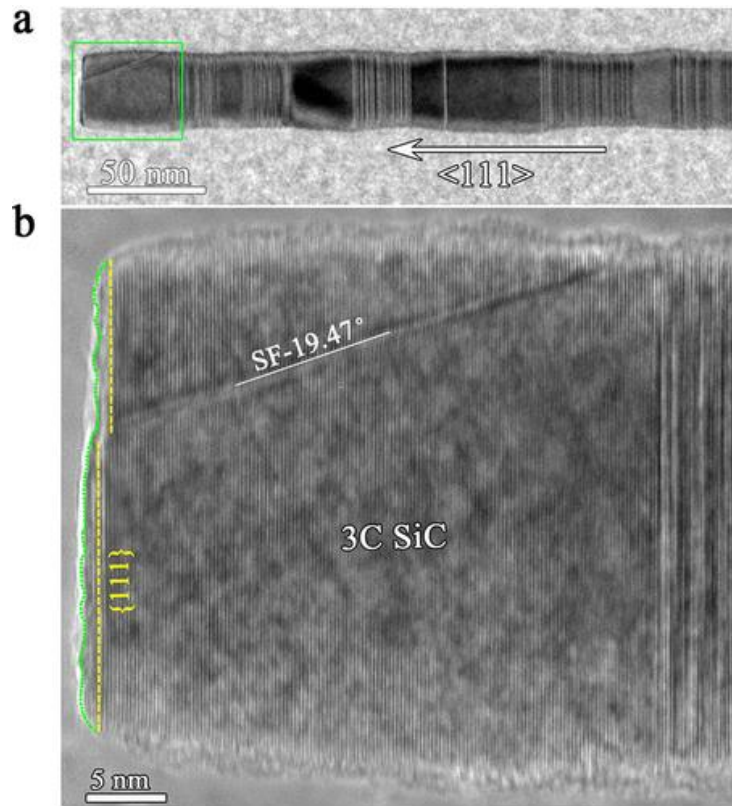


**Figure 2.5** (a) Low-magnification TEM image of the fracture surface of a SiC NW. (b) HRTEM image of the fracture surface of the SiC NW, corresponding to the marked area in (a). The loading direction is along the  $\langle 111 \rangle$  direction. The  $19.47^\circ$  SF is labeled as SF-19.47°. Similar fracture surfaces were observed other NWs tested (see the Supporting Information).

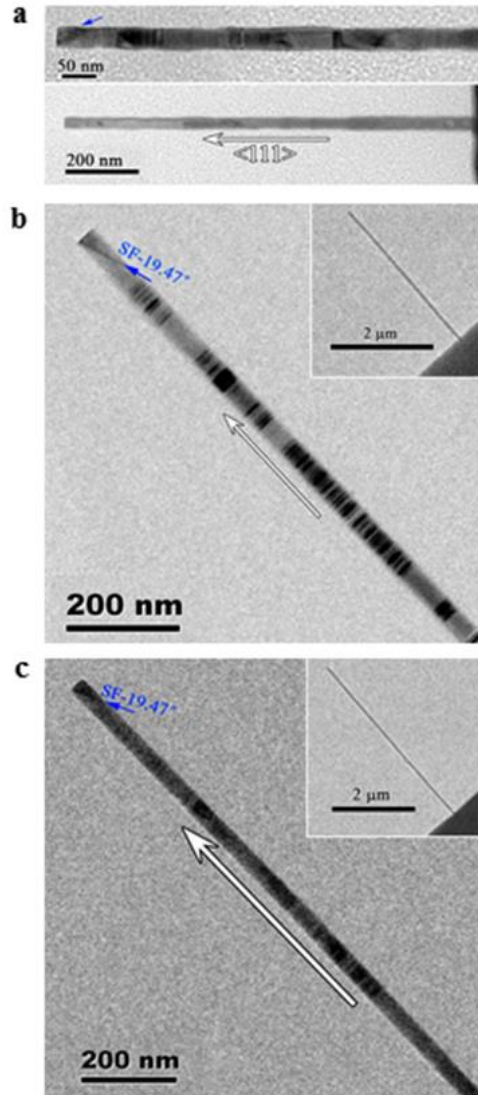


**Figure 2.6** Bright-field TEM images show the fracture surfaces of SiC NWs. The fractures were always in the 3C segments with  $19.47^\circ$  stacking faults (marked by the blue arrows). (a) corresponds to the fracture surface in the text. (b,c) are two additional examples of the fracture surfaces. Insets in (b,c) show the overview of the broken NWs attached on the cantilevers.

Another and more likely reason is that the 3C segments with  $19.47^\circ$  SFs are weaker than the segments with highly defective structures. Atomistic simulations predicted that the

cracks initiate and propagate in the regions with periodic  $90^\circ$  nanotwins (twining plane perpendicular to the growth direction) or highly-ordered structures (e.g., 4H, 6H and etc.) in SiC NWs, [226, 230, 231] which is different from our observation. The highly defective structures in our SiC NWs are not pure nanotwins or highly-ordered structures as in simulations but composed of high density of randomly distributed nanotwins, SFs and highly-ordered structures. Each individual microstructure has a thickness of only several atomic layers, which is effective in blocking crack motion and leads to strengthening of the highly defective segments. Wang *et al.* systematically investigated the effect of different types of defects (especially, SFs and nanotwins) on the mechanical properties of SiC NWs by MD simulations. [226] They found that the NW strength decreases substantially with the increasing thickness of SFs that are  $19.47^\circ$  from the NW axial direction (e.g., decreasing by 29.5% from 28.5 GPa for pure 3C structure to 20.1 GPa with SF thickness of 5 nm). On the other hand, the NW strength decreases much less for  $90^\circ$  SFs or nanotwins (e.g., decreasing by 10.5% from 28.5 GPa to 25.5 GPa with SF composition of 50%, and by 6.3% from 28.5 to 26.7 GPa with twin composition of 50%). It indicates that out of the three types of microstructures observed in our SiC NWs, the pure 3C structure is the strongest, the highly defective structure is the second strongest, and the 3C structure with  $19.47^\circ$  SF is the weakest. The MD simulation agrees well with our experimental observation that the cracks always initiate and propagate in the 3C segments with  $19.47^\circ$  SFs. The arrangement of a large number of  $90^\circ$  SFs and nanotwins in the highly defective structures are expected to play an important role in impeding crack propagation.

## 2.4 Conclusions

In conclusion, we have quantitatively studied the mechanical properties of SiC NWs. The microstructure of SiC NWs is rather complex, consisting of pure 3C structure, 3C structure with an inclined stacking fault, and highly defective structure in a periodic fashion along the NW length. We found that the SiC NWs fail in brittle fracture at room temperature, in contrast to the superplasticity as previously observed. The SiC NWs exhibited strong size effect in the fracture strength; that is, the fracture strength increased with decreasing diameter, up to over 25 GPa and approaching the theoretical strength of 3C SiC. It is interesting to observe that the cracks initiate and propagate in the 3C segments with the  $19.47^\circ$  SFs, rather than in the highly defective segments. The size effect on fracture strength of SiC NWs is attributed to the size-dependent defect density (i.e., of the 3C structure with  $19.47^\circ$  SFs), rather than the surface effect that is common for single crystalline NWs.

## CHAPTER 3

# LARGE ANELASTICITY AND ENERGY DISSIPATION IN SINGLE CRYSTALLINE NANOWIRES

\*In this chapter, Supplementary information and Movie 1 and 2 can be traced from

<http://www.nature.com/nnano/journal/v10/n8/extref/nnano.2015.135-s1.pdf>

<http://www.nature.com/nnano/journal/v10/n8/extref/nnano.2015.135-s2.wmv>

<http://www.nature.com/nnano/journal/v10/n8/extref/nnano.2015.135-s3.wmv>

Anelastic materials exhibit gradual full recovery of deformation once a load is removed, leading to efficient dissipation of internal mechanical energy [129]. As a consequence, anelastic materials are being investigated for energy damping applications. At macroscopic scale, however, anelaticity is usually very small or negligible, especially in single crystalline materials [137, 138]. Here we show that single crystalline ZnO and p-doped Si nanowires (NWs) can exhibit anelastic behaviour that is up to four orders of magnitude larger than the largest anelasticity observed in bulk materials, with a recovery time-scale in the order of minutes. *In situ* scanning electron microscope (SEM) tests of individual NWs showed that, upon removal of the bending load and instantaneous recovery of the elastic strain, a substantial portion of the total strain gradually recovers with time. We attribute the observed large anelasticity to stress-gradient-induced migration of point defects, as supported by electron energy loss spectroscopy (EELS) measurements and also by the fact that no anelastic behaviour could be observed under tension. We model this behaviour through a theoretical framework by point defect diffusion under high initial strain gradient and short diffusion distance, expanding

the classic Gorsky theory. Finally, we show that ZnO single crystalline NWs exhibit a high damping merit index, suggesting crystalline NWs with point defects are promising for damping applications.

### **3.1 Introduction**

NWs exhibit a host of novel properties that are being exploited for many applications including energy harvesting and storage [5, 8], flexible/stretchable electronics [14, 15], sensing [18], and nanoelectromechanical systems [20]. So far a vast majority of research on mechanical properties of NWs has been focused on size-dependent elastic modulus and strength [2, 29, 32, 38, 141], with very few studies on time-dependent responses [102, 139]. This work reports an unexpected phenomenon of large anelastic relaxation and energy dissipation in single crystalline NWs under bending.

### **3.2 Materials and Methods**

#### **3.2.1 Synthesis of ZnO and Si NWs**

Following the vapor-liquid-solid (VLS) method, ZnO NWs and Si NWs were synthesized on Si/SiO<sub>2</sub> substrates with Au colloids as catalysts. More details on the NW synthesis have been reported elsewhere [2, 127].

### **3.2.2 *In Situ* SEM Testing**

A MEMS electrostatic actuator was used to bend an individual NW that was clamped onto a nanomanipulator tip inside an SEM. The MEMS actuator fabricated using a silicon-on-insulator process was used for the bending tests [220]. Electrostatic actuation allowed the target displacement to be controlled precisely (on the order of 1 nm) and instantaneously (on the order of 1  $\mu$ s), which is essential for monitoring the relaxation and recovery processes in the present study. A nanomechanical testing system including a nanomanipulator (actuator) and atomic force microscopy cantilever (load sensor) was used for the tension and compression/buckling tests [127].

### **3.2.3 TEM, HRTEM and STEM/EELS Experiments**

TEM and HRTEM observations for ZnO NWs were performed on JEOL 2010F operated at 200 kV; high-angle annular dark-field (HAADF) STEM imaging and EELS quantitative analysis was carried out on an aberration-corrected FEI Titan 80-300 S/TEM with Gatan EELS spectrometer operated at 200 kV. The details of the EELS analysis are given in the Supplementary Section S6.

### **3.2.4 Theoretical Model**

We model the NW as a beam with the hexagonal cross section of diameter  $2h$ . The curvature  $\kappa$  of the NW can be related to the distributions of internal point defects as

$$\kappa = \kappa_e + \frac{16}{5\sqrt{3}h^4} \iint_D \sum_{i=1,2,\dots,n} \frac{1}{3} \Omega_i c_i y dx dy \quad (1)$$

where subscripts  $i \equiv 1, 2, \dots, n$  refer to all species of point defects;  $c_i$  and  $\Omega_i$  respectively are the concentrations and partial molar volume of  $i$ -th type of point defects;  $\kappa_e = \frac{16}{5\sqrt{3}h^4} \frac{M_e}{E}$  is the elastic curvature caused by the applied external moment  $M_e$ ,  $E$  being the Young's modulus. Considering diffusion of multiple types of internal point defects driven by gradients in their chemical potential, we derived the following governing equation

$$\frac{\partial c_i}{\partial t} = D_i \frac{\partial}{\partial x} \left( \frac{\partial c_i}{\partial x} + \frac{1}{3} \frac{E \Omega_i c_i}{RT} \sum_{j=1,2,\dots,n} \frac{1}{3} \Omega_j \frac{\partial c_j}{\partial x} \right) + D_i \frac{\partial}{\partial y} \left[ \frac{\partial c_i}{\partial y} - \frac{1}{3} \frac{E \Omega_i c_i}{RT} \left( \kappa - \sum_{j=1,2,\dots,n} \frac{1}{3} \Omega_j \frac{\partial c_j}{\partial x} \right) \right] \quad (2)$$

where  $D_i$  is the diffusion coefficient of point defects;  $R$  and  $T$  correspond to the universal gas constant and temperature. More details of the model can be found in the Supplementary Section S4.

### 3.3 Results

The bending tests were performed at the room temperature using a microelectromechanical system (MEMS) based nanomechanical testing stage inside an SEM (Figure 3.1a) [202, 220]. After the NW was held at a bent configuration for certain time (holding time), the MEMS actuator was retracted and the shape of the NW was monitored in real time (Figure 3.1b, Supplementary Movie 1). It can be seen that a large portion of the bending strain recovered instantaneously while the rest recovered gradually with time.

Figure 3.2a shows the evolution of the anelastic strain of a ZnO NW (54 nm in diameter) for an initial (total) bending strain of 1.94% with six different durations of holding time. Here the initial or total strain is the sum of anelastic strain and elastic strain, right before the load is removed. It can be seen that the recovery of the anelastic strain depends on the holding time – the shorter the holding time, the faster the recovery. Figure 3.2b shows the evolution of the anelastic strain for a holding time of 15 minutes under five different initial strains. Larger initial strain led to larger anelastic strain. The anelastic strain almost fully recovered with time (e.g., Figure 3.3a, with holding time of 15 minutes and recovery time up to 40 minutes). The anelastic strain was as large as 0.64% (in the case of 4.1% total strain).

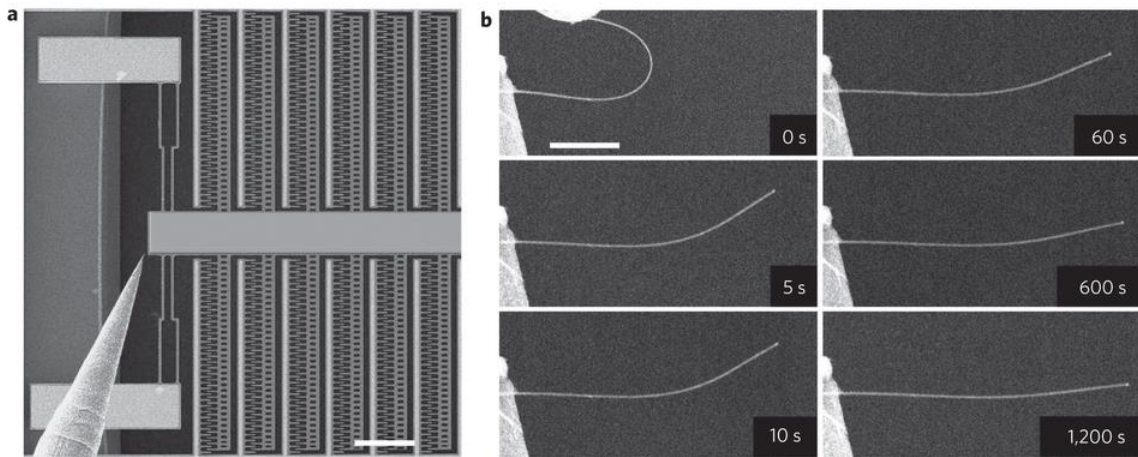


**Figure 3.1** *In situ* SEM bending test of an individual ZnO NW. (a) Experimental setup showing an individual ZnO NW that was bent between a MEMS stage (right) and a nanomanipulator tip (left). Scale bar, 100 μm. (b) A sequence of SEM images showing the recovery process of a ZnO NW after the bending load was removed. Scale bar, 2 μm.

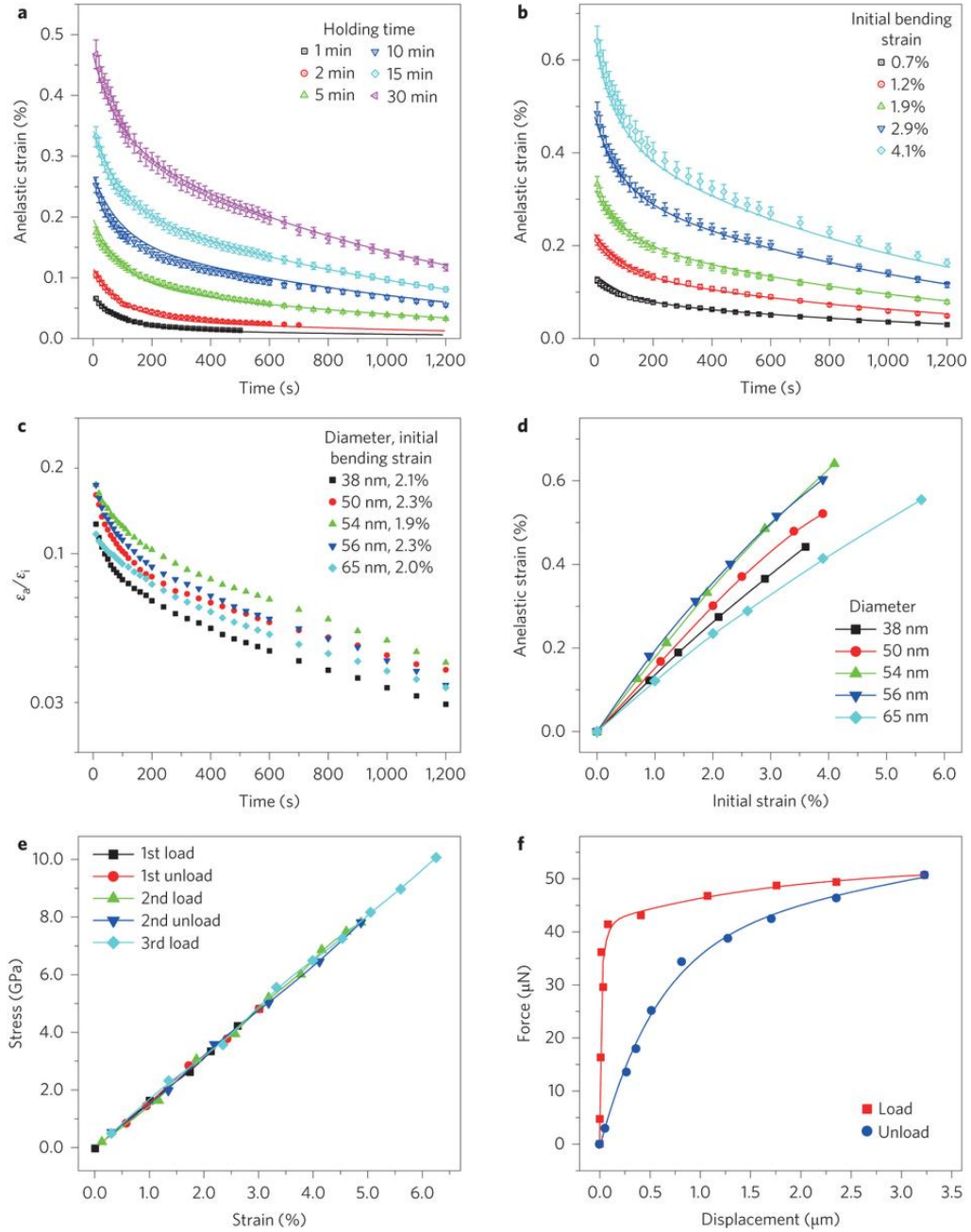


**Figure 3.2** Recovery and damping behaviors of a ZnO NW. (a) Anelastic strain as a function of recovery time for six different durations of holding time. The NW diameter was 54 nm and the initial bending strain was 1.94%. (b) Anelastic strain as a function of recovery time for five

different initial bending strains. The holding time was 15 minutes in all five cases. Solid lines in both (a) and (b) represent the fitting data from finite element analysis. Error bars for strain measurement in (a) and (b) were  $\sim 5.4\%$ . (c) Normalized anelastic strain (anelastic strain divided by elastic strain) as a function of recovery time for five ZnO NWs in diameters of 38, 50, 54, 56 and 65 nm with the same holding time of 15 minutes. (d) The maximum anelastic strain as a function of the initial strain for the five ZnO NWs. The holding time was 15 minutes in all cases. Note how, for larger initial strains, the relationship becomes nonlinear. (e) Stress-strain curve of a ZnO NW under tension. (f) Force-displacement curve of a ZnO NW under compression (buckling).

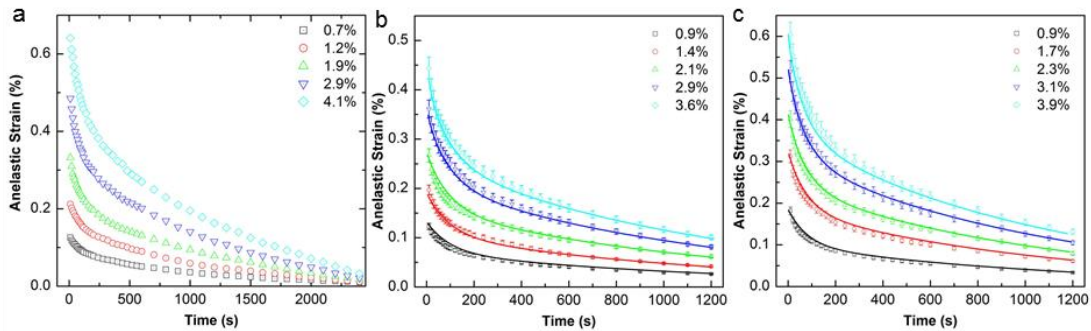


**Figure 3.3** Anelastic strain as a function of recovery time for different initial bending strains. In (a), the anelastic strain almost totally recovered ( $> 98\%$ ) within the time of 40 minutes. The NW diameter in (a), (b) and (c) was 54, 38 and 56 nm, respectively. The holding time was 15 min. Solid lines in panels (b) and (c) represent the fitting data from finite element analysis.

Five ZnO NWs were tested and all exhibited the same anelastic behaviour (Figure 3.2c and Figure 3.3b, c). Figure 3.2d shows the maximum anelastic strain (e.g., immediately after

removal of the load) as a function of the initial strain for all the ZnO NWs tested. In general the maximum anelastic strain scales nonlinearly with the initial strain; but for small initial strain, a linear approximation holds.

A number of anelastic mechanisms could be present in single crystalline materials, including thermoelastic relaxation, piezoelectric coupling and relaxations involving point defect motion [129, 137, 138]. To elucidate the underlying mechanism(s), additional experiments were carried out with ZnO NWs subjected to uniaxial tension and compression. Under tension, ZnO NWs exhibited linear elastic behaviour without observable hysteresis (Figure 3.2e) [127]. By contrast, under compression, ZnO NWs buckled and exhibited a strong hysteresis (Figure 3.2f). Both tension and compression tests were conducted using the same setup with the same mechanical/electrical boundary conditions and at loading rates comparable to the inverse timescale associated with the aforementioned relaxation under bending. Hence, the relaxation occurs only under an inhomogeneous strain field (e.g., bending or compression/buckling), rather than a homogeneous strain field (e.g., tension). Previously observed anelastic behavior in GaAs NWs was attributed to the amorphous/crystalline interface at the NW surface [139], which could not account for the observed differences between bending and tension in our present study.

Two types of relaxations, thermoelastic and Gorsky relaxations, are known to operate under an inhomogeneous strain field [129]. In thermoelastic relaxation, both relaxation strength (amplitude) and relaxation time are much smaller than those observed in the ZnO NWs (see Supplementary Section 3) [232]. Thus Gorsky relaxation, which arises from the motion of point defects in an inhomogeneous stress field [136, 233], is identified as a likely

operating mechanism. When a beam that contains volume-sensitive point defects (e.g., interstitials or vacancies) is subject to bending, the stress gradient across the sample creates a gradient in chemical potential for the point defects to migrate. For example, long-range diffusion of interstitials goes from the compressed side to the dilated side, while vacancies migrate in the opposite direction. However, the classic Gorsky relaxation predicts a linear relationship between the maximum anelastic strain and the initial strain, and has only been observed in a few bulk materials with very small relaxation amplitude [136, 233].

A theoretical model was hence developed to understand the relationship between the diffusion of point defects and the measured anelastic behaviour. The governing equation for the time-dependent evolution of defect concentrations was derived (see Methods section). Finite element simulations were performed to simulate the bending and relaxation processes under the same conditions as in the experiments. A number of defect types with corresponding diffusivities and initial concentrations were considered. The evolution of the anelastic strain was calculated as functions of the initial strain and holding time, and compared to the experimental results (Figure 3.2). For the NW with diameter of 54 nm, the best fitting identified two types of point defects with diffusivities of  $1.9 \times 10^{-14}$  and  $1.5 \times 10^{-15} \text{ cm}^2/\text{s}$ , at initial defect concentrations of  $1.26 \times 10^{20}$  and  $3.67 \times 10^{20} \text{ cm}^{-3}$ , respectively. Note that the fitting is not trivial, yet robust, as the model predictions using the same parameters were able to fit a wide range of experimental results with different durations of holding time and different initial strains (Figure 3.2a,b). The model predicts that a faster species of point defects dominates the rapid relaxation in the beginning, while a slower species of point defects governs relaxation with a larger time constant (Figure 3.4). Interestingly, it has been reported that two dominant

types of point defects exist in ZnO, oxygen vacancy and zinc interstitial [234], which is consistent with our results. During relaxation, oxygen vacancies could diffuse from the tensile to the compressive side, while zinc interstitials diffuse in the opposite direction. Note that the diffusivities identified above are larger than those for bulk ZnO at room temperature. Possible reasons for this deviation include: 1) surface-mediated bulk diffusion (in view that for NWs a substantial fraction of atoms lie near free surfaces with atomic structure considerably different from that in the bulk) [29, 235] and 2) reduced activation energy under ultrahigh stress (on the order of GPa) [107]. It is worth pointing out that the current knowledge on room temperature diffusion of point defects in bulk ZnO, and more so in ZnO NWs, is very limited [236]. The present experimental approach can be a useful way to investigate transport and equilibrium properties of point defects in nanomaterials.

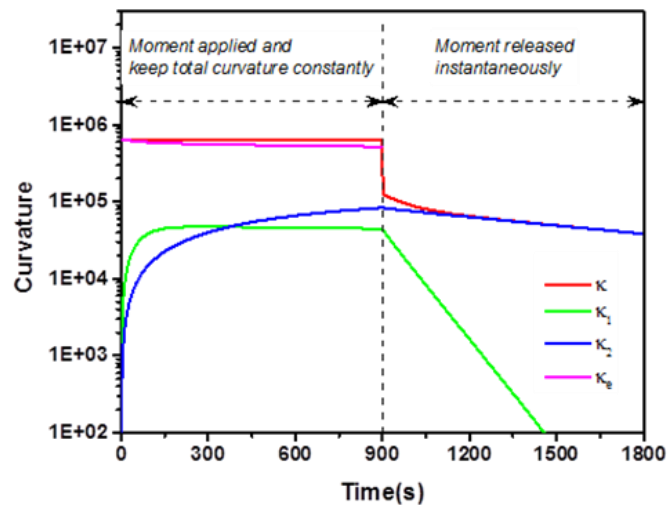


**Figure 3.4** Time-dependent beam curvature for a NW with diameter of 54 nm and initial strain of 1.75% during bending (with a constant total curvature) and release. The NW is held for 900

s at constant total curvature after the initial strain is applied. The red line ( $\kappa$ ) indicates the total curvature of the NW, while the green ( $\kappa_1$ ) and blue ( $\kappa_2$ ) lines indicate the curvatures induced by non-uniform distributions of type 1 and type 2 defects, respectively. The magenta line is the curvature ( $\kappa_e$ ) due to the elastic part.

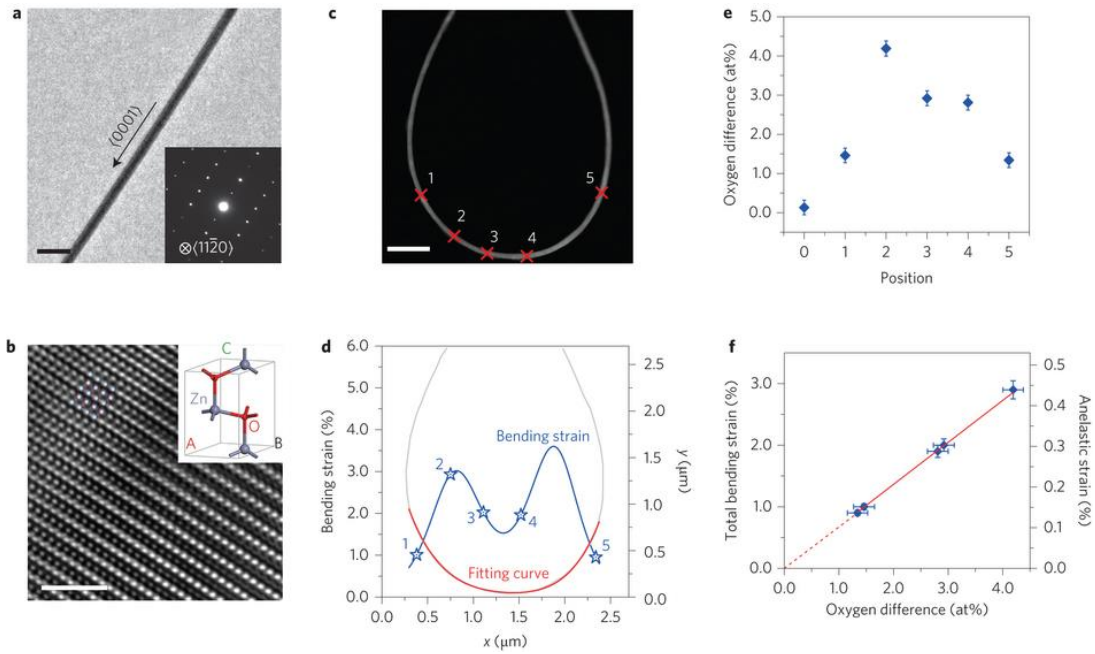


**Figure 3.5** Microstructure and relationship between oxygen difference and bending strain of a ZnO NW. (a) Overview of an individual ZnO NW of 37 nm in diameter with growth direction of  $\langle 0001 \rangle$ . Inset shows the corresponding SAED pattern, at the zone axis of  $\langle 11\bar{2}0 \rangle$ . Scale bar, 100 nm. (b) HRTEM image showing a perfect atomic arrangement in the close-packed layers of  $\{0001\}$ . Inset shows the atomic model of a ZnO unit cell. Scale bar, 2 nm. (c) HAADF-STEM image showing a bent NW for EELS analysis. Scale bar, 0.5  $\mu\text{m}$ . (d) Bending strain as a function of positions in the bent ZnO NW. (e) EELS analysis showing the difference

in oxygen concentration between outer and inner sides of the bent ZnO NW at different positions. Position #0 was taken from a straight part with zero bending strain. Error bars are from the variation in stoichiometry (~0.5 at.%). (f) Linear relationship between the difference in oxygen concentration (between outer and inner sides) and the total bending strain and the anelastic strain.

To corroborate the conclusion that the anelastic behaviour results from diffusion of point defects, further investigation on the defect structures in ZnO NWs was performed. Transmission electron microscopy (TEM) image shows that ZnO NWs are uniform in diameter (Figure 3.5a). The corresponding selected area electron diffraction (SAED) pattern indicates that the NWs are single crystalline wurtzite, with a growth direction along the  $\langle 0001 \rangle$  axis. High-resolution TEM image shows no extended structural defects (e.g., stacking faults or dislocations) (Figure 3.5b).

Aberration-corrected STEM/EELS was employed to investigate the stoichiometry of ZnO NWs under bending. Diffusion of point defects across the diameter would lead to a difference in stoichiometry at the two sides of a bent NW (named as inner side and outer side in the following). Here, an individual ZnO NW protruding from a TEM grid was bent into a loop. Five positions with different bending strains were chosen along the axial direction (Figure 3.5c, d). The quantitative EELS results showed that the atomic percentage of oxygen (i.e., stoichiometry) is different at the inner and outer sides; the outer side is always richer in oxygen than the inner side. By contrast, for un-deformed (straight) regions the inner side and outer side have nearly the same stoichiometry, as expected (Supplementary Section 6). The

same phenomenon was observed in three additional NWs in a similar bending geometry. The differences in oxygen atomic percentage between inner and outer sides for the selected points are shown in Figure 3.5e. The largest difference in oxygen atomic percentage is at Position #3, ~4.2 at.%, which corresponds to the largest total bending strain, ~2.9%. Figure 3f shows a nearly linear relationship between the difference in oxygen concentration and the bending strain as well as the anelastic strain (following Figure 3.2d). The EELS results suggested that during relaxation, more oxygen vacancies diffuse from the tensile (outer) to the compressive (inner) side than zinc interstitials in the opposite direction, leading to higher oxygen percentage in the outer side.

Two conditions are usually necessary for Gorsky relaxation: 1) the point defects must cause lattice distortion, which changes the volume of the host lattice; 2) they must have relatively high mobility. So far, Gorsky relaxation has only been observed in bulk samples with hydrogen (or its isotope) as the most mobile interstitial species [136, 233], with anelastic strain less than  $10^{-6}$ . The observed anelasticity in the present study is four orders of magnitude higher than the largest observed value at the macroscopic scale.

How can Gorsky relaxation lead to the observed large anelasticity in ZnO NWs? Nanostructures can typically withstand ultrahigh stress (on the order of GPa) or strain (on the order of a few percent) [107]. In our study, the bending strain in the ZnO NWs was as large as 5.6% with stress over 8 GPa [127]; by contrast, for hydrogen diffusion in bulk materials [136, 232], the bending strain is usually less than  $10^{-5}$ . The ultrahigh bending stress (strain) applied to the NWs is responsible for the magnitude of the large anelastic strain. According to Eqn. (S8) in Supplementary Section S4, diffusional flux of point defects depends on the gradient in

chemical potential, which in turn depends on the stress gradient. Therefore, the small diffusion distance (i.e., NW diameter), enormous stress gradient and the high diffusivity contribute to the short relaxation (recovery) time scale on the order of minutes.

It should be noted that our theoretical model is more general than the classic Gorsky theory. The classic Gorsky theory predicts a linear relationship between the initial strain and the anelastic strain, while our model predicts a nonlinear relationship when the strain is large. Therefore, the relaxation phenomenon reported in the present study may be referred to as a type of nonlinear Gorsky relaxation. As discussed in Supplementary Section S5, the Gorsky model is a special case of our theoretical model when there is only one type of diffusion species and the applied strain gradient is small.

Anelasticity can lead to energy dissipation (or internal friction), which is of great technological interest. Figure 3.2f shows the hysteretic behaviour of a ZnO NW under compression. Here the energy dissipation can be characterized by the loss factor  $h = \frac{\Delta W}{\rho W_{\max}}$ , where  $\Delta W$  is the dissipated energy per loading-unloading cycle and  $W_{\max}$  is the maximum stored energy per unit volume over the cycle. A high loss factor of ~0.08 is calculated from Figure 3.2f. High-damping materials typically have low stiffness (Young's modulus) [237]. In load-bearing applications, however, both high stiffness and high damping are often desired. A merit index is given by  $\sqrt{E}h$ , where  $E$  is Young's modulus [132]. The merit index for the ZnO NW is remarkably high with a value of 1.13, taking  $E = 200$  GPa for NW diameter of 20 nm [127]. For the purpose of comparison, among the bulk materials traditionally used as high-damping materials, Cu–Mn alloys exhibit the highest merit index of ~0.5. Recently, nanopillars

made of Cu–Al–Ni single crystalline shape memory alloy were reported to have the merit index of  $\sim 0.9$  [132]. Clearly the ZnO NWs exhibit promising potential for mechanical damping and might be used as an efficient damping material in a broad range of applications.

To assess if the observed anelasticity is present in other single crystalline NWs with point defects, we tested p-doped Si NWs and observed similar anelastic relaxation. Figure 3.6a shows that the relaxation in p-doped Si NWs is slower than that in ZnO NWs for the same holding time, indicating slower diffusion of boron dopants in Si NWs (Supplementary Movie 2). Figure 3.6b plots the load-displacement curve of a Si NW under buckling, illustrating a similar hysteretic behaviour with a loss factor of  $\sim 0.025$  and a merit index of 0.36. Preliminary tests on single crystalline Ag NWs showed anelastic behaviour at sufficiently small strains, but at higher strains, dislocation activities induced plastic deformation resulting in incomplete strain recovery.

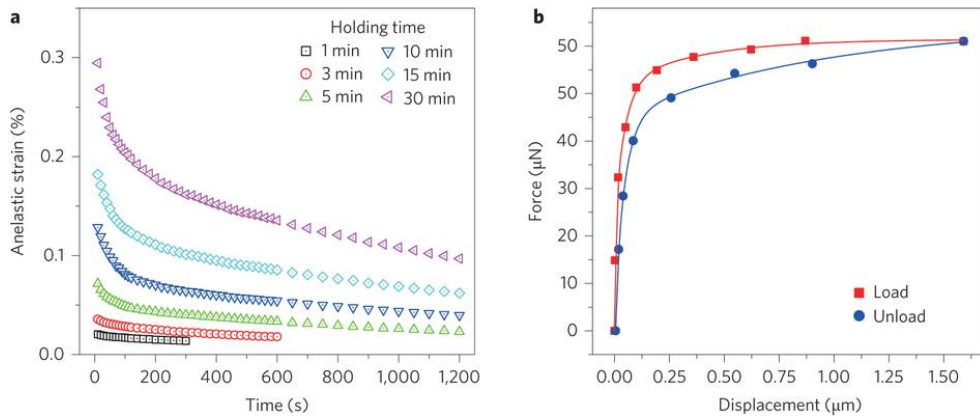


**Figure 3.6** Mechanical behaviors of p-doped Si NWs under bending and compression. (a) Anelastic strain as a function of recovery time for six different durations of holding time. (b) Force-displacement curve of a p-doped Si NW under compression (buckling).

### 3.4 Conclusions

In summary, we have reported large anelastic behaviour in single crystalline NWs governed by stress-gradient-induced migration of point defects. The observed anelasticity was attributed to a type of nonlinear Gorsky relaxation that involves the diffusion of two types of point defects under an inhomogeneous stress field. The large anelasticity in ZnO NWs resulted in high mechanical damping with the merit index of 1.13. Similar anelastic behaviour was found in p-doped Si NWs. The large magnitude of the anelasticity is attributed to the high strain applied to the NWs, while the small diffusion distance, enormous stress gradient and large diffusivity result in the short relaxation (recovery) time scale. The large diffusivity in NWs is due to the surface-mediated bulk diffusion and reduced activation energy under ultrahigh stress. The present study also suggests a useful experimental approach to study transport and equilibrium properties of point defects at the nanoscale. Since point defects have been reported to exist in many nanostructures [238], the reported anelasticity is expected to have broad impacts in nanotechnology. With the rapid progress in large-scale synthesis of NWs [239], our study suggests that crystalline NWs with point defects could serve as highly efficient damping materials for a broad range of applications in aerospace, automotive, energy and biomedical industries.

## CHAPTER 4

# TWINNING, DETWINNING AND SUPERPLASTICITY IN CRYSTALLINE METAL NANOWIRES

Investigation of dislocation nucleation, propagation and interaction is a key to elucidating the deformation mechanisms in metallic materials under applied load. Here, we report transition of deformation modes in bi-twinned Ag nanowires (NWs) with a single twin boundary (TB) running parallel to the NW length via *in situ* transmission electron microscopy (TEM) tensile tests and molecular dynamics simulations. Localized dislocation slip and detwinning-twinning deformation depend on the volume ratio between the two twin variants and the cross-sectional aspect ratio. Specifically, in bi-twinned Ag NWs with balanced volume ratios localized dislocation propagation across the entire cross-section lead to permanent slip and limited fracture strain, while in those with small volume ratios, twinning propagation took place following a detwinning process leading to superplasticity through reorientation of the NW. Both experimental and theoretical results corroborated that interaction of multiple localized dislocations with the TB governs the detwinning process. A criterion is proposed for determining the deformation modes in face-centered cubic metallic NWs containing an internal TB with certain cross-sectional aspect ratio.

## 4.1 Introduction

Nanowires (NWs) are among the most important building blocks for a host of applications including energy harvesting/storage, sensors, flexible/stretchable electronics, and nanoelectromechanical systems,[5, 8, 14, 18-20] to name a few. Operation and reliability of the NW-based devices call for a more thorough understanding of the mechanical behaviors of NWs. Dislocation nucleation from free surfaces has been identified as a dominant deformation mechanism in NWs, in contrast to the forest dislocation dynamics in bulk materials. Extensive studies have been reported for defect-free, single crystalline metal NWs where surface-nucleated dislocations tend to glide across the NW and annihilate at the opposite surfaces.[3, 107, 143, 145, 146, 153, 176-178, 240]. Such NWs exhibit ultrahigh yield strength,[38, 141] typically with limited or no strain hardening and low tensile ductility due to the absence of effective obstacles within the NWs that could block the movement of crystalline defects like dislocations. On the other hand, while as-synthesized NWs typically possess different types of defects such as twin boundaries (TBs) and stacking faults (SFs),[55, 241] few studies have considered the internal microstructure in the NWs. Thus it is of particular interest to study how preexisting defects and internal microstructure can affect the mechanical behaviors of NWs.

Coherent TBs in face-centered cubic (FCC) metals are a special kind of interfaces with much higher thermal and mechanical stability compared to other general high-angle grain boundaries (GBs).[242, 243] NWs with internal TBs, perpendicular, inclined or parallel to the NW length direction,[155, 156, 159, 244, 245] have recently received much attention, owing to their capability to contribute to hardening by acting as effective barriers to dislocation motion. Effective hardening due to perpendicular TBs requires uniformly small twin spacing across the

entire length of NWs,[159] while inclined TBs are prone to migration, leading to grain coarsening through detwinning driven by the finite resolved shear stress on the inclined TBs when the NW is axially loaded.[155] Penta-twinned NWs, each of which has five twin planes joined along a common quintuple line in the axial direction, have been shown to exhibit pronounced strain hardening. However, the penta-twinned structure introduces a complicated internal stress field and additional preexisting defects such as SFs.[102, 106, 246] In addition, the overlapping images of the five twin variants makes it difficult to fully capture dislocation dynamics via *in situ* transmission electron microscope (TEM). A simpler TB structure would be desirable for investigating the deformation mechanisms, especially TB-dislocation interactions, in the confined volume of a NW.

Here, based on *in situ* TEM tensile tests and molecular dynamics (MD) simulations, we report for the first time the deformation mechanisms in the so-called bi-twinned metal NWs, each having a single TB running parallel to the NW length direction. Two distinct deformation modes, localized dislocation slip and detwinning-twinning deformation, are observed in bi-twinned Ag NWs depending on the volume ratio between the two twin variants and the cross-sectional aspect ratio. Specifically, it is found that in bi-twinned NWs with balanced volume ratios, localized dislocation slip across the TB leads to permanent slip and limited fracture strain, while in those with small volume ratios propagation of twinning partials takes place following a unique detwinning process, leading to superplasticity. A criterion for detwinning-twinning deformation in bi-twinned NWs is proposed based on the energy change associated with detwinning to elucidate the effect of volume ratio and cross-sectional aspect ratio on the

transition of deformation mode. Single crystalline Ag NWs were studied for the purpose of comparison, which also exhibited pronounced superplasticity.

## **4.2 Materials and Methods**

### **4.2.1 Sample Synthesis and Characterization**

Crystalline Ag NWs were synthesized by physical vapour deposition inside a molecular beam epitaxy system under ultra-high vacuum condition and substrate temperature of 700 °C. More details of the NW synthesis process are provided elsewhere [38].

Cross-sectional TEM samples of Ag NWs after deformation were prepared with focused ion beam (FIB). High-resolution TEM observations were performed on JEOL 2010F with a Schottky field emission gun (FEG) operated at 200 kV. Atomic resolution high-angle annular dark-field (HAADF) scanning transmission electron microscopy (STEM) imaging was performed on a probe corrected FEI Titan G<sup>2</sup> 60-300 kV S/TEM equipped with an X-FEG source operated at 200 kV.

### **4.2.2 *In Situ* TEM Mechanical Testing**

The mechanical testing was carried out *in situ* inside a TEM using a MEMS based material testing stage, which consists of an electrostatic (comb-drive) actuator, a capacitive load sensor and a gap in between for mounting samples, shown in Figure 4.1a. Details on the testing stage has been reported previously [228]. Displacement (and strain) is measured by digital image correlation of TEM images of two local markers on the specimen (Figure 4.1b).

This MEMS based testing stage has a strain resolution of 0.01% (gage length 2  $\mu\text{m}$ ) and a stress resolution of 1.4 MPa (for example, for NW diameter of 104 nm).

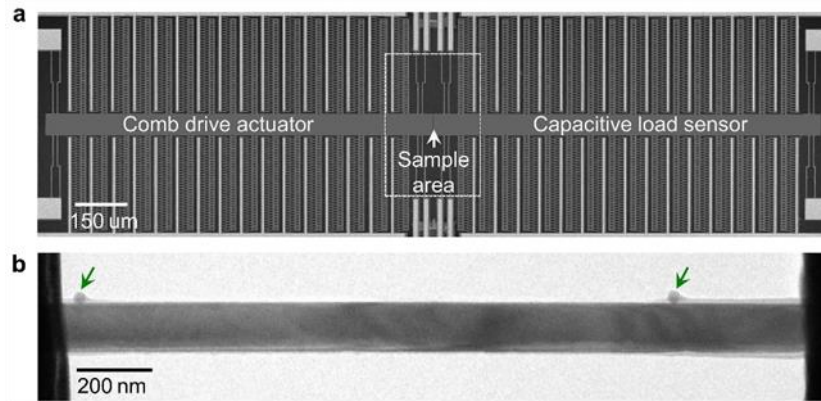


**Figure 4.1** A comb-drive-actuated MEMS based system for *in situ* TEM tensile test. (a) Comb-drive-actuated MEMS based device for tensile test. (b) TEM image showing a NW mounted on the device. Two local markers are deposited on the NW surface for displacement (or strain) measurement.

NWs were mounted on the testing stage using a nanomanipulator (Klocke Nanotechnik, Germany) inside a FEI Nova 600 dual beam SEM. A single Ag NW was welded to the nanomanipulator probe, then mounted to the MEMS stage and clamped by electron-beam-induced Pt deposition at the two free ends. Two local markers were deposited on the NWs for displacement (and strain) measurement. *In situ* TEM mechanical testing was performed on JEOL 2010F operated at 200 kV. The loading and unloading strain rates were  $\sim 0.005$  %/s. Low magnification images were recorded at a fixed condense (the second condense lens) current to

minimize the focus change. The current density of incident e-beam is  $< 0.1 \text{ A/cm}^2$  and its effect on the mechanical behavior of the NW under tensile testing can be neglected.[108, 247-249]

### **4.2.3 MD simulations**

Large-scale MD simulations were performed using the software package LAMMPS[250]. Simulation samples of bi-twinned NWs and single crystalline NWs were generated according to experimentally observed geometries. Figure. 5d shows the atomic cross-section of the bi-twinned NW samples. For each sample, W equals 13 nm and H ranges from 3nm to 10nm, and all samples are 80 nm in length. The embedded atom method potential for Ag[251] was used to describe the interatomic interactions. Periodic boundary condition was imposed along the axial direction (that is, the loading direction  $\langle 110 \rangle$ ) of all simulated samples. The samples were initially relaxed and equilibrated at temperature of 300 K for 800 ps using the Nosé–Hoover[252] thermostat and barostat, followed by stretch at a constant strain rate of  $10^8 \text{ s}^{-1}$  under NVT ensemble (canonical ensemble) until failure. To visualize defects generated during deformation, atoms were painted with different crystalline order in different colors using a common neighbor analysis by OVITO[253]. The green-colored atoms stand for atoms with face-centered cubic symmetry, the red those with hexagonal close-packed symmetry and the grey those at dislocation cores, surfaces and point defects.

## 4.3 Results

### 4.3.1 NW Morphology and *In Situ* TEM Tensile Testing

The Ag NWs in this study exhibited high crystalline quality owing to near-equilibrium growth conditions. Based on TEM characterization, there are two types of Ag NWs with growth direction along a  $\langle 110 \rangle$  direction, bi-twinned and single crystalline, as shown in Figure 4.2. Bi-twinned NWs with a single TB running parallel to the NW length direction are dominant (81%) in the examined 113 NWs (see details in Supplementary Section 1). Figure 4.2a,b shows schematic drawings of the morphology of the bi-twinned and single crystalline NWs, respectively. The corresponding cross-sectional TEM images of the two types of NWs are shown in Figure 4.2c,d. Both show hexagonal cross-sectional shapes but with different arrangement of surface facets (marked in Figure 4.2a,b). High-resolution TEM image in Figure 4.2e shows that the internal TB in a bi-twinned NW is highly coherent without other line or planar defects as in the case of penta-twinned metallic NWs [102].

We performed *in situ* TEM tensile testing of individual NWs using a testing stage based on a microelectromechanical system (Figure 4.1a) that allows accurate measurements of both load and displacement simultaneously, [202, 220, 228] as well as real-time imaging of microstructure evolution during deformation. Figure 4.3 shows stress-strain responses and snapshots of microstructure evolution for typical tensile tests of two bi-twinned and one single crystalline Ag NWs. Insets in Figure 4.3a-c are the corresponding cross-sectional TEM images of the tested NWs taken from the undeformed parts on the supported beams of the MEMS based device after the tensile tests. Note that bi-twinned NWs were identified first from the

longitudinal view based on the  $19.4^\circ$  tilt angle between  $\langle 1\bar{1}0 \rangle$  and  $\langle 001 \rangle_t$  from the two twin variants (Figure 4.3a) and then verified by the cross-sectional TEM images. From the cross-sectional images (the insets in Figure 4.3a,b), the two bi-twinned NWs show different volume ratios ( $V_{\text{small}}/V_{\text{large}}$ ) between the two twin variants, 0.64 and 0.19 in the insets of Figure 4.3a,b, respectively.

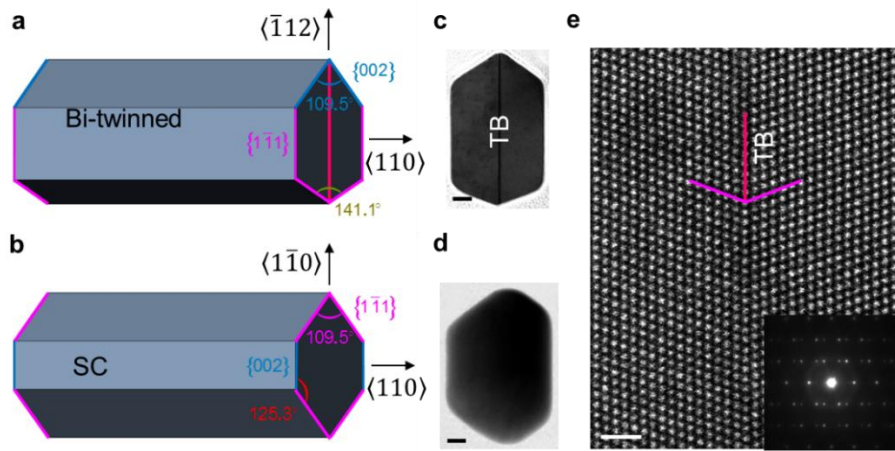


**Figure 4.2** Characterization of crystalline Ag NWs. (a,b) Schematic drawings of bi-twinned and single crystalline NWs, respectively. (c,d) Cross-sectional TEM images of bi-twinned and single crystalline NWs, respectively. Scale bar, 20 nm. (e) A cross-sectional HRTEM image of a bi-twinned Ag NW. Inset in (e) is the corresponding selected area electron diffraction (SAED) pattern. Scale bar, 1 nm.

As shown in Figure 4.3, one bi-twinned NW with a balanced (or large) volume ratio exhibited a limited fracture strain (4.2%, Figure 4.3a,d), while the other with a small volume

ratio showed superplasticity (an elongation of 27.5% measured between the two deposited local markers, Figure 4.3b,e), comparable to superplasticity in the single crystalline NW (an elongation of 37.5% for the fully deformed part between the two local markers, Figure 4.3c,f). Moreover, the yield strength and the ultimate tensile strength (UTS) of the bi-twinned Ag NWs, regardless of the deformation mode, were found to be 1.21-1.31 and 1.5 GPa, respectively, which are higher than those of the single crystalline NWs (0.95 GPa and 1.21 GPa). More details of the stress-strain curves can be seen in Supplementary Section 2. These results suggest that the internal TB running parallel to the NW length direction can act as obstacles for dislocation nucleation and propagation so as to strengthen the NWs.

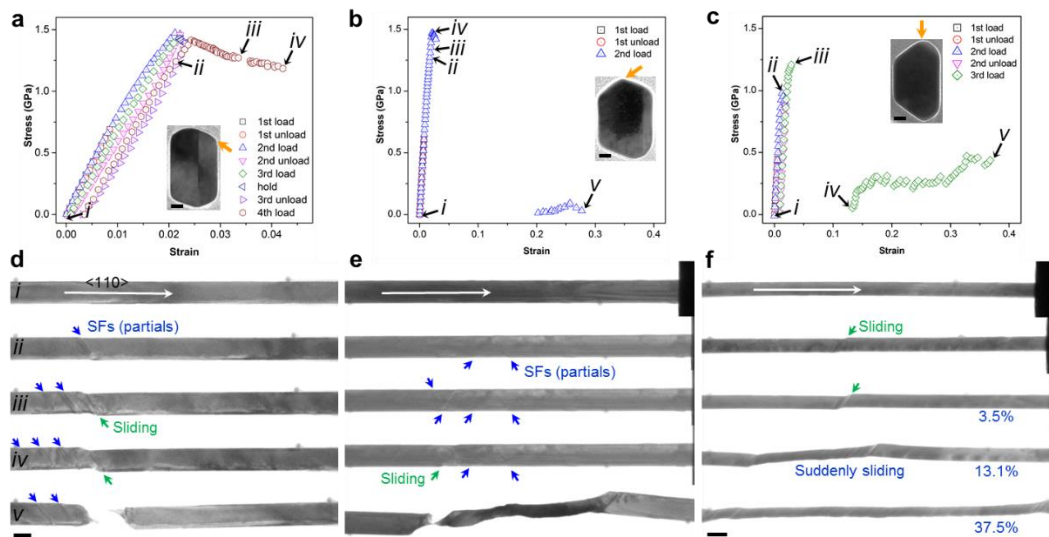


**Figure 4.3** Mechanical response and microstructure evolution of crystalline Ag NWs under *in situ* TEM tensile test. (a-c) Engineering stress-strain curves of bi-twinned and single crystalline Ag NWs under uniaxial loading-unloading. Insets in (a-c) are the corresponding cross-sectional images of the tested NWs (cut from the undeformed part after the test). Scale bar, 20

nm. (d-f) Snapshots of microstructure evolution of bi-twinned and single crystalline Ag NWs during the loading-unloading processes. The five snapshots corresponding to the stress-strain change are marked in (a-c). The loading direction is  $\langle 110 \rangle$ , which is also the length (or growth) direction of the NWs. Partial dislocations are marked by blue arrows and planar sliding by green arrows. Scale bar, 100 nm. The viewing directions are from the  $\langle 1\bar{1}0 \rangle$  zone axis of the small twin variant in (d), the large twin variant in (e) and the whole grain in (f), which are marked by the yellow arrows in the insets in (a-c), respectively.

### 4.3.2 Three Deformation Modes

Localized dislocation nucleation and propagation dominated in bi-twinned Ag NWs with a balanced volume ratio, shown in Figure 4.3d (viewed from the  $\langle 1\bar{1}0 \rangle$  zone axis of the small twin variant; see details in Supplementary Section 3). As shown in Figure 4.3a,d, partial dislocations marked by blue arrows emerged at the yielding point (Figure 4.3d-ii). After that, partial dislocations were continuously nucleated under increasing applied stress, leading to permanent plastic deformation (planar sliding) in the NW (Figure 4.3d-iii) as they swiped across the whole cross-sectional area. Continuous dislocation nucleation and propagation resulted in large plastic deformation and failure of the NW (Figure 4.3d-iv,v and Supplementary Movie 1). Note that only dislocation slip was observed without obvious necking at the fracture region. Figure 4.4a shows a magnified TEM image of the fracture morphology in which a high density of SFs was left in the small twin variant (see details in Supplementary Section 3), whereas the partials observed in Figure 4.3d during the plastic deformation were from the large twin variant. This indicates that partial dislocations are prone

to nucleation and propagation in the dominant twin variant in bi-twinned NWs during the plastic deformation. According to the MD simulation results in Figure 4.4b (see Supplementary Movie 4 for more details) and a schematics of the slip systems [73, 147] shown in Figure 4.4c, a partial dislocation,  $\alpha\mathbf{B}$  from plane  $\mathbf{BCD}$  (or  $\beta\mathbf{A}$  from plane  $\mathbf{ACD}$ ), nucleated from a surface vertex (Figure 4.4b-i), propagated into the dominant twin variant towards the TB (Figure 4.4b-ii), then interacted with the TB and transmitted into the small twin variant through a dislocation reaction,  $\alpha\mathbf{B} \rightarrow \alpha\alpha' + \alpha'\mathbf{B}$  (Figure 4.4b-iii), leaving a stair-rod dislocation  $\alpha\alpha'$  with a magnitude of  $\frac{2}{9}\langle 1\bar{1}1 \rangle$  across the TB (see Supplementary Section 4). After that, the trailing partial ( $\mathbf{C}\alpha$  in plane  $\mathbf{BCD}$ ) was nucleated (Figure 4.4b-iv) and swept through the defected area ( $\mathbf{C}\alpha \rightarrow \mathbf{C}\alpha' + \alpha'\alpha$ ), resulting in a permanent slipping step (one atomic layer along  $\mathbf{CB}$ ) in the bi-twinned NW (Figure 4.4b-vi).

In contrast to the dislocation slip dominated deformation described above, large plasticity was observed in the bi-twinned Ag NWs with small volume ratios (Figure 4.3b,e). After a careful microstructure characterization, a detwinning-twinning deformation was identified to contribute to the large plasticity in such bi-twinned NWs (see details in Supplementary Section 2 and Movie 2). Before the detwinning-twinning deformation, dislocations were nucleated and propagated in the dominant twin variant when the applied stress approached the yield strength (Figure 4.3e-ii,iii); with further loading a permanent planar slip also occurred (Figure 4.3e-iv). Different from the bi-twinned NW dominated by dislocation slip, the dislocations in this case nucleated and propagated in both  $\{111\}$  and  $\{11\bar{1}\}$  planes (planes  $\mathbf{BCD}$  and  $\mathbf{ACD}$  in Figure 4.4c) and intersected at the TB. The interaction of multiple dislocations with the TB led to detwinning of the existing TB, followed by the

nucleation and propagation of new inclined TBs (marked in Figure 4.3e-v) along the NW length. This deformation mechanism is significantly affected by the volume ratio between the two twin variants.

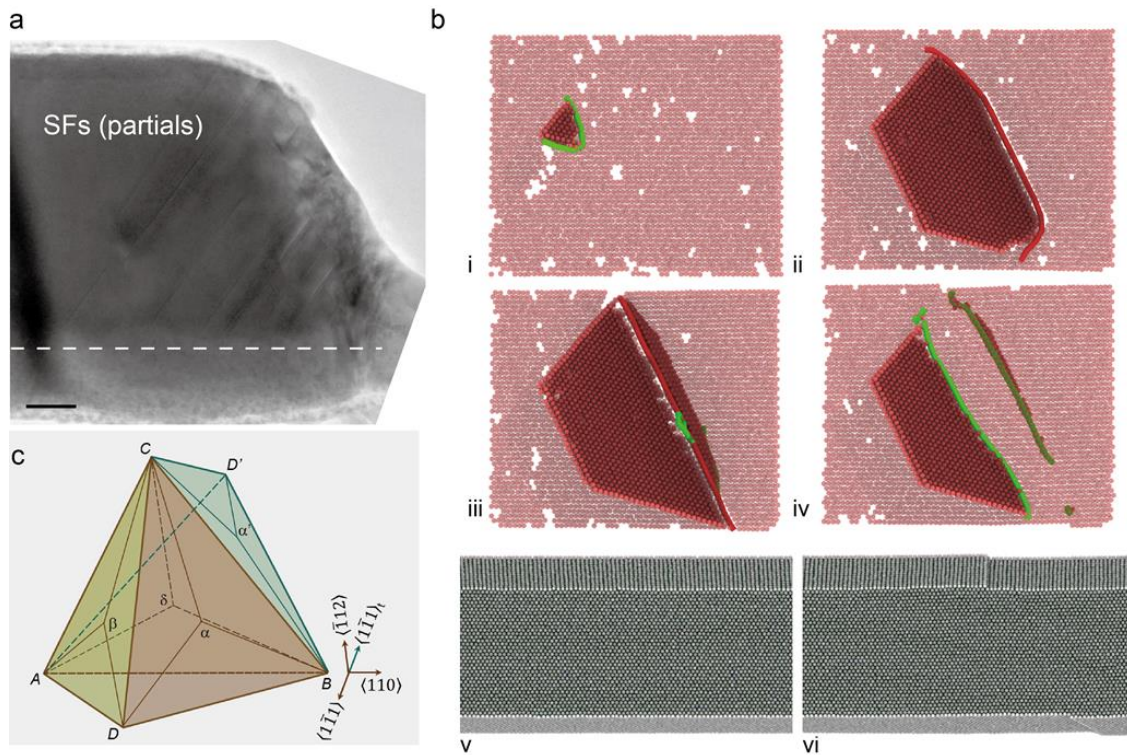


**Figure 4.4** Dislocation slip dominated deformation in bi-twinned Ag NWs. (a) A magnified TEM image showing stacking faults left in the small twin variant at on-zone condition. The surface edge of the small twin variant is marked by the dashed line. Scale bar, 20 nm. (b) Snapshots from MD simulations showing nucleation, propagation of partial dislocations and interaction between the partial and the TB in bi-twinned Ag NWs. (c) Illustration of a double

Thompson tetrahedron on the coherent  $\{1\bar{1}1\}$  TB in bi-twinned NWs. The front tetrahedron at the front of the TB represents the matrix slip systems in the dominant twin variant, while the back one represents twin slip systems in the small twin variant.

To understand further the detwinning-twinning mechanism in bi-twinned metallic NWs, we have performed a series of MD simulations. Details of the simulation are provided in the ‘Methods’ section. Figure 4.5a shows a perfect TB parallel to the NW axis before loading and Figure 4.5b shows the NW after detwinning, where a single crystalline phase was formed and part of the original twin plane disappeared (only hexagonal close-packed atoms are shown here). Detailed detwinning process is illustrated in Figure 4.6 (see Supplementary Movie 7). Partials initially interacted with the TB and left a stair-rod dislocation  $\alpha'\alpha$  (Figure 4.6a), similar to the initial stage in bi-twinned NWs with balanced volume ratio (Figure 4.4b). After that, direct interaction of two partials,  $\alpha B$  and  $\alpha C$  in plane  $BCD$  (Figure 4.4c), formed a temporary partial  $D\alpha$  (Figure 4.6b), which would decompose into a stair-rod dislocations  $\alpha\delta$  and a Hirth dislocation,  $1/3\langle 010 \rangle$  (Figure 4.6c). Because of the high energy state of the two new formed dislocations, an extended jog was formed among them with a new partial  $\delta C$  in plane  $ABC$  which is for detwinning (Figure 4.6d,e). Subsequent dislocation nucleation, propagation and interaction continued the detwinning process, following with twinning deformation in the temporary formed structure. As a result, a low energy TB in the dominant twin variant and a high-angle GB in the other twin variant were created; under further loading twinning partials kept nucleating on the newly formed TB as shown in Figure 4.5f, leading to migration of the inclined TB and GB, and creation of an expanding single crystalline phase

(see Supplementary Section 2). Figure 4.5e,g shows the cross-sections of the original bi-twinned phase and the newly formed single crystalline phase, respectively. The bi-twinned NW with  $\langle 110 \rangle$  axis was transformed to the single crystalline phase with  $\langle 001 \rangle$  axis by coherent twinning migration from the detwinning site, which is somewhat similar to the deformation mechanism in single crystalline Ag NWs that will be discussed below. Figure 4.5h,i shows the fracture morphologies of the detwinning-twinning dominated bi-twinned Ag NWs from experiments and MD simulations, respectively. The fact that MD simulations matched quite well with the experimental results indicates that the detwinning-twinning mechanism can lead to large plasticity in bi-twinned NWs.

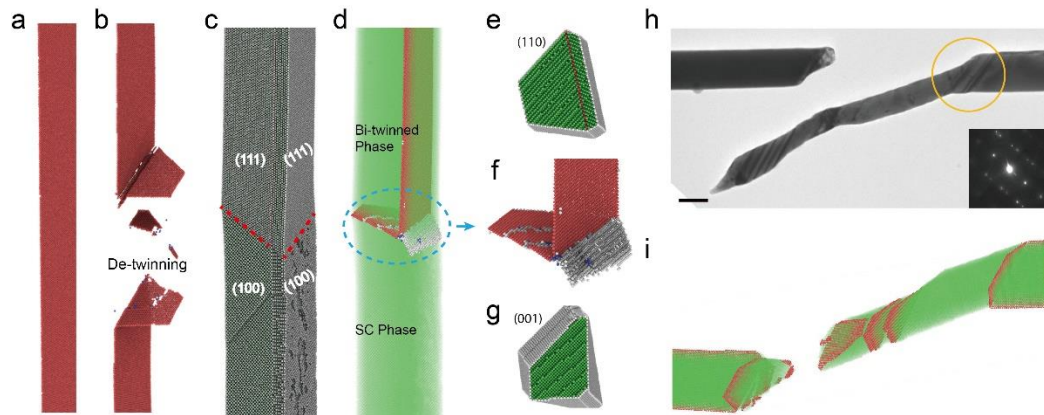


**Figure 4.5** Illustration of detwinning-twinning deformation in bi-twinned Ag NWs. (a) A perfect TB in the bi-twinned NW before loading. (b) Detwinning of the bi-twinned NW above a critical load. Note that only HCP atoms are made visible in (a,b). (c) Nucleation of a single crystalline phase in the bi-twinned NW, the side surfaces being reoriented from (111) to (100). (d) Internal structure of the detwinned NW. The FCC atoms have been made transparent. (e) Cross-section of the bi-twinned phase with axial direction of  $\langle 110 \rangle$ . (f) Detailed structure of

the newly formed GBs during the detwinning process. (g) Cross-section of the single crystalline phase with axial direction reoriented to  $\langle 001 \rangle$ . (h,i) Fracture morphology of detwinning dominated bi-twinned Ag NWs from experimental and simulation investigations, respectively. A SAED pattern in the inset of (h) indicates the twin relationship between the newly formed single crystalline phase and the original dominant twin variant in the bi-twinned phase.

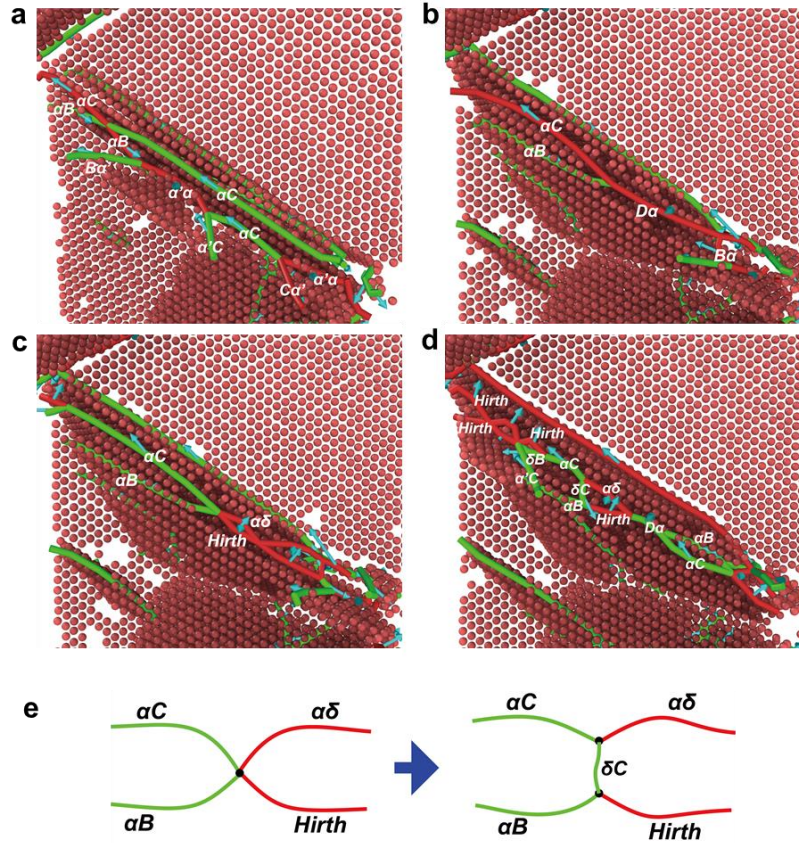


**Figure 4.6** MD simulations showing dislocation evolution for detwinning-twinning deformation in bi-twinned NW. (a-d) Snapshots from MD simulations showing detwinning

processes in a bi-twinned NW with small volume ratio. (e) Illustration of an extended jog formed with a new partial  $\delta C$  in plane  $ABC$  for detwinning.

For the purpose of comparison, *in situ* tensile testing of single crystalline Ag NWs was also performed, as shown in Figure 4.3c,f, where superplasticity was observed as a result of twinning induced deformation. The microstructure evolution in the single crystalline Ag NW during the plastic deformation is illustrated in Figure 4.3f (see Supplementary Movie 3). At the yielding point, leading partials were nucleated from the NW free surface and propagated across the NW cross section, which resulted in a permanent planar slip (Figure 4.3f-ii). Continuous nucleation and propagation of the leading partials caused a small deformed segment (Figure 4.3f-iii) followed by a sudden, large elongation (13.1%) of the NW accompanying a nearly full release of the applied stress (Figure 4.3f-iv). After that, the NW underwent a continuous twinning deformation with the increase of the applied load (Figure 4.3f-v). Postmortem TEM observations revealed that the single crystalline Ag NW was completely reoriented from  $\langle 110 \rangle$  to  $\langle 100 \rangle$  direction (see the cross-sectional TEM images before and after deformation in the insets in Figure 4.7a). Similar twinning deformation was observed in single crystalline Au NWs [152]. In comparison, a high density of defective structures (nanotwins and SFs, marked in Figure 4.7a) was observed in the single crystalline Ag NW, while only a few parallel nanotwins in the single crystalline Au NW. To explain this, we calculated the generalized SF energy curve for Ag and compared the results with other FCC metals, as shown in Table 4.1. It has been proposed that  $\gamma_{USF}/(\gamma_{UT} - \gamma_{ISF})$  can describe the competition between partial nucleation and twinning, where  $\gamma_{USF}$  is the unstable SF energy,

$\gamma_{UT}$  the unstable twinning energy and  $\gamma_{ISF}$  the intrinsic SF energy [153]. For  $\langle 110 \rangle$  oriented Ag under tension, the value of  $\gamma_{USF}/(\gamma_{UT} - \gamma_{ISF})$  is 1.08, which is very close to 1 compared to other FCC metals. This means that partial nucleation and twinning are almost equally probable to occur, which explains the appearance of a high density of nanotwins and SFs in the deformed single crystalline Ag NW. MD simulations showed that the nucleation of leading partials will generate nanotwins and SFs in the NW (Figure 4.7b), and when migration of the inclined TB crosses the nanotwins and SFs, they will be left behind in the NW (see Figure 4.7b and Supplementary Movie 8).

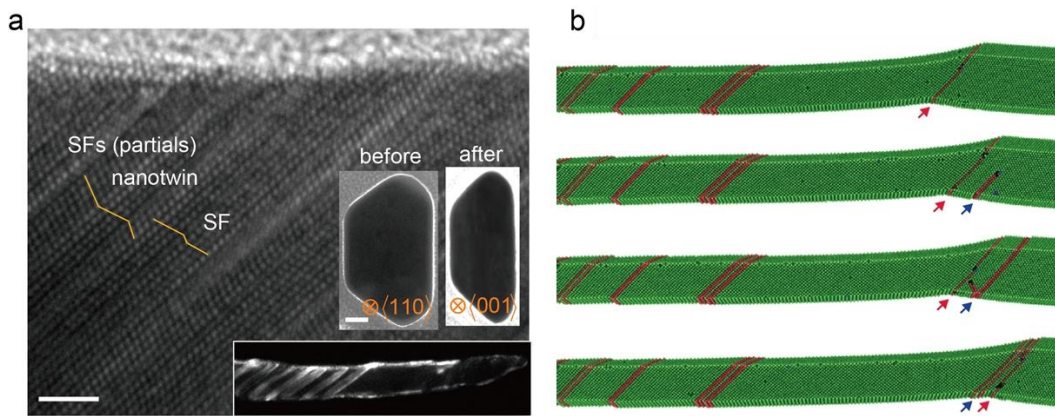


**Figure 4.7** Twinning deformation in single crystalline Ag NWs. (a) A high-resolution TEM image of defective structures (nanotwins and SFs) in the deformed part of a single crystalline Ag NW after the *in situ* tensile testing. Scale bar, 2nm. Insets in (a) are the cross-sectional images of single crystalline Ag NW before and after deformation. Scale bar, 20 nm. (b) Snapshots from MD simulations showing the generation of SFs and nanotwins during the twinning deformation in a single crystalline Ag NW. Leading partials for twinning propagation and SFs or nanotwinns are marked by red and blue arrows, respectively.

In short, it is shown that detwinning-twinning deformation leads to the observed large plasticity in bi-twinned NWs with a small volume ratio, characterized by interaction of multiple dislocations with the TB, which is different from dislocation slip dominated deformation in bi-twinned NWs with balanced volume ratios and twinning dominated deformation in single crystalline NWs. The three deformation mechanisms were observed in more Ag NWs (see additional examples in Supplementary Section 2) and supported by MD simulations (see Supplementary Section 4 and Movie 4-6).

Detwinning has been extensively studied recently especially in fcc metals.[154, 155, 254, 255] The key for detwinning is to nucleate a partial in the twinning plane at the TB. Zhu *et al.*[254] proposed a detwinning mechanism via cross-slip of partials into the twinning plane at the TB. Subsequent dislocation interactions with the TB continue the detwinning process. Wang *et al.*[255] attributed the detwinning to the rapid migration of incoherent TBs formed by twinning partials during compressive loading. Twinning partials from the incoherent TBs can directly activate the detwinning process owing to the shear stresses. Moreover, detwinning has been observed in Cu nanopillars[155] and Au NWs[154] with preexisting nanotwins under tension and compression, respectively. In these two cases, twinning partials were directly nucleated from the free surface and transferred into the twinning plane owing to the large resolved shear stress. In contrast, the detwinning mechanism reported here is a unique process because the loading direction is parallel to the twinning plane and there is no resolved shear stress. Therefore, the previous detwinning mechanisms cannot be readily applied. Alternatively, we propose that complicated dislocation interactions with the TB can disorder

the local atomic arrangement, leading to a twinning partial in the twinning plane for detwinning.

**Table 4.1** Important features on the GSF curves for various FCC metals

	EAM				TB [256]
	Cu [153]	Au [153]	Al [153]	Ag [251]	Ag
$\gamma_{ISF}$ (mJ m <sup>-2</sup> )	45	31	146	19	18
$\gamma_{USF}$ (mJ m <sup>-2</sup> )	180	101	189	129	93
$\gamma_{UT}$ (mJ m <sup>-2</sup> )	202	122	240	138	105
$\gamma_{USF} / (\gamma_{UT} - \gamma_{ISF})$	1.147	1.11	2.011	1.084	1.069

### 4.3.3 Effects of Volume Ratio and Cross-sectional Aspect Ratio

Apparently, detwinning plays a crucial role in the superplasticity of bi-twinned NWs; without the detwinning and nucleation of a single crystalline phase, twinning migration and NW reorientation would not occur in the bi-twinned phase. After the detwinning, a single crystalline phase (the same as the dominant twin variant) is formed, which will be subsequently deformed by twinning. After this detwinning-twinning process a complex structure is formed as shown in Figure 4.5d,f – a low energy TB in the dominant twin variant and a high-angle GB in the other twin variant. The energy change associated with the detwinning-twinning process can be calculated as the energy needed to create these new boundaries:

$$\Delta E = 2A_1\gamma_{twin} + 2A_2\gamma_{GB} \quad (1)$$

where  $A_1$  and  $A_2$  are the area of the TB and high-angle GB in Figure 4.5f;  $\gamma_{twin}$  and  $\gamma_{GB}$  are the interfacial energies of TB and the newly formed high-angle GB, with the values of 5.9 and 539

mJ/m<sup>2</sup>, respectively (See Supplementary Section S5). This energy change as a function of the volume ratio for a fixed  $H = 9$  nm and  $W = 13$  nm NW is plotted in Figure 4.8a. The volume ratio in bi-twinned NWs can be quite different, ranging from 0.1 to 1.0 in the 20 NWs examined. It is obvious that  $\Delta E$  can be reduced by decreasing the volume ratio, indicating that a reduced volume ratio can facilitate the detwinning process in bi-twinned Ag NWs.

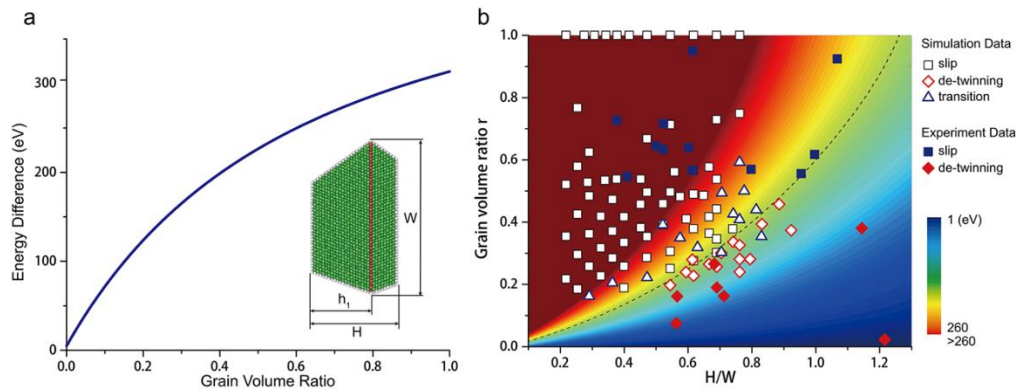


**Figure 4.8** Transition of deformation mechanisms in bi-twinned Ag NWs. (a) Energy difference associated with the detwinning process as a function of the twin volume ratio for a sample with fixed  $W$  and  $H$ . Inset in (a) shows the cross-section of a typical bi-twinned NW in MD simulation and its corresponding geometrical parameters. (b) The contour plot of energy difference in the detwinning process as a function of  $H/W$  and twin volume ratio  $r$ , along with the simulation and experimental data. For simulation results: the black squares stand for the slip dominated deformation mode, the red rhombuses stand for the detwinning-twinning deformation mode and the blue rhombuses stand for the transitional deformation mode. For experiment data: solid black squares stand for the slip dominated deformation mode and solid red rhombuses stand for the detwinning-twinning deformation mode.

To systematically investigate the transition of the two deformation mechanisms, a parameter study was conducted for the bi-twinned NWs using MD simulations. Inset in Figure 4.8a shows the cross-section of the simulated bi-twinned NWs, where  $W$ ,  $H$  and  $h_1$  are the geometrical parameters to be adjusted. The energy difference of the detwinning process  $\Delta E$  in equation (1) can be expressed in terms of two dimensionless parameters:  $H/W$  and volume ratio  $r \in (0,1]$ :

$$\Delta E(A_1, A_2) = \Delta E(W, H, h_1) = \Delta E(H/W, r) \quad (2)$$

The detailed form of the equation is derived in Supplementary Section S5. The contour of  $\Delta E$  is plotted in Figure 4.8b for a fixed  $H = 8.9$  nm, where the x-axis is  $H/W$  and the y-axis is  $r$ . The color from blue to red indicates an increase in  $\Delta E$ . The plot shows that NWs with smaller volume ratio and larger  $H/W$  values have lower energy change, thus favor detwinning; while those with larger volume ratio and smaller  $H/W$  value have higher energy change, thus favor a dislocation slip dominated deformation mechanism.

As shown in Figure 4.8b, the MD simulations suggested a transition deformation mode in between the two deformation mechanisms. More details of the transition mode are shown in Supplementary Section 4. In this mode, dislocation slip first dominated, leading to a necking of the NW in the  $W$  direction, which increased the  $H/W$  value in the necking region. This geometrical change made detwinning more favorable in the necked region, as indeed observed in the simulations. The simulation results are generally predictable based on the behavior of  $\Delta E$ . In addition, a total of 20 experimental data were included in Figure 4.8b (solid symbols), which also showed good agreement with the prediction based on  $\Delta E$ .

Based on the experimental and simulation results, a transition line, corresponding to a critical  $\Delta E$  of 140eV, is found to separate the dislocation slip mechanism and the detwinning-twinning deformation mechanism in bi-twinned Ag NWs (Figure 4.8b). The transition mode of mixed deformation mechanisms was frequently seen around this transition line.

#### **4.3.4 Effect of Twin Boundaries**

Preexisting TBs in metallic NWs have received much interest as a strengthening mechanism due to their capability in blocking the dislocation movement. From the synthesis perspective, it is much simpler to controllably introduce TBs in NWs that are parallel to the length direction. For instance, penta-twinned NWs are commonly synthesized by the polyol method [56] and bi-twinned NWs reported in this study can be synthesized by physical vapor deposition [38].

The mechanical behavior of penta-twinned Ag NWs has been widely studied. [103, 106, 126, 182] For comparison, we list typical mechanical properties of single crystalline, bi- and penta-twinned Ag NWs in Table 4.2. Note that all listed NWs have cross-sectional areas corresponding to a diameter in the range of 95-120 nm so as to avoid the size effect. The bi-twinned Ag NWs exhibit the highest yield strength (1.2-1.4 GPa) and ultimate tensile strength (1.5-1.8 GPa). Depending on the deformation mode, the total elongation of the bi-twinned NWs can range between 3.5% and 27.5%, which is comparable to that of penta-twinned NWs and single crystalline NWs, respectively. Penta-twinned Ag NWs have a similar yield strength of 0.8-1.1 GPa but a larger UTS of 1.1-1.5 GPa, compared to the single crystalline counterparts. The large UTS of penta-twinned NWs has been attributed to strong strain hardening rates since

the internal TBs can act as effective obstacles to hinder the propagation of dislocations through the TBs. [106] From the perspective of material design, metallic NWs with a single TB parallel to the length direction offer the best combined mechanical properties.

**Table 4.2** Mechanical properties of single crystalline, bi- and penta-twinned Ag NWs under uniaxial tensile testing. Note that all the three type NWs have closed cross-sectional areas corresponding to a diameter ranging from 95-120 nm (treated as round shape) so as to avoid the size dependent effect on the Young's modulus.

	single crystalline	Bi-twinned	Penta-twinned
<b>Young's Modulus (GPa)</b>		82±2.2	
<b>Yield Strength (GPa)</b>	0.8-1.0	1.2-1.4	0.8-1.1
<b>Ultimate Strength (GPa)</b>	1.0-1.2	1.5-1.8	1.1-1.5
<b>Total Elongation (%)</b>	35-41	3.5-27.5	1.9-3.8
<b>Number of tested NWs</b>	5	17	13

The effect of TBs parallel to the NW length direction on the deformation behavior of Ag NWs is summarized in Table 4.3. First, twinning is identified as the dominant deformation mechanism in single crystalline Ag NWs, while detwinning-twinning in bi-twinned NWs with small volume ratios, both leading to superplasticity. In contrast, localized dislocation slip are common in bi-twinned NWs with balanced volume ratios and penta-twinned NWs as a result of limited fracture strain. Second, planar sliding (or shearing) is the dominant failure mode in single crystalline and bi-twinned NWs due to partial dislocation sliding across the entire cross-

section while serious necking in penta-twinned NWs owing to complicated dislocation interactions at the intersection of multiple TBs [106, 157]. Third, the interaction of dislocations with TBs introduces obvious hardening in bi- and penta-twinned [106] NWs but the generation of defective structures provides limited hardening in single crystalline NWs. Finally, recoverable plasticity are observed in both bi- and penta-twinned NWs but not in single crystalline NWs since the internal TBs play an essential role in the retraction of partial dislocations.

**Table 4.3** Summary of the mechanical behaviors of single crystalline, bi- and penta-twinned Ag NWs under uniaxial tensile testing.

	Single crystalline	Bi-twinned		Penta-twinned	
		Small vol. ratio	Large vol. ratio		
<b>Deformation mode</b>	Twinning	Detwinning-twinning		Dislocation slip	
<b>Plasticity</b>		Superplasticity		Limited plasticity	
<b>Failure mode</b>		Planar sliding			Necking
<b>Strengthening</b>	Limited		Medium	Strong	
<b>Recoverable plasticity</b>	No		Limited	Strong	

#### 4.4 Conclusions

In summary, we have discovered a transition between two deformation modes, dislocation slip and detwinning-twinning, in bi-twinned metallic NWs via an integrated

approach combining *in situ* TEM tensile testing, microstructure characterization and MD simulations. Localized dislocation nucleation and propagation across the TB lead to permanent planar sliding and limited fracture strain in bi-twinned NWs with balanced volume ratios, while detwinning-twinning deformation results in superplasticity in those with small volume ratios. The superplasticity observed in bi-twinned metallic NWs is somewhat similar to that in single crystalline metallic NWs due to coherent twinning propagation. Our experimental and theoretical results indicated that the detwinning process is governed by interaction of multiple localized dislocations with the TB. A criterion for the detwinning deformation was proposed based on the detwinning energy barrier, which was shown capable of capturing the effects of the volume ratio and cross-sectional aspect ratio on the transition of deformation modes in bi-twinned NWs. Among the single crystalline, bi- and penta-twinned Ag NWs, bi-twinned Ag NWs offer the best combined mechanical properties.

## CHAPTER 5

### RECOVERABLE PLASTICITY IN BI-TWINNED SILVER

#### NANOWIRES

Metallic nanowires (NWs) with multiple twin boundaries (TBs) running parallel to the NW length direction exhibit unusual time-dependent mechanical behavior owing to the interaction of dislocations with TBs. Here, based on *in situ* TEM tensile testing and atomistic simulations, we report recoverable plasticity in bi-twinned Ag NWs with a single TB running parallel to the NW length direction. *In situ* tensile experiments show that bi-twinned Ag NWs undergo stress relaxation on loading at an initial stress around the yield point and plastic strain recovery on unloading. Both experimental and simulated results corroborate that stress relaxation originates from the nucleation of leading partial dislocations from the free surface, while strain recovery is due to the reverse motion of partial dislocations driven by the repulsive force from the TB. The internal TB in bi-twinned NWs can act as an obstacle for hindering dislocation propagation through the entire cross-section. The observed recoverable plasticity in twinned NWs shows new insight on the understanding of interactions between dislocations and TBs in twinned metallic nanomaterials.

#### 5. 1 Introduction

Nanowires (NWs) are among the most important building blocks for many applications, including nanoelectronics, optoelectronics, energy harvesting and storage,

ultrasensitive sensing and nanoelectromechanical devices. [4-6, 8, 10, 12, 19, 257] NWs usually exhibit ultrahigh mechanical strength, which make them ideal candidates for studying fundamental deformation mechanism at nanoscale. [3, 38, 107, 113, 141, 154, 159] In the case of metallic NWs, dislocation nucleation from free surfaces has been identified as a dominant mechanism, in contrast to the forest dislocation dynamics in bulk materials. [102, 143, 146, 153, 174-177, 179, 180] Recently, time-dependent mechanical behavior of metallic NWs under sustained or cyclic loadings has attracted much attention owing to the importance for the design of functional and reliable NW-based electronic devices. [102, 182]

Previous studies have revealed substantial time-dependent and partially reversible deformation behaviors in nanocrystalline thin films, which are attributed to the coupling and competition of reversible dislocation activities and grain boundary (GB) mediated processes at different temperature and strain rates. [165-169] But only a few works have been focused on nanoscale structures like metallic NWs, since they are most single crystalline without GBs or have internal twin boundaries (TBs) which have low energy, high symmetry and coherent atomic structure. [102, 182] Metallic NWs with internal microstructures have received much attention in the past decade, for example, metallic NWs with parallel, inclined or perpendicular TBs with respect to the NW length direction. [103, 106, 155-159, 258] Pre-existed TBs as internal structure in metallic NWs have been demonstrated to effectively improve the mechanical strength, especially for the NWs with inclined or perpendicular TBs with respect to the NW length direction since they can act as obstacles for dislocation nucleation. [155, 159] But no obvious time-dependent mechanical behavior is observed in such NWs with inclined or perpendicular TBs. However, NWs with multiple TBs parallel to the NW length direction

have been reported to exhibit unusual time-dependent mechanical behavior. A complete recoverable plasticity has been observed in penta-twinned Ag NWs with five TBs running parallel to the NW length direction, with stress relaxation on loading and complete strain recovery on unloading. [102] Interaction between dislocations and multiple TBs were considered to contribute to the full plastic strain recovery in penta-twinned NWs. Recoverable plasticity has also been predicted in bi-twinned Ag NWs [102] (for consistent with the reported penta-twinned NWs) with a single TB running parallel to the NW length direction but there is lack of experimental evidence and the interaction between dislocation and single TB remains elusive.

Here, we report recoverable plasticity in bi-twinned Ag NWs via *in situ* TEM tensile tests combined with molecular dynamics (MD) simulations. *In situ* tensile experiments show that bi-twinned Ag NWs undergo stress relaxation at a stress level close to the yield point and plastic strain recovery during the unloading process. Both experimental and simulated results corroborate that stress relaxation originates from the nucleation of leading partial dislocations, while strain recovery is due to the reverse motion of partial dislocations driven by the repulsive force from the TB. Effect of TB on the dislocation propagation in bi-twinned NWs is studied by comparing the case in single crystalline NWs. And the influence of TBs on the recoverable plasticity in twinned NWs is discussed.

## 5.2 Materials and Methods

### 5.2.1 Sample Synthesis and Characterization

Crystalline Ag NWs were synthesized by physical vapour deposition inside a molecular beam epitaxy system under ultra-high vacuum condition and substrate temperature of 700 °C. More details of the NW synthesis process are provided elsewhere [38].

Cross-sectional TEM samples of Ag NWs after deformation were prepared with focused ion beam (FIB). High-resolution TEM observations were performed on JEOL 2010F with a Schottky field emission gun (FEG) operated at 200 kV. Atomic resolution high-angle annular dark-field (HAADF) scanning transmission electron microscopy (STEM) imaging was performed on a probe corrected FEI Titan G<sup>2</sup> 60-300 kV S/TEM equipped with an X-FEG source operated at 200 kV.

### 5.2.2 *In Situ* TEM Mechanical Testing

The mechanical testing was carried out *in situ* inside a TEM using a MEMS based material testing system, which consists of an electrostatic (comb-drive) actuator, a capacitive load sensor and a gap in between for mounting samples (Figure 4.1a). Details on the load sensor calibration have been reported previously [228]. Displacement (and strain) is measured by digital image correlation of TEM images of two local markers on the specimen (Figure 4.1b). This MEMS based stage has a strain resolution of 0.01% (gage length 2 μm) and a stress resolution of 1.4 MPa (for example, for NW diameter of 104 nm).

NWs were mounted on the testing stage using a nanomanipulator (Klocke Nanotechnik, Germany) inside a FEI Nova 600 dual beam SEM. A Ag NW was welded to the nanomanipulator probe, then mounted to the MEMS stage and clamped by electron-beam-induced Pt deposition at the two free ends. Two local markers were deposited on the NWs for displacement (and strain) measurement. *In situ* TEM mechanical testing was performed on JEOL 2010F operated at 200 kV. The loading and unloading strain rates were  $\sim 0.005$  %/s. Low magnification images were recorded at a fixed condense (the second condense lens) current to minimize the focus change. The current density of incident e-beam is  $< 0.1$  A/cm<sup>2</sup> and its effect on the mechanical behavior of the NW under tensile testing can be neglected.

### 5.2.3 MD Simulations

Large-scale MD simulations were performed using the software package LAMMPS. Bi-twinned NW sample was generated according to experiments observed shapes. Figure 5.3 shows the atomic cross-section of the bi-twinned NW sample. The bi-twinned NW sample is about 15 nm in both height and width and 50 nm in length. The embedded atom method potential for Ag is used to describe the interatomic interactions. The vacancies are introduced by randomly removing atoms out of the samples. The samples are initially relaxed and equilibrated at temperature of 800 K for 600 ps using the Nosé–Hoover thermostat and barostat. Periodic boundary condition is imposed along the axial direction (that is, the loading direction  $\langle 110 \rangle$ ). Then the samples are stretched at a constant strain rate of  $10^8$  s<sup>-1</sup> under NVT ensemble (canonical ensemble) to a certain strain of 2.1% during loading process. Then the strain of the sample is fixed and NW is relaxed under NVT ensemble for 2 nanoseconds. In

the relaxation process, we monitor the variation of the axial stress by averaging the axial stresses over all atoms in the samples. Note that we have used an elevated temperature of 800 K in our MD simulations to accelerate the thermally activated processes of vacancy diffusion and the associated dislocation nucleation within the time scale of MD simulations. To examine the reversibility of deformation (related to the reverse motion of dislocations), we unload the elongated samples at a strain rate of  $-10^8 \text{ s}^{-1}$  until the axial stress in the simulated sample approaches zero. To identify defects during deformation of the samples, we paint atoms with different crystalline order in different colors using a common neighbor analysis. The green-colored atoms stand for atoms with face-centered cubic symmetry, the red ones those with hexagonal close-packed symmetry and the grey ones those at dislocation cores, surfaces and point defects.

## **5.3 Results**

### **5.3.1 Characterization of Bi-twinned NWs**

Crystalline Ag NWs were synthesized by physical vapour deposition inside a molecular beam epitaxy system. [38] A scanning electron microscope (SEM) image in Figure 5.1a shows Ag NWs on Si substrate, with length at micron scale (5-25  $\mu\text{m}$ ) and width at nanometer scale (50-200 nm). Size distribution of Ag NWs is shown in Figure 5.1b, taken into account of 113 NWs. Note that the size used here is referred to the NW width directly measured from TEM images. Based on TEM characterization, two types of  $\langle 110 \rangle$  oriented Ag NWs are dominated in the synthesized product, bi-twinned and single crystalline NWs. And bi-twinned Ag NWs

are dominant in the 113 examined NWs, with a percentage of 81% (Figure 5.1b). Figure 5.1c,d shows schematic drawings of the geometry of bi-twinned and single crystalline NWs, respectively. For bi-twinned NWs, a single internal TB is running parallel to the NW length direction.

In experiments, the type of Ag NWs can be directly determined from the cross-sectional TEM images when being viewed from  $\langle 110 \rangle$  zone axis, shown in the insets in Figure 1c,d. Both bi-twinned and single crystalline NWs show hexagonal cross-sectional shapes but with different arrangement of surface facets (marked in Figure 5.1c,d). And the bi-twinned NW show clear TB between the two twin variants (see the inset in Figure 5.1c). On the other hand, bi-twinned Ag NWs can be determined from longitudinal view under TEM observation. Based on the geometry of bi-twinned structure (see Figure 5.1c), there is a  $19.4^\circ$  tilt angle between  $\langle 1\bar{1}0 \rangle$  and  $\langle 001 \rangle_t$  zone axes from the two twin variants, respectively. It can be used as a criterion for determining bi-twinned NWs under longitudinal view since there is a  $45$  or  $90^\circ$  included angle between  $\langle 1\bar{1}0 \rangle$  and  $\langle 001 \rangle$  in single crystalline NWs. Moreover, the bi-twinned structure can also be distinguished by comparing the dark- and bright-field TEM images when being viewed from zone axes of  $\langle 1\bar{1}0 \rangle$  or  $\langle 001 \rangle$  from one of the twin variants. Figure 5.1e,f shows an example of a bi-twinned Ag NW being viewed from  $\langle 001 \rangle$  zone axis of one of the twin variants (see the diffraction pattern in the inset of Figure 5.1e). The on-zone grain showed bright image contrast under dark-field TEM imaging mode (Figure 5.1e), although the two twin variants displayed weak image contrast under bright-field imaging mode (Figure 5.1f).

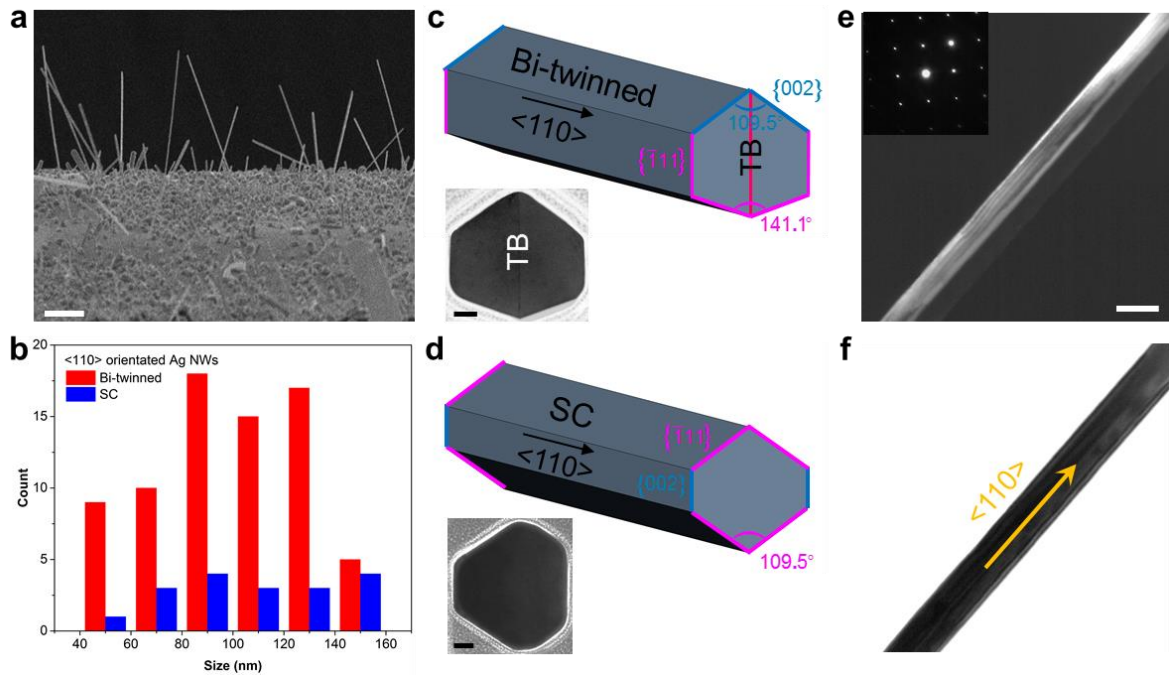


**Figure 5.1** Microstructure characterization of Ag NWs. (a) SEM image of Ag NWs on Si substrate. Scale bar, 5  $\mu\text{m}$ . (b) Size distribution of Ag NWs.  $\langle 110 \rangle$  oriented bi-twinned NWs are dominant in the examined 113 NWs. (c,d) Schematic drawings of bi-twinned and single crystalline Ag NWs and corresponding cross-sectional TEM images, respectively. Scale bar, 20 nm. (e,f) Dark- and bright-field TEM images of a bi-twinned Ag NW from longitudinal view. Inset in (e) is the corresponding SAED pattern taken from  $\langle 001 \rangle$  zone axis. Scale bar, 100 nm.

### 5.3.2 Stress Relaxation in Bi-twinned NWs

We performed *in situ* TEM tensile testing of individual NWs using a microelectromechanical system (MEMS) based testing stage (see Figure 4.1a) that allows

accurate measurement of both load and displacement [202, 220, 228]. Figure 5.2a shows the stress-strain responses during typical tensile tests (two cycles) of a bi-twinned Ag NW with loading direction along the NW length direction in three steps: loading, relaxation and unloading. Two initial stresses were chosen for stress relaxation (held about 15 minutes with a fixed applied force). One (0.84 GPa) is lower than the yield strength (1.23 GPa, see Figure 5.6a), while the other (1.21 GPa) is close to the yield strength. During the loading step, the NW in both cases exhibited nearly linear response. During the relaxation process, there is almost no change of stress and strain at the initial stress of 0.84 GPa, while obvious change of them observed at the initial stress of 1.21 GPa. The stress decreased with time, while the strain increased. On unloading, the strain in the NW completely recovered for both cases. For the stress relaxation process, Figure 5.2b shows the strain and stress as functions of time at the two selected stress levels. When the applied initial stress was 1.21 GPa, the NW strain increased monotonically with time from 1.66 to 1.79%, while the stress decreased monotonically from 1.21 to 1.12 GPa. However, if the applied initial stress (0.84 GPa) is much lower than the yield strength, there is no obvious change of strain and stress during the relaxation process. This is different from the phenomena observed in penta-twinned Ag NWs before [102] that stress relaxation can even take place at a very small initial stress (0.37 GPa) which is far below the yielding strength (1.0 GPa). Dislocation nucleation and retraction are suggested to contribute to the recoverable plasticity in twinned metallic NWs. [102] Therefore, a higher external stress is needed for the dislocation nucleation in bi-twinned NWs by compared with that in penta-twinned NWs. Detailed comparison of the mechanism in the two types of twinned NWs will be discussed later.

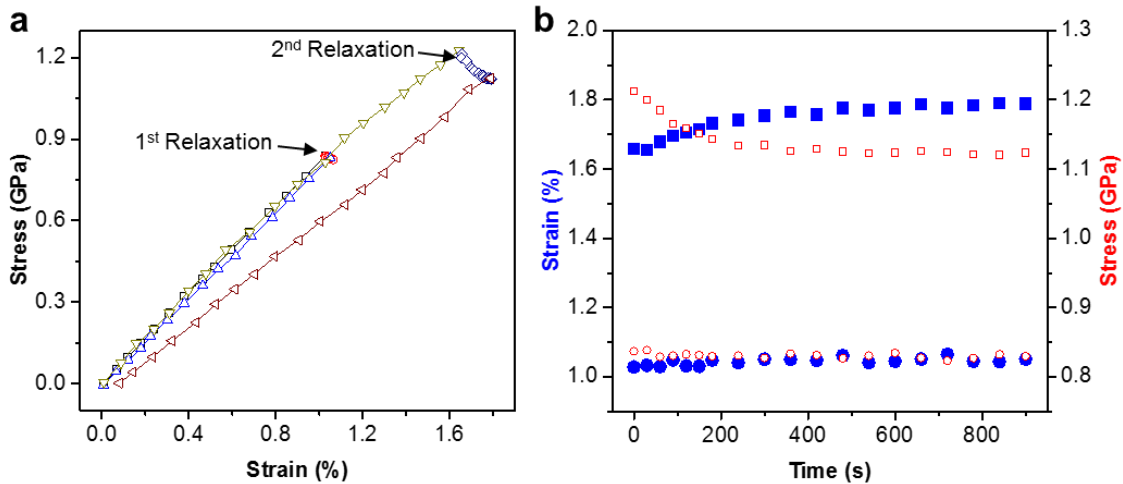


**Figure 5.2** *In situ* measurements of stress and strain evolutions in a bi-twinned Ag NW. (a) Stress-strain curve for the bi-twinned Ag NW under two cycles of loading-relaxation-unloading processes. The relaxation step took 15 minutes. (b) Relaxation curves for the bi-twinned Ag NW. Solid and open symbols correspond to the strain-time and stress-time relationships, respectively. Square and circle symbols correspond to high and low initial stress levels, respectively.

MD simulation was performed to reveal the underlying mechanisms behind the observed relaxation and recovery behavior of bi-twinned NWs. Hexagonal cross-sectional shape was taken into account for the modeling, shown in the inset of Figure 5.3a. To investigate the stress relaxation behavior, we first stretched the simulated sample to a strain of 2.1%, and then monitored stress relaxation while the applied strain was held fixed. The stress gradually decreased from an initial stress of 1.27 GPa by about 120 MPa. The partial dislocation

nucleated during the stress relaxation process, indicating that the stress relaxation is a direct consequence of dislocation nucleation in bi-twinned NWs. Similar to experiments, after stress relaxation the simulated samples were subsequently unloaded. When the applied stress came down to 30% of the initial one, the partial dislocation started to retract and the stress-strain curve was back to the original state. This phenomenon is very similar to the experimental observations. Figure 5.3b,c shows the snapshots of the deformed samples during relaxation and recovery. During stress relaxation, partial dislocation was found to nucleate near free surface and then expand through the grain interior but restricted by the TB (Figure 5.3b). During strain recovery, partial dislocation was retracted from the TB, resulting in complete strain recovery (Figure 5.3c). Details of such process are shown in Supporting Movie 1. It is known that there exists a repulsive force between TB and curved dislocation. [259] When the external stress is decreased during unloading process, the repulsive force from the TBs appears to induce reverse motion of dislocation by pushing the non-inserted segments as well as extracting the inserted segments from the TBs back towards where the dislocations were nucleated. Consequently, in bi-twinned NWs, stress relaxation originates from the nucleation of leading partial dislocations which are then held by the TB, while strain recovery is due to the reverse motion of partial dislocations driven by the repulsive force from the TB.

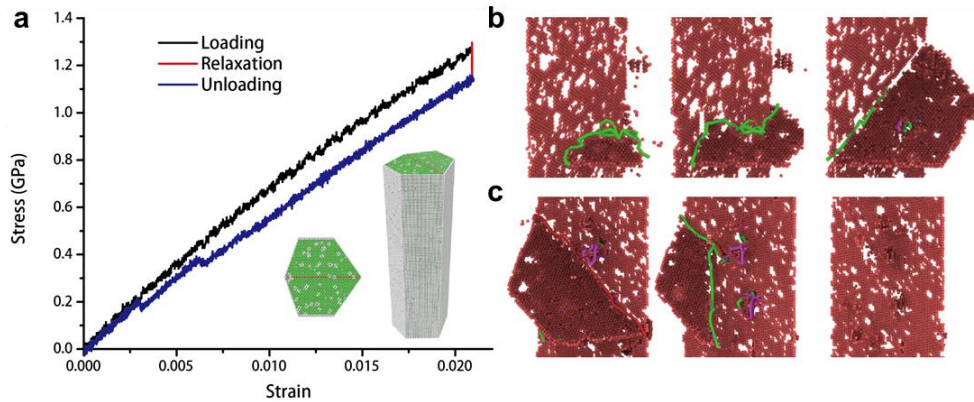


**Figure 5.3** MD simulation of stress relaxation and strain recovery in a bi-twinned Ag NW. (a) Stress-strain curve of the full loading-relaxation-unloading process. Inset in (a) is an atomic model viewed from transverse and longitudinal direction. (b) Snapshots of partial dislocation nucleation during loading process. (c) Snapshots of partial dislocation retraction during unloading process. Note that only red hexagonal closed packed atoms are shown here and solid lines are dislocation lines by DXA algorithm.

### 5.3.3 *In Situ* Observation of Dislocation Nucleation and Retraction

In order to track the dislocation motion in bi-twinned NWs, we did additional *in situ* TEM tensile tests and increased the applied stresses close to the ultimate stress (see Figure 5.6b). Figure 5.4 shows the stress-strain responses and the snapshots of microstructure evolution during typical loading-unloading cycles of a bi-twinned Ag NW with or without holding process. Before the tensile testing, the microstructure of the NW was checked and there was no exclusive defect in the NW excluding the internal TB (Figure 5.4b-i). Figure 5a, b shows a loading-unloading cycle without holding process (see Supporting Movie 2). As the

partial dislocation (marked by A in Figure 5.4b-ii) came out during the loading process, we directly decreased the applied force and turned the NW into unloading process. It is clear that another partial dislocation (marked by B in Figure 5.4b-iii) appeared at the initial stage of the unloading process which was probable due to the overstress of the NW during the loading process. As the applied stress continued decreasing, the later generated dislocation B first disappeared (Figure 5b-iv) when the applied stress was decreased by 75%. And dislocation A also disappeared as the applied stress was fully retracted. The plastic strain was almost recovered on unloading. As described before, release of internal concentrated stress at the TB is suggested to provide the driving force to repulse the leading partials and make them disappeared during the unloading process. On the other hand, Figure 5.4c,d displays a loading-holding-unloading cycle with a short-time (5 minutes) stress relaxation by fixing the applied load (see Supporting Movie 3). Two partial dislocations (marked by C and D in Figure 5.4d-ii) came out as the applied stress was close to the ultimate stress. During the holding process, a new one (marked by E in Figure 5.4d-iii) was generated and an obvious planar sliding was observed. The planar sliding was due to the propagation of dislocation C across the entire cross-section. During the unloading process, dislocation D first disappeared as the applied stress was decreased by 80% (Figure 5.4d-iv). And the other two dislocations (C and E) disappeared at the last step (Figure 5.4d-v). Note that there is residual strain ( $\sim 0.2\%$ ) left in the NW due to the permanent planar sliding which cannot be fully recovered after holding 15 minutes at zero applied force. Accordingly, the above results indicate that the internal TB in bi-twinned NWs can act as an obstacle for hindering the propagation of partial dislocation across the TB in a short time when the applied stress is lower than the ultimate strength.

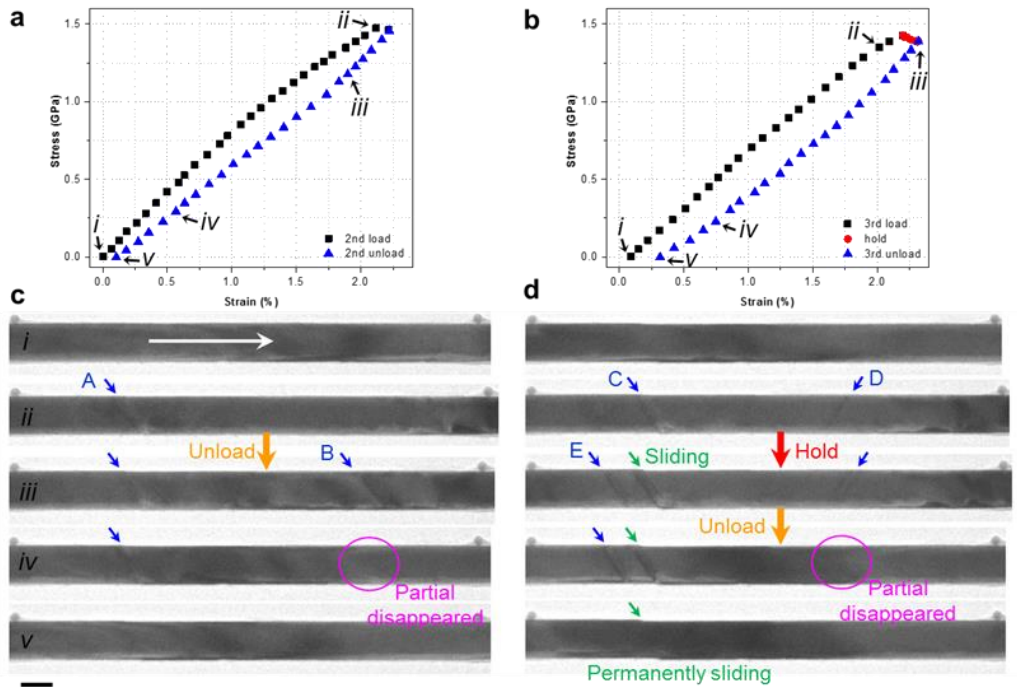


**Figure 5.4** Mechanical response and microstructure evolution of a bi-twinned Ag NW under *in situ* TEM tensile testing. (a) Stress-strain curve for the bi-twinned Ag NW without a holding process. (b) Microstructure evolution during the load-unload process. (c) Stress-strain curved for the bi-twinned Ag NW with a holding process. The relaxation step took 5 minutes. (d) Microstructure evolution during the load-hold-unload process. The location of partial dislocations and planar sliding in the NW are marked by blue and green arrows, respectively. Scale bar, 100 nm.

For a comparison, Figure 5.5 shows the stress-strain response and the snapshots of microstructure evolution during a typical tensile test of a single crystalline Ag NW (see Supporting Movie 4). The loading direction was along the NW length direction and there was

no extended defect in the NW (Figure 5.5b-i). As the applied stress reached to the yield strength (1.0 GPa), a planar sliding quickly took place in the NW and the strain was obviously increased (Figure 5.5b-ii). During the unloading process, a small deformed segment was always kept in the NW (Figure 5.5b-iii and iv) and the NW showed almost elastic response as the load was releasing. It indicates that the planar sliding during the loading process was a permanent plastic deformation which cannot be recovered anymore. Further studies revealed that twinning deformation took place in the single crystalline NW which caused such permanent plastic deformation.

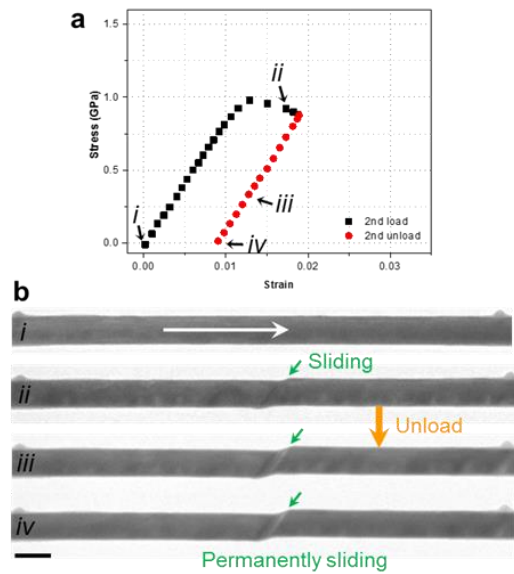


**Figure 5.5** Mechanical response and microstructure evolution of a single crystalline Ag NW under *in situ* TEM tensile testing. (a) Stress-strain curve for the single crystalline Ag NW. (b) Microstructure evolution during the load-unload process. Permanent planar sliding in the NW is marked by the green arrows. Scale bar, 100 nm.

As a summary, the observed recoverable plasticity in bi-twinned NWs is attributed to the nucleation and retraction of partial dislocations. Nucleation of partial dislocations from the free surface mainly contributed to the stress relaxation on loading and retraction of partial dislocations to the plastic strain recovery on unloading. The internal TB in bi-twinned NWs can act as an obstacle for hindering the propagation of partial dislocations across the TB, leading to the recoverable plasticity. Whereas, if partial dislocations directly travel through the entire cross-section in bi-twinned or single crystalline NWs, it will result in permanent plastic deformation.

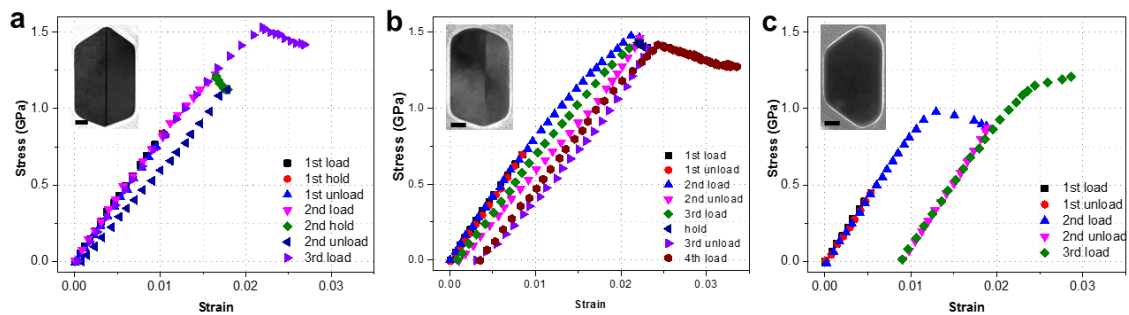


**Figure 5.6** Stress-strain curves for the tested NWs in Figure 5.2, 4.4 and 4.5, respectively. (a,b) from bi-twinned NWs. (c) from single crystalline Ag NW. Insets in (a-c) show the cross-sectional TEM images of the tested NWs. All scale bars, 20 nm.

## 5.4 Discussions

The internal TBs in twinned NWs play an important role for the observed recoverable plasticity owing to the nucleation and retraction of partial dislocations since there is no such behavior in single crystalline NWs. It should be mentioned that recoverable plasticity in

twinned NWs with inclined or perpendicular TBs to the NW length direction could be neglected because such TBs can effectively act as obstacles for the nucleation of dislocations [155]. And dislocations nucleated from the free surface in them are prone to travel through the entire cross-section leading to permanent plastic deformation, similar to the case in single crystalline NWs. Furthermore, regular GBs (such as low-angle/high-angle tilt GB) in bi-crystalline NWs was predicted to fail to block or trap the dislocations, resulting in no strain recovery. [102]

Although recoverable plasticity is observed in both bi- and penta-twinned NWs with TBs parallel to the NW length direction, there exists significant difference between them, including the stress relaxation, strain recovery and the interaction between dislocation and TBs. As described in the previous study, [102] the penta-twinned NWs have five twin variants which are arranged homogeneously and intersected at the center from the cross-sectional view, showing a symmetrical configuration. And there are pre-existed defects (partials and SFs) distributed along one or two of the TBs due to the angle compensation to a pentagonal shape (Figure 5.7b). Whereas, the bi-twinned NWs only have single TB parallel to the NW length direction with a perfect atomic arrangement along the TB (Figure 5.7a). The difference in their microstructures are considered to be the dominant factor to cause the significant difference in the observed recoverable plasticity in the two types of twinned NWs.

First, stress relaxation in bi-twinned NWs requires a higher applied stress level than that in penta-twinned NWs. It has been proposed that stress relaxation in penta-twinned NWs is significantly affected by vacancies which can promote the nucleation of partial dislocations. [102] The pre-existed liner or planar defects in penta-twinned NWs could also assist the

nucleation and propagation of partial dislocations so that the stress relaxation can even occur at a very low stress level (Figure 5.8). However, bi-twinned NWs have no exclusive linear or planar defects in the twin variants. Partial dislocations only nucleate from the free surface, and expand into the grain interior. Thus a higher stress level is required for the nucleation of partial dislocations in bi-twinned NWs. On the other hand, the amplitude of stress relaxation in bi-twinned NWs is only about half of that in penta-twinned NWs (see Figure 5.2b and Figure 5.8b). It indicates that penta-twinned NWs have higher capability for dislocation nucleation, which could also be attributed to the high density of pre-existed defects in them.

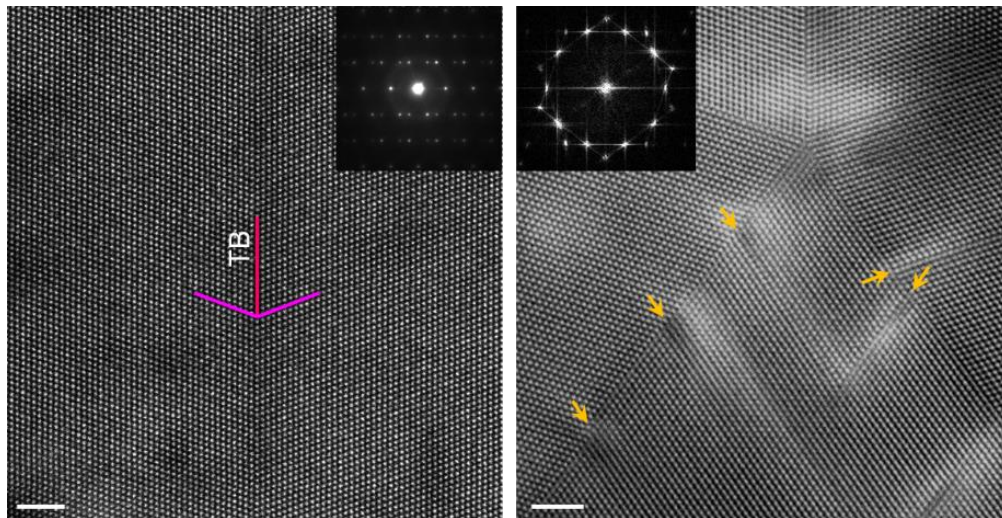


**Figure 5.7** High resolution STEM images shows the atomic alignments from the cross-sectional view of bi and penta-twinned Ag NWs. (a) a bi-twinned Ag NW; (b) a penta-twinned NW. Internal defects (SFs and partials) distributed along the TBs in the penta-twinned Ag NW are marked by the arrows. The insets in (a,b) are the corresponding SAED patterns. All scale bar, 2 nm.

Second, plastic strain recovery in bi-twinned NWs is almost finished during the unloading process, while an additional strain recovery process is needed for penta-twinned NWs. Penta-twinned NWs showed almost linear strain-stress change during the unloading process but a full strain recovery during the additional recovery process. [102] It is suggested that reversible dislocation motion and vacancy diffusion are promoted by the inhomogeneous strain field generated by the fivefold twin during the additional strain recovery process. However, there is no obvious residual strain caused by the single TB in bi-twinned NWs.

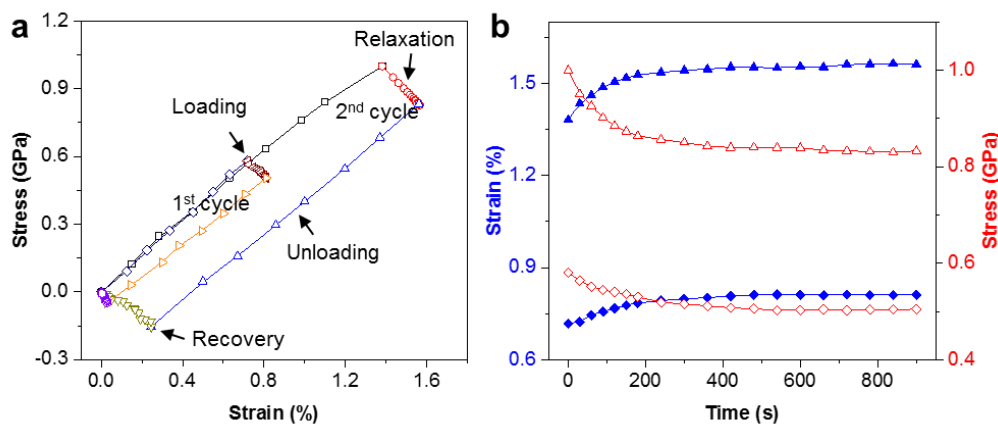


**Figure 5.8** *In situ* measurements of stress and strain evolutions in a penta-twinned Ag NW (120 nm in diameter). (a) Stress-strain curve for the NW under two cycles of loading-relaxation-unloading-recovery process. The relaxation and recovery steps took 15 minutes. (b) Relaxation curves for the NW at different stress level. Solid and open symbols correspond to the strain-time and stress-time relationships, respectively. Diamond and triangle symbols correspond to low and high initial stress levels, respectively.

Third, interaction between partial dislocations and TBs results in different partially reversible plasticity in bi- and penta-twinned NWs. If complex dislocation structure existed in the penta-twinned NWs caused by interaction of stacking fault decahedrons, plasticity became only partially reversible. [182] And a strong Bauschinger's effect was observed in penta-twinned NWs during cyclic loading. Different from the case in penta-twinned NWs, the propagation of leading partials in bi-twinned NWs nucleated from the free surface was directly hindered by the single TB under an applied stress which was lower than the ultimate strength. If increase of the applied stress and the holding time, the leading partial will travel through the TB to the other twin variant followed by a trailing partial sweeping across the entire cross-section, and a permanent plastic deformation (planar sliding) will be left in the NWs. Additionally, from the cyclic loading of bi-twinned NWs (see Figure 5.6b), plastic flow upon unloading was clearly observed, which was reminiscent of the classical Bauschinger's effect.

## 5.5 Conclusions

In summary, recoverable plasticity was revealed in bi-twinned Ag NWs via *in situ* TEM tensile testing, microstructure characterization and MD simulations. *In situ* tensile experiments show that bi-twinned Ag NWs undergo stress relaxation on loading at a stress level close to the yield strength and plastic strain recovery on unloading. Our experimental and simulated results confirmed that stress relaxation originates from the nucleation of leading partial dislocations from the free surface, while strain recovery is due to the reverse motion of partial dislocations driven by the repulsive force from the TB. The internal TB in bi-twinned NWs

can be acted as an obstacle for hindering the propagation of partial dislocations across the TB at an applied stress lower than the ultimate strength. If the partial dislocations cross through the entire cross-section, a permanent planar sliding will be left.

Significant difference was found in the observed recoverable plasticity in bi- and penta-twinned [102] Ag NWs, including the stress relaxation, the strain recovery and the interaction between dislocations and TBs, which is attributed to the large difference in their microstructure configurations.

The observed recoverable plasticity in bi-twinned NWs shows new insight on the understanding of interactions between dislocations and TBs in twinned metallic nanomaterials.

## CHAPTER 6

### CONCLUSIONS AND FUTURE WORKS

#### 6.1 Conclusions

In this thesis, we focus on the mechanical behaviors of three types of NWs, SiC, ZnO and Ag NWs. We emphasize on the nanomechanics revealed by combining *in situ* SEM/TEM mechanical testing and theoretical modeling, including fracture mechanism of SiC NWs, anelasticity of ZnO NWs, deformation mechanisms of Ag NWs and recoverable plasticity in twinned Ag NWs.

In Chapter 2, we have quantitatively studied the mechanical properties of SiC NWs. The microstructure of SiC NWs is rather complex, consisting of pure 3C structure, 3C structure with an inclined stacking fault, and highly defective structure in a periodic fashion along the NW length. We found that the SiC NWs fail in brittle fracture at room temperature, in contrast to the superplasticity as previously observed. The SiC NWs exhibited strong size effect in the fracture strength; that is, the fracture strength increased with decreasing diameter, up to over 25 GPa and approaching the theoretical strength of 3C SiC. It is interesting to observe that the cracks initiate and propagate in the 3C segments with the  $19.47^\circ$  SFs, rather than in the highly defective segments. The size effect on fracture strength of SiC NWs is attributed to the size-dependent defect density (i.e., of the 3C structure with  $19.47^\circ$  SFs), rather than the surface effect that is common for single crystalline NWs.

In Chapter 3, we have reported large anelastic behaviour in single crystalline NWs governed by stress-gradient-induced migration of point defects. The observed anelasticity was

attributed to a type of nonlinear Gorsky relaxation that involves the diffusion of two types of point defects under an inhomogeneous stress field. The large anelasticity in ZnO NWs resulted in high mechanical damping with the merit index of 1.13. Similar anelastic behaviour was found in p-doped Si NWs. The large magnitude of the anelasticity is attributed to the high strain applied to the NWs, while the small diffusion distance, enormous stress gradient and large diffusivity result in the short relaxation (recovery) time scale. The large diffusivity in NWs is due to the surface-mediated bulk diffusion and reduced activation energy under ultrahigh stress. The present study also suggests a useful experimental approach to study transport and equilibrium properties of point defects at the nanoscale. Since point defects have been reported to exist in many nanostructures [238], the reported anelasticity is expected to have broad impacts in nanotechnology. With the rapid progress in large-scale synthesis of NWs [239], our study suggests that crystalline NWs with point defects could serve as highly efficient damping materials for a broad range of applications in aerospace, automotive, energy and biomedical industries.

In Chapter 4, we have discovered a transition between two deformation modes, dislocation slip and detwinning-twinning, in bi-twinned metallic NWs. Localized dislocation nucleation and propagation across the TB lead to permanent planar sliding and limited fracture strain in bi-twinned NWs with balanced volume ratio, while detwinning-twinning deformation results in superplasticity in those with small volume ratios. The superplasticity observed in bi-twinned metallic NWs is somewhat similar to that in single crystalline metallic NWs due to coherent twinning propagation. Our experimental and theoretical results indicated that the detwinning process is governed by interaction of multiple localized dislocations with the TB

A criterion for the detwinning deformation was proposed based on the detwinning energy barrier, which was shown capable of capturing the effects of the volume ratio and cross-sectional aspect ratio on the transition of the deformation modes in bi-twinned NWs. Among the single crystalline, bi- and penta-twinned Ag NWs, bi-twinned Ag NWs offer the best combined mechanical properties.

In Chapter 5, we have revealed recoverable plasticity in bi-twinned Ag NWs. *In situ* tensile experiments showed that bi-twinned Ag NWs undergo stress relaxation on loading and plastic strain recovery on unloading. Our experimental and simulated results confirmed that stress relaxation originates from the nucleation of leading partials from the free surface, while strain recovery is due to the reverse motion of partials driven by the repulsive force from the TB. The internal TB in bi-twinned NWs can be acted as an obstacle for hindering dislocation propagation across the TB at an applied stress level lower than the ultimate strength. If the dislocations cross through the TB, a permanent planar sliding will be left. On the other hand, significant difference was found in the observed recoverable plasticity in bi- and penta-twinned [102] Ag NWs, including the stress relaxation, strain recovery and the interaction between dislocations and TBs. It is attributed to the large difference in their microstructure configurations.

## 6.2 Future Works

With the development of advanced nanomechanical testing systems, it allows us to investigate 1D nanomaterials involving not just stress field but also multi-physical effects. With the advance of nanodevices, 1D nanostructures including NWs as building blocks will undergo more and more realistic mechanical loadings. Therefore, it is of great relevance to investigate other effects on their mechanical behaviors, such as temperature, time and environment [260] which will be very important for long-time operation and reliability of the nanodevices. Undoubtedly, MEMS will play important roles in such studies.

Temperature effects on the mechanical properties of 1D nanostructures are interesting, but so far have been much less studied at least experimentally. Our temperature controllable MEMS based device is allowed to be heated up to 600 K [220], which greatly enhance the instrumentation capabilities for probing the thermomechanical properties at nanoscale. For the study of brittle to ductile transition (BDT) in Si NWs, it could be tested to find out the critical size and temperature of a Si NW that shows BDT. On the other hand, we keep interests on the investigation of thermal effects on dislocation nucleation and propagation, and eventually on the mechanical behaviors of metallic NWs. Our onsite heating MEMS based device allows us to study the microstructure evolution via *in situ* TEM tensile testing at high temperature.

One of the most common causes of structural failure in materials is fatigue induced by cyclic loading. [261, 262] A common result of these studies is that nanostructured materials show an increased fatigue life, especially in the high-cycle regime. This can be related to their increased yield strength, which is typically accompanied by a reduced ductility. However, there is a little study on the fatigue behaviors of 1D nanomaterials no matter how it is important for

the reliability of the nanodevices. Thus, it is of great importance to investigate the fatigue behaviors of 1D nanomaterials via a MEMS based device with capability of high frequency cycling mechanical loading performed *in situ* inside a SEM or TEM.

The characterization of nanomaterials under high strain rate is critical to understand their suitability for dynamic applications such as nanoresonators and nanoswitches. [263] It is also of great theoretical importance to explore nanomechanics with dynamic and rate effects. Our MEMS based device allows a change of strain ranging from  $2 \times 10^{-4}/s$  to  $2/s$ . It enables the investigation of the effect of high strain rate on the mechanical behavior of 1D nanostructures, such as dislocation nucleation as the rate controlling mechanism and possible brittle-to-ductile failure mode transition. *In situ* TEM tensile testing also allows the investigation of microstructure evolution along the NW, such as dislocation density and spatial distribution of plastic regions with the increase of strain rate.

Electromechanical coupling is a topic of current interest in nanostructures, such as metallic and semiconducting NWs, for a variety of electronic and energy applications. [264, 265] However, the mechanical signature of electromigration and the electrical nature of dislocation activity remain to be studied. And electromigration is a likely failure mode in nano-sized interconnects as a result of higher current densities. [243] Hence, the determination of structure-property relations that dictate the electromechanical coupling requires the development of experimental tools to perform accurate metrology. Our novel MEMS based devices allow integrated four-point, uniaxial, electromechanical measurements of freestanding 1D nanostructures via *in situ* SEM or TEM testing. We are interested in the effect of stress

induced defects on the resistance of metallic NWs and tunable band gap of semiconductor NWs.

In our recent studies, we have demonstrated large anelastic behaviors in semiconductor NWs (ZnO and Si) and metallic NWs. [4] And we have elucidated the anelasticity of ZnO NWs governed by stress-gradient-induced migration of point defects. However, the mechanisms of anelasticity in metallic NWs remain an open question. We would like to deeply investigate the anelastic behavior in metallic NWs and reveal how the surface-mediated diffusion works in them. And we are interested in the dislocation coupled anelastic behavior in metallic NWs via *in situ* TEM bending testing. Meanwhile, we will keep our interests in investigating the effects of internal structures on the mechanical behaviors of NWs under different loading modes.

## REFERENCES

- [1] Hoffmann S, Utke I, Moser B, Michler J, Christiansen SH, Schmidt V, Senz S, Werner P, Gösele U, Ballif C. Measurement of the bending strength of vapor-liquid-solid grown silicon nanowires. *Nano letters* 2006, **6**(4): 622-625.
- [2] Zhu Y, Xu F, Qin Q, Fung WY, Lu W. Mechanical Properties of Vapor-Liquid-Solid Synthesized Silicon Nanowires. *Nano Letters* 2009, **9**(11): 3934-3939.
- [3] Chen LY, He M-r, Shin J, Richter G, Gianola DS. Measuring surface dislocation nucleation in defect-scarce nanostructures. *Nature materials* 2015, **14**(7): 707-713.
- [4] Cheng G, Miao C, Qin Q, Li J, Xu F, Haftbaradaran H, Dickey EC, Gao H, Zhu Y. Large anelasticity and associated energy dissipation in single-crystalline nanowires. *Nature nanotechnology* 2015, **10**(8): 687-691.
- [5] Chan CK, Peng H, Liu G, McIlwrath K, Zhang XF, Huggins RA, Cui Y. High-performance lithium battery anodes using silicon nanowires. *Nature Nanotechnology* 2008, **3**(1): 31-35.
- [6] Law M, Greene LE, Johnson JC, Saykally R, Yang P. Nanowire dye-sensitized solar cells. *Nature materials* 2005, **4**(6): 455-459.
- [7] Lu W, Lieber CM. Nanoelectronics from the bottom up. *Nature Materials* 2007, **6**(11): 841-850.
- [8] Wang ZL, Song J. Piezoelectric nanogenerators based on zinc oxide nanowire arrays. *Science* 2006, **312**(5771): 242-246.

- [9] Barth S, Hernandez-Ramirez F, Holmes JD, Romano-Rodriguez A. Synthesis and applications of one-dimensional semiconductors. *Progress in Materials Science* 2010, **55**(6): 563-627.
- [10] Xiang J, Lu W, Hu Y, Wu Y, Yan H, Lieber CM. Ge/Si nanowire heterostructures as high-performance field-effect transistors. *Nature* 2006, **441**(7092): 489-493.
- [11] Lieber CM, Wang ZL. Functional nanowires. *MRS bulletin* 2007, **32**(02): 99-108.
- [12] Xia YN, Yang PD, Sun YG, Wu YY, Mayers B, Gates B, Yin YD, Kim F, Yan YQ. One-dimensional nanostructures: Synthesis, characterization, and applications. *Advanced Materials* 2003, **15**(5): 353-389.
- [13] Holmes JD, Johnston KP, Doty RC, Korgel BA. Control of thickness and orientation of solution-grown silicon nanowires. *Science* 2000, **287**(5457): 1471-1473.
- [14] Xu F, Lu W, Zhu Y. Controlled 3D Buckling of Silicon Nanowires for Stretchable Electronics. *Acs Nano* 2011, **5**(1): 672-678.
- [15] McAlpine MC, Friedman RS, Jin S, Lin KH, Wang WU, Lieber CM. High-performance nanowire electronics and photonics on glass and plastic substrates. *Nano Letters* 2003, **3**(11): 1531-1535.
- [16] Cui Z, Pobleto FR, Cheng G, Yao S, Jiang X, Zhu Y. Design and operation of silver nanowire based flexible and stretchable touch sensors. *Journal of Materials Research* 2015, **30**(01): 1-7.
- [17] Mårtensson T, Svensson CPT, Wacaser BA, Larsson MW, Seifert W, Deppert K, Gustafsson A, Wallenberg LR, Samuelson L. Epitaxial III-V nanowires on silicon. *Nano Letters* 2004, **4**(10): 1987-1990.

- [18] Takei K, Takahashi T, Ho JC, Ko H, Gillies AG, Leu PW, Fearing RS, Javey A. Nanowire active-matrix circuitry for low-voltage macroscale artificial skin. *Nature Materials* 2010, **9**(10): 821-826.
- [19] McAlpine MC, Ahmad H, Wang D, Heath JR. Highly ordered nanowire arrays on plastic substrates for ultrasensitive flexible chemical sensors. *Nature materials* 2007, **6**(5): 379-384.
- [20] Feng XL, He R, Yang P, Roukes ML. Very high frequency silicon nanowire electromechanical resonators. *Nano Letters* 2007, **7**(7): 1953-1959.
- [21] Lu W, Lieber CM. Semiconductor nanowires. *Journal of Physics D: Applied Physics* 2006, **39**(21): R387.
- [22] Xu F, Zhu Y. Highly conductive and stretchable silver nanowire conductors. *Advanced materials* 2012, **24**(37): 5117-5122.
- [23] Yao S, Zhu Y. Nanomaterial-enabled stretchable conductors: strategies, materials and devices. *Advanced Materials* 2015, **27**(9): 1480-1511.
- [24] Song L, Myers AC, Adams JJ, Zhu Y. Stretchable and reversibly deformable radio frequency antennas based on silver nanowires. *ACS applied materials & interfaces* 2014, **6**(6): 4248-4253.
- [25] Wang ZL. ZnO nanowire and nanobelt platform for nanotechnology. *Materials Science and Engineering: R: Reports* 2009, **64**(3-4): 33-71.
- [26] Hochbaum AI, Chen R, Delgado RD, Liang W, Garnett EC, Najarian M, Majumdar A, Yang P. Enhanced thermoelectric performance of rough silicon nanowires. *Nature* 2008, **451**(7175): 163-167.

- [27] Li D, Wu Y, Kim P, Shi L, Yang P, Majumdar A. Thermal conductivity of individual silicon nanowires. *Applied Physics Letters* 2003, **83**(14): 2934-2936.
- [28] Tian B, Zheng X, Kempa TJ, Fang Y, Yu N, Yu G, Huang J, Lieber CM. Coaxial silicon nanowires as solar cells and nanoelectronic power sources. *Nature* 2007, **449**(7164): 885-889.
- [29] Park HS, Cai W, Espinosa HD, Huang H. Mechanics of Crystalline Nanowires. *Mrs Bulletin* 2009, **34**(3): 178-183.
- [30] Agrawal R, Peng B, Gdoutos EE, Espinosa HD. Elasticity size effects in ZnO nanowires– a combined experimental-computational approach. *Nano Letters* 2008, **8**(11): 3668-3674.
- [31] Pirota KR, Silva EL, Zanchet D, Navas D, Vázquez M, Hernández-Vélez M, Knobel M. Size effect and surface tension measurements in Ni and Co nanowires. *Physical Review B* 2007, **76**(23): 233410.
- [32] Chen C, Shi Y, Zhang Y, Zhu J, Yan Y. Size dependence of Young's modulus in ZnO nanowires. *Physical review letters* 2006, **96**(7): 075505.
- [33] Agrawal R, Peng B, Espinosa HD. Experimental-Computational Investigation of ZnO nanowires Strength and Fracture. *Nano Letters* 2009, **9**(12): 4177-4183.
- [34] Wang N, Cai Y, Zhang R. Growth of nanowires. *Materials Science and Engineering: R: Reports* 2008, **60**(1): 1-51.
- [35] Law M, Goldberger J, Yang P. SEMICONDUCTOR NANOWIRES AND NANOTUBES. *Annual Review of Materials Research* 2004, **34**(1): 83-122.

- [36] Yang P, Yan R, Fardy M. Semiconductor Nanowire: What's Next? *Nano Letters* 2010, **10**(5): 1529-1536.
- [37] Heo YW, Norton DP, Tien LC, Kwon Y, Kang BS, Ren F, Pearton SJ, LaRoche JR. ZnO nanowire growth and devices. *Materials Science and Engineering: R: Reports* 2004, **47**(1-2): 1-47.
- [38] Richter G, Hillerich K, Gianola DS, Moenig R, Kraft O, Volkert CA. Ultrahigh Strength Single Crystalline Nanowhiskers Grown by Physical Vapor Deposition. *Nano Letters* 2009, **9**(8): 3048-3052.
- [39] Huang Z, Geyer N, Werner P, de Boor J, Gösele U. Metal-Assisted Chemical Etching of Silicon: A Review. *Advanced Materials* 2011, **23**(2): 285-308.
- [40] Wu R, Zhou K, Yue CY, Wei J, Pan Y. Recent progress in synthesis, properties and potential applications of SiC nanomaterials. *Progress in Materials Science* 2015, **72**: 1-60.
- [41] Lee KN, Jung SW, Shin KS, Kim WH, Lee MH, Seong WK. Fabrication of suspended silicon nanowire arrays. *Small* 2008, **4**(5): 642-648.
- [42] Peng K, Fang H, Hu J, Wu Y, Zhu J, Yan Y, Lee S. Metal-Particle-Induced, Highly Localized Site-Specific Etching of Si and Formation of Single-Crystalline Si Nanowires in Aqueous Fluoride Solution. *Chemistry—A European Journal* 2006, **12**(30): 7942-7947.
- [43] Schmidt V, Senz S, Gösele U. Diameter-dependent growth direction of epitaxial silicon nanowires. *Nano letters* 2005, **5**(5): 931-935.

- [44] Morales AM, Lieber CM. A laser ablation method for the synthesis of crystalline semiconductor nanowires. *Science* 1998, **279**(5348): 208-211.
- [45] Duan X, Lieber CM. General synthesis of compound semiconductor nanowires. *Advanced Materials* 2000, **12**(4): 298-302.
- [46] Wood EL, Sansoz F. Growth and properties of coherent twinning superlattice nanowires. *Nanoscale* 2012, **4**(17): 5268-5276.
- [47] Gu XW, Loynachan CN, Wu Z, Zhang Y-W, Srolovitz DJ, Greer JR. Size-dependent deformation of nanocrystalline Pt nanopillars. *Nano letters* 2012, **12**(12): 6385-6392.
- [48] Carim AH, Lew KK, Redwing J. Bicrystalline silicon nanowires. *Advanced Materials* 2001, **13**(19): 1489-1491.
- [49] Choi H-J, Seong H-K, Lee J-C, Sung Y-M. Growth and modulation of silicon carbide nanowires. *Journal of Crystal Growth* 2004, **269**(2-4): 472-478.
- [50] Zhang H-F, Wang C-M, Wang L-S. Helical crystalline SiC/SiO<sub>2</sub> core-shell nanowires. *Nano letters* 2002, **2**(9): 941-944.
- [51] Wu Y, Cui Y, Huynh L, Barrelet CJ, Bell DC, Lieber CM. Controlled growth and structures of molecular-scale silicon nanowires. *Nano Letters* 2004, **4**(3): 433-436.
- [52] Hannon JB, Kodambaka S, Ross FM, Tromp RM. The influence of the surface migration of gold on the growth of silicon nanowires. *Nature* 2006, **440**(7080): 69-71.
- [53] Wang Y, Schmidt V, Senz S, Gösele U. Epitaxial growth of silicon nanowires using an aluminium catalyst. *Nature nanotechnology* 2006, **1**(3): 186-189.

- [54] Wagner R, Ellis W. Vapor-liquid-solid mechanism of single crystal growth. *Applied Physics Letters* 1964, **4**(5): 89-90.
- [55] Sun Y, Gates B, Mayers B, Xia Y. Crystalline Silver Nanowires by Soft Solution Processing. *Nano Letters* 2002, **2**(2): 165-168.
- [56] Sun Y, Mayers B, Herricks T, Xia Y. Polyol Synthesis of Uniform Silver Nanowires: A Plausible Growth Mechanism and the Supporting Evidence. *Nano Letters* 2003, **3**(7): 955-960.
- [57] Venables J. *Introduction to surface and thin film processes*. Cambridge University Press, 2000.
- [58] Wang ZL. Transmission electron microscopy of shape-controlled nanocrystals and their assemblies. *The Journal of Physical Chemistry B* 2000, **104**(6): 1153-1175.
- [59] Wang P-I, Zhao Y, Wang G, Lu T. Novel growth mechanism of single crystalline Cu nanorods by electron beam irradiation. *Nanotechnology* 2003, **15**(1): 218.
- [60] Egelhoff Jr WF, Tibbetts GG. Growth of copper, nickel, and palladium films on graphite and amorphous carbon. *Physical Review B* 1979, **19**(10): 5028.
- [61] Hamilton J, Logel P. Nucleation and growth of Ag and Pd on amorphous carbon by vapor deposition. *Thin Solid Films* 1973, **16**(1): 49-63.
- [62] Mortimer D, Nicholas M. The wetting of carbon by copper and copper alloys. *Journal of Materials Science* 1970, **5**(2): 149-155.
- [63] Szlufarska I, Chandross M, Carpick RW. Recent advances in single-asperity nanotribology. *Journal of Physics D: Applied Physics* 2008, **41**(12): 123001.

- [64] Persson C, Lindefelt U. Detailed band structure for 3C-, 2H-, 4H-, 6H-SiC, and Si around the fundamental band gap. *Physical Review B* 1996, **54**(15): 10257-10260.
- [65] Morkoc H, Strite S, Gao GB, Lin ME, Sverdlov B, Burns M. LARGE-BAND-GAP SIC, III-V NITRIDE, AND II-VI ZNSE-BASED SEMICONDUCTOR-DEVICE TECHNOLOGIES. *Journal of Applied Physics* 1994, **76**(3): 1363-1398.
- [66] Huang HC, Ghoniem N. NEUTRON DISPLACEMENT DAMAGE CROSS-SECTIONS FOR SIC. *Journal of Nuclear Materials* 1993, **199**(3): 221-230.
- [67] Bhaskaran H, Gotsmann B, Sebastian A, Drechsler U, Lantz MA, Despont M, Jaroenapibal P, Carpick RW, Chen Y, Sridharan K. Ultralow nanoscale wear through atom-by-atom attrition in silicon-containing diamond-like carbon. *Nature nanotechnology* 2010, **5**(3): 181-185.
- [68] Li X, Bhushan B. Fatigue studies of nanoscale structures for MEMS/NEMS applications using nanoindentation techniques. *Surface and Coatings Technology* 2003, **163**: 521-526.
- [69] Ouyang M, Yuan C, Muisener R, Boulares A, Koberstein J. Conversion of some siloxane polymers to silicon oxide by UV/ozone photochemical processes. *Chemistry of materials* 2000, **12**(6): 1591-1596.
- [70] Li Q, Kim K-S. Micromechanics of friction: effects of nanometre-scale roughness. *Proceedings of the Royal Society of London A: Mathematical, Physical and Engineering Sciences*; 2008: The Royal Society; 2008. p. 1319-1343.
- [71] Bai X, Gao P, Wang ZL, Wang E. Dual-mode mechanical resonance of individual ZnO nanobelts. *Applied Physics Letters* 2003, **82**(26): 4806-4808.

- [72] Zekentes K, Rogdakis K. SiC nanowires: material and devices. *Journal of Physics D-Applied Physics* 2011, **44**(13): 133001.
- [73] Yang W, Araki H, Tang CC, Thaveethavorn S, Kohyama A, Suzuki H, Noda T. Single-crystal SiC nanowires with a thin carbon coating for stronger and tougher ceramic composites. *Advanced Materials* 2005, **17**(12): 1519-1523.
- [74] Yang YT, Ekinici KL, Huang XMH, Schiavone LM, Roukes ML, Zorman CA, Mehregany M. Monocrystalline silicon carbide nanoelectromechanical systems. *Applied Physics Letters* 2001, **78**(2): 162-164.
- [75] Shim HW, Huang H. Three-stage transition during silicon carbide nanowire growth. *Applied Physics Letters* 2007, **90**(8): 083106.
- [76] Wang ZL. Zinc oxide nanostructures: growth, properties and applications. *Journal of Physics: Condensed Matter* 2004, **16**(25): R829.
- [77] Fan F-R, Ding Y, Liu D-Y, Tian Z-Q, Wang ZL. Facet-selective epitaxial growth of heterogeneous nanostructures of semiconductor and metal: ZnO nanorods on Ag nanocrystals. *Journal of the American Chemical Society* 2009, **131**(34): 12036-12037.
- [78] Zhou J, Fei P, Gao Y, Gu Y, Liu J, Bao G, Wang ZL. Mechanical– electrical triggers and sensors using piezoelectric micowires/nanowires. *Nano letters* 2008, **8**(9): 2725-2730.
- [79] Souidi A, Khan E, Dickinson J, Gu Y. Observation of unintentionally incorporated nitrogen-related complexes in ZnO and GaN nanowires. *Nano letters* 2009, **9**(5): 1844-1849.

- [80] Yuan Q, Zhao Y-P, Li L, Wang T. Ab initio study of ZnO-based gas-sensing mechanisms: surface reconstruction and charge transfer. *The Journal of Physical Chemistry C* 2009, **113**(15): 6107-6113.
- [81] Wan Q, Li Q, Chen Y, Wang T-H, He X, Li J, Lin C. Fabrication and ethanol sensing characteristics of ZnO nanowire gas sensors. *Applied Physics Letters* 2004, **84**(18): 3654-3656.
- [82] Yang R, Qin Y, Dai L, Wang ZL. Power generation with laterally packaged piezoelectric fine wires. *Nature Nanotechnology* 2009, **4**(1): 34-39.
- [83] Laudise R, Ballman A. Hydrothermal synthesis of zinc oxide and zinc sulfide<sup>1</sup>. *The Journal of Physical Chemistry* 1960, **64**(5): 688-691.
- [84] Vergés MA, Mifsud A, Serna C. Formation of rod-like zinc oxide microcrystals in homogeneous solutions. *Journal of the Chemical Society, Faraday Transactions* 1990, **86**(6): 959-963.
- [85] Vayssieres L, Keis K, Lindquist S-E, Hagfeldt A. Purpose-built anisotropic metal oxide material: 3D highly oriented microrod array of ZnO. *The Journal of Physical Chemistry B* 2001, **105**(17): 3350-3352.
- [86] Pan ZW, Dai ZR, Wang ZL. Nanobelts of semiconducting oxides. *Science* 2001, **291**(5510): 1947-1949.
- [87] Huang MH, Wu Y, Feick H, Tran N, Weber E, Yang P. Catalytic growth of zinc oxide nanowires by vapor transport. *Advanced Materials* 2001, **13**(2): 113-116.
- [88] Yao B, Chan Y, Wang N. Formation of ZnO nanostructures by a simple way of thermal evaporation. *Applied Physics Letters* 2002, **81**(4): 757-759.

- [89] Heo Y, Varadarajan V, Kaufman M, Kim K, Norton D, Ren F, Fleming P. Site-specific growth of ZnO nanorods using catalysis-driven molecular-beam epitaxy. *Applied physics letters* 2002, **81**(16): 3046-3048.
- [90] Sun Y, Fuge GM, Ashfold MN. Growth of aligned ZnO nanorod arrays by catalyst-free pulsed laser deposition methods. *Chemical Physics Letters* 2004, **396**(1): 21-26.
- [91] Hong J-I, Bae J, Wang ZL, Snyder RL. Room-temperature, texture-controlled growth of ZnO thin films and their application for growing aligned ZnO nanowire arrays. *Nanotechnology* 2009, **20**(8): 085609.
- [92] Wu JJ, Wen HI, Tseng CH, Liu SC. Well-Aligned ZnO Nanorods via Hydrogen Treatment of ZnO Films. *Advanced functional materials* 2004, **14**(8): 806-810.
- [93] Yang P, Yan H, Mao S, Russo R, Johnson J, Saykally R, Morris N, Pham J, He R, Choi H-J. Controlled growth of ZnO nanowires and their optical properties. *Advanced Functional Materials* 2002, **12**(5): 323.
- [94] Hecht DS, Hu L, Irvin G. Emerging transparent electrodes based on thin films of carbon nanotubes, graphene, and metallic nanostructures. *Advanced Materials* 2011, **23**(13): 1482-1513.
- [95] Lee J-Y, Connor ST, Cui Y, Peumans P. Solution-processed metal nanowire mesh transparent electrodes. *Nano letters* 2008, **8**(2): 689-692.
- [96] Hu L, Kim HS, Lee J-Y, Peumans P, Cui Y. Scalable coating and properties of transparent, flexible, silver nanowire electrodes. *ACS nano* 2010, **4**(5): 2955-2963.
- [97] Yao S, Zhu Y. Wearable multifunctional sensors using printed stretchable conductors made of silver nanowires. *Nanoscale* 2014, **6**(4): 2345-2352.

- [98] Mock J, Oldenburg S, Smith D, Schultz D, Schultz S. Composite plasmon resonant nanowires. *Nano Letters* 2002, **2**(5): 465-469.
- [99] Wang W, Yang Q, Fan F, Xu H, Wang ZL. Light propagation in curved silver nanowire plasmonic waveguides. *Nano letters* 2011, **11**(4): 1603-1608.
- [100] Kang T, Choi W, Yoon I, Lee H, Seo M-K, Park Q-H, Kim B. Rainbow radiating single-crystal Ag nanowire nanoantenna. *Nano letters* 2012, **12**(5): 2331-2336.
- [101] Sun Y, Yin Y, Mayers BT, Herricks T, Xia Y. Uniform Silver Nanowires Synthesis by Reducing AgNO<sub>3</sub> with Ethylene Glycol in the Presence of Seeds and Poly(Vinyl Pyrrolidone). *Chemistry of Materials* 2002, **14**(11): 4736-4745.
- [102] Qin Q, Yin S, Cheng G, Li X, Chang T-H, Richter G, Zhu Y, Gao H. Recoverable plasticity in penta-twinned metallic nanowires governed by dislocation nucleation and retraction. *Nature communications* 2015, **6**: 5983.
- [103] Zhu Y, Qin Q, Xu F, Fan F, Ding Y, Zhang T, Wiley BJ, Wang ZL. Size effects on elasticity, yielding, and fracture of silver nanowires: In situ experiments. *Physical Review B* 2012, **85**(4): 045443.
- [104] He M-R, Zhu J. Defect-dominated diameter dependence of fracture strength in single-crystalline ZnO nanowires: In situ experiments. *Physical Review B* 2011, **83**(16): 161302(R).
- [105] Zhu Y. In Situ Nanomechanical Testing of Crystalline Nanowires in Electron Microscopes. *JOM* 2015, **68**: 84.
- [106] Narayanan S, Cheng G, Zeng Z, Zhu Y, Zhu T. Strain hardening and size effect in five-fold twinned Ag nanowires. *Nano letters* 2015, **15**(6): 4037-4044.

- [107] Zhu T, Li J. Ultra-strength materials. *Progress in Materials Science* 2010, **55**(7): 710-757.
- [108] Cheng G, Xu W, Wang Y, Misra A, Zhu Y. Grain size effect on radiation tolerance of nanocrystalline Mo. *Scripta Materialia* 2016, **123**: 90-94.
- [109] Brenner SS. TENSILE STRENGTH OF WHISKERS. *Journal of Applied Physics* 1956, **27**(12): 1484-1491.
- [110] Kiener D, Grosinger W, Dehm G, Pippan R. A further step towards an understanding of size-dependent crystal plasticity: In situ tension experiments of miniaturized single-crystal copper samples. *Acta Materialia* 2008, **56**(3): 580-592.
- [111] Brenner S. Plastic deformation of copper and silver whiskers. *Journal of Applied Physics* 1957, **28**(9): 1023-1026.
- [112] Kiener D, Motz C, Schöberl T, Jenko M, Dehm G. Determination of mechanical properties of copper at the micron scale. *Advanced Engineering Materials* 2006, **8**(11): 1119-1125.
- [113] Cheng G, Chang T-H, Qin Q, Huang H, Zhu Y. Mechanical Properties of Silicon Carbide Nanowires: Effect of Size-Dependent Defect Density. *Nano Letters* 2014, **14**(2): 754-758.
- [114] Wong EW, Sheehan PE, Lieber CM. Nanobeam mechanics: Elasticity, strength, and toughness of nanorods and nanotubes. *Science* 1997, **277**(5334): 1971-1975.
- [115] Bayer PD, Cooper RE. Size-Strength Effects in Sapphire and Silicon Nitride Whiskers at 20 degrees C. *Journal of Materials Science* 1967, **2**(3): 233-237.

- [116] Petrovic JJ, Milewski JV, Rohr DL, Gac FD. TENSILE MECHANICAL-PROPERTIES OF SIC WHISKERS. *Journal of Materials Science* 1985, **20**(4): 1167-1177.
- [117] Kirchner HP, Knoll P. SILICON CARBIDE WHISKERS. *Journal of the American Ceramic Society* 1963, **46**(6): 299-300.
- [118] Mehan RL, Herzog JA. In: Levitt AP (ed). *Whisker Technology*. Wiley: New York, 1970, p 169.
- [119] He J, Lilley CM. Surface Effect on the Elastic Behavior of Static Bending Nanowires. *Nano Letters* 2008, **8**(7): 1798-1802.
- [120] Jing GY, Duan HL, Sun XM, Zhang ZS, Xu J, Li YD, Wang JX, Yu DP. Surface effects on elastic properties of silver nanowires: Contact atomic-force microscopy. *Physical Review B* 2006, **73**(23): 235409.
- [121] Song F, Huang G, Park H, Liu X. A continuum model for the mechanical behavior of nanowires including surface and surface-induced initial stresses. *International Journal of Solids and Structures* 2011, **48**(14): 2154-2163.
- [122] Miller RE, Shenoy VB. Size-dependent elastic properties of nanosized structural elements. *Nanotechnology* 2000, **11**(3): 139.
- [123] Zhou L, Huang H. Are surfaces elastically softer or stiffer? *Applied Physics Letters* 2004, **84**(11): 1940-1942.
- [124] Shim HW, Zhou L, Huang H, Cale TS. Nanoplate elasticity under surface reconstruction. *Applied physics letters* 2005, **86**(15): 151912.

- [125] Liang H, Upmanyu M, Huang H. Size-dependent elasticity of nanowires: nonlinear effects. *Physical Review B* 2005, **71**(24): 241403.
- [126] Chang T-H, Cheng G, Li C, Zhu Y. On the size-dependent elasticity of penta-twinned silver nanowires. *Extreme Mechanics Letters* 2016.
- [127] Xu F, Qin Q, Mishra A, Gu Y, Zhu Y. Mechanical Properties of ZnO Nanowires Under Different Loading Modes. *Nano Research* 2010, **3**(4): 271-280.
- [128] Hosford WF. *Mechanical Behavior of Materials*. Cambridge University Press: Cambridge, 2005.
- [129] Lakes R. *Viscoelastic Materials*. Cambridge University Press, 2009.
- [130] Eichler A, Moser J, Chaste J, Zdrojek M, Wilson-Rae I, Bachtold A. Nonlinear damping in mechanical resonators made from carbon nanotubes and graphene. *Nature nanotechnology* 2011, **6**(6): 339-342.
- [131] Zalalutdinov MK, Ray MP, Photiadis DM, Robinson JT, Baldwin JW, Butler JE, Feygelson TI, Pate BB, Houston BH. Ultrathin single crystal diamond nanomechanical dome resonators. *Nano letters* 2011, **11**(10): 4304-4308.
- [132] San Juan J, N6 ML, Schuh CA. Nanoscale shape-memory alloys for ultrahigh mechanical damping. *Nature nanotechnology* 2009, **4**(7): 415-419.
- [133] Tanimoto H, Sakai S, Mizubayashi H. Anelasticity of nanocrystalline metals. *Materials Science and Engineering: A* 2004, **370**(1): 135-141.
- [134] Pan L, Horibe S. Anelastic behaviour of zirconia ceramics under monotonic and cyclic loadings. *Acta materialia* 1997, **45**(2): 463-469.

- [135] Caron A, Kawashima A, Fecht H-J, Louzguine-Luzguin D, Inoue A. On the anelasticity and strain induced structural changes in a Zr-based bulk metallic glass. *Applied Physics Letters* 2011, **99**(17): 171907.
- [136] Schauman.G, Volkl J, Alefeld G. DIFFUSION COEFFICIENTS OF HYDROGEN AND DEUTERIUM IN VANADIUM, NIOBIUM, AND TANTALUM BY GORSKY-EFFECT MEASUREMENTS. *Physica Status Solidi* 1970, **42**(1): 401-+.
- [137] Nowick AS, Berry BS. *Anelastic Relaxation in Crystalline Solids*. Academic Press: New York, 1972.
- [138] Zener C. *Elasticity and anelasticity of metals*. University of Chicago press, 1948.
- [139] Chen B, Gao Q, Wang Y, Liao X, Mai Y-W, Tan HH, Zou J, Ringer SP, Jagadish C. Anelastic Behavior in GaAs Semiconductor Nanowires. *Nano Letters* 2013, **13**(7): 3169-3172.
- [140] Sheng H, Zheng H, Cao F, Wu S, Li L, Liu C, Zhao D, Wang J. Anelasticity of twinned CuO nanowires. *Nano Research* 2015, **8**(11): 3687-3693.
- [141] Wu B, Heidelberg A, Boland JJ. Mechanical properties of ultrahigh-strength gold nanowires. *Nature Materials* 2005, **4**(7): 525-529.
- [142] Chen M, Ma E, Hemker KJ, Sheng H, Wang Y, Cheng X. Deformation twinning in nanocrystalline aluminum. *Science* 2003, **300**(5623): 1275-1277.
- [143] Park HS, Gall K, Zimmerman JA. Deformation of FCC nanowires by twinning and slip. *Journal of the Mechanics and Physics of Solids* 2006, **54**(9): 1862-1881.

- [144] Sedlmayr A, Bitzek E, Gianola DS, Richter G, Mönig R, Kraft O. Existence of two twinning-mediated plastic deformation modes in Au nanowhiskers. *Acta Materialia* 2012, **60**(9): 3985-3993.
- [145] Greer JR, De Hosson JTM. Plasticity in small-sized metallic systems: Intrinsic versus extrinsic size effect. *Progress in Materials Science* 2011, **56**(6): 654-724.
- [146] Yue Y, Liu P, Deng Q, Ma E, Zhang Z, Han X. Quantitative evidence of crossover toward partial dislocation mediated plasticity in copper single crystalline nanowires. *Nano letters* 2012, **12**(8): 4045-4049.
- [147] Zhu YT, Liao XZ, Wu XL. Deformation twinning in nanocrystalline materials. *Progress in Materials Science* 2012, **57**(1): 1-62.
- [148] Cheng G, Yuan H, Jian W, Xu W, Millett P, Zhu Y. Deformation-induced  $\omega$  phase in nanocrystalline Mo. *Scripta Materialia* 2013, **68**(2): 130-133.
- [149] Wang J, Zeng Z, Weinberger CR, Zhang Z, Zhu T, Mao SX. In situ atomic-scale observation of twinning-dominated deformation in nanoscale body-centred cubic tungsten. *Nature materials* 2015, **14**(6): 594-600.
- [150] Seo J-H, Park HS, Yoo Y, Seong T-Y, Li J, Ahn J-P, Kim B, Choi I-S. Origin of size dependency in coherent-twin-propagation-mediated tensile deformation of noble metal nanowires. *Nano letters* 2013, **13**(11): 5112-5116.
- [151] Hwang B, Kang M, Lee S, Weinberger CR, Loya P, Lou J, Oh SH, Kim B, Han SM. Effect of surface energy on size-dependent deformation twinning of defect-free Au nanowires. *Nanoscale* 2015, **7**(38): 15657-15664.

- [152] Seo J-H, Yoo Y, Park N-Y, Yoon S-W, Lee H, Han S, Lee S-W, Seong T-Y, Lee S-C, Lee K-B, Cha P-R, Park HS, Kim B, Ahn J-P. Superplastic Deformation of Defect-Free Au Nanowires via Coherent Twin Propagation. *Nano Letters* 2011, **11**(8): 3499-3502.
- [153] Weinberger CR, Cai W. Plasticity of metal nanowires. *Journal of Materials Chemistry* 2012, **22**(8): 3277-3292.
- [154] Lee S, Im J, Yoo Y, Bitzek E, Kiener D, Richter G, Kim B, Oh SH. Reversible cyclic deformation mechanism of gold nanowires by twinning–detwinning transition evidenced from in situ TEM. *Nature communications* 2014, **5**: 3033.
- [155] Jang D, Li X, Gao H, Greer JR. Deformation mechanisms in nanotwinned metal nanopillars. *Nature Nanotechnology* 2012, **7**(9): 594-601.
- [156] Deng C, Sansoz F. Fundamental differences in the plasticity of periodically twinned nanowires in Au, Ag, Al, Cu, Pb and Ni. *Acta Materialia* 2009, **57**(20): 6090-6101.
- [157] Filleter T, Ryu S, Kang K, Yin J, Bernal RA, Sohn K, Li S, Huang J, Cai W, Espinosa HD. Nucleation-Controlled Distributed Plasticity in Penta-twinned Silver Nanowires. *Small* 2012, **8**(19): 2986-2993.
- [158] Lu Y, Song J, Huang JY, Lou J. Fracture of Sub-20nm Ultrathin Gold Nanowires. *Advanced Functional Materials* 2011, **21**(20): 3982-3989.
- [159] Wang J, Sansoz F, Huang J, Liu Y, Sun S, Zhang Z, Mao SX. Near-ideal theoretical strength in gold nanowires containing angstrom scale twins. *Nature communications* 2013, **4**: 1742.

- [160] Baker SP, Vinci RP, Arias T. Elastic and anelastic behavior of materials in small dimensions. *Mrs Bulletin* 2002, **27**(1): 26-29.
- [161] Choi DH, Kim H, Nix WD. Anelasticity and damping of thin aluminum films on silicon substrates. *Journal of Microelectromechanical Systems* 2004, **13**(2): 230-237.
- [162] Haque MA, Saif MTA. Thermo-mechanical properties of nano-scale freestanding aluminum films. *Thin Solid Films* 2005, **484**(1-2): 364-368.
- [163] Karanjgaokar NJ, Oh CS, Lambros J, Chasiotis I. Inelastic deformation of nanocrystalline Au thin films as a function of temperature and strain rate. *Acta Materialia* 2012, **60**(13-14): 5352-5361.
- [164] Lang MJ, Duarte-Dominguez M, Birringer R, Hempelmann R, Natter H, Arnold W. Measurement of elastic and anelastic properties of nanocrystalline metals. *Nanostructured Materials* 1999, **12**(5-8): 811-816.
- [165] Li X, Wei Y, Yang W, Gao H. Competing grain-boundary- and dislocation-mediated mechanisms in plastic strain recovery in nanocrystalline aluminum. *Proceedings of the National Academy of Sciences* 2009, **106**(38): 16108-16113.
- [166] Rajagopalan J, Han JH, Saif MTA. Plastic deformation recovery in freestanding nanocrystalline aluminum and gold thin films. *Science* 2007, **315**(5820): 1831-1834.
- [167] Wei X, Kysar JW. Residual plastic strain recovery driven by grain boundary diffusion in nanocrystalline thin films. *Acta Materialia* 2011, **59**(10): 3937-3945.
- [168] Wei Y, Bower AF, Gao H. Recoverable creep deformation due to heterogeneous grain-boundary diffusion and sliding. *Scripta Materialia* 2007, **57**(10): 933-936.

- [169] Wei Y, Bower AF, Gao H. Recoverable creep deformation and transient local stress concentration due to heterogeneous grain-boundary diffusion and sliding in polycrystalline solids. *Journal of the Mechanics and Physics of Solids* 2008, **56**(4): 1460-1483.
- [170] Yamakov V, Wolf D, Phillpot SR, Mukherjee AK, Gleiter H. Dislocation processes in the deformation of nanocrystalline aluminium by molecular-dynamics simulation. *Nature Materials* 2002, **1**(1): 45-49.
- [171] Diao J, Gall K, Dunn ML. Surface-stress-induced phase transformation in metal nanowires. *Nature Materials* 2003, **2**(10): 656-660.
- [172] Liang W, Srolovitz DJ, Zhou M. A micromechanical continuum model for the tensile behavior of shape memory metal nanowires. *Journal of the Mechanics and Physics of Solids* 2007, **55**(8): 1729-1761.
- [173] Liang W, Zhou M. Atomistic simulations reveal shape memory of fcc metal nanowires. *Physical Review B* 2006, **73**(11): 115409.
- [174] Park HS, Gall K, Zimmerman JA. Shape memory and pseudoelasticity in metal nanowires. *Physical Review Letters* 2005, **95**(25): 255504.
- [175] Lu Y, Huang JY, Wang C, Sun S, Lou J. Cold welding of ultrathin gold nanowires. *Nature nanotechnology* 2010, **5**(3): 218-224.
- [176] Zheng H, Cao A, Weinberger CR, Huang JY, Du K, Wang J, Ma Y, Xia Y, Mao SX. Discrete plasticity in sub-10-nm-sized gold crystals. *Nature communications* 2010, **1**: 144.

- [177] Zhu T, Li J, Samanta A, Leach A, Gall K. Temperature and strain-rate dependence of surface dislocation nucleation. *Physical Review Letters* 2008, **100**(2): 025502.
- [178] Roos B, Kapelle B, Richter G, Volkert C. Surface dislocation nucleation controlled deformation of Au nanowires. *Applied Physics Letters* 2014, **105**(20): 201908.
- [179] Cheng G, Jian W, Xu W, Yuan H, Millett P, Zhu Y. Grain Size Effect on Deformation Mechanisms of Nanocrystalline bcc Metals. *Material Research Letters* 2013, **1**(1): 26-31.
- [180] Cheng G, Xu W, Jian W, Yuan H, Tsai M, Zhu Y, Zhang Y, Millett P. Dislocations with edge components in nanocrystalline bcc Mo. *Journal of Materials Research* 2013, **28**(13): 1820-1826.
- [181] Jian WW, Cheng GM, Xu WZ, Koch CC, Wang QD, Zhu YT, Mathaudhu SN. Physics and model of strengthening by parallel stacking faults. *Applied Physics Letters* 2013, **103**: 133108.
- [182] Bernal RA, Aghaei A, Lee S, Ryu S, Sohn K, Huang J, Cai W, Espinosa H. Intrinsic Bauschinger Effect and Recoverable Plasticity in Pentatwinned Silver Nanowires Tested in Tension. *Nano Letters* 2015, **15**(1): 139-146.
- [183] Gane N, Bowden F. Microdeformation of solids. *Journal of Applied Physics* 1968, **39**(3): 1432-1435.
- [184] Gane N. The direct measurement of the strength of metals on a sub-micrometre scale. *Proceedings of the Royal Society of London A: Mathematical, Physical and Engineering Sciences*; 1970: The Royal Society; 1970. p. 367-391.

- [185] Wang YB, Wang LF, Joyce HJ, Gao Q, Liao XZ, Mai YW, Tan HH, Zou J, Ringer SP, Gao HJ. Super deformability and Young's modulus of GaAs nanowires. *Advanced Materials* 2011, **23**(11): 1356-1360.
- [186] Minor AM, Asif SS, Shan Z, Stach EA, Cyrankowski E, Wyrobek TJ, Warren OL. A new view of the onset of plasticity during the nanoindentation of aluminium. *Nature materials* 2006, **5**(9): 697-702.
- [187] Shan Z, Mishra RK, Asif SS, Warren OL, Minor AM. Mechanical annealing and source-limited deformation in submicrometre-diameter Ni crystals. *Nature materials* 2008, **7**(2): 115-119.
- [188] Nowak R, Chrobak D, Nagao S, Vodnick D, Berg M, Tukiainen A, Pessa M. An electric current spike linked to nanoscale plasticity. *Nature Nanotechnology* 2009, **4**(5): 287-291.
- [189] Huang JY, Zheng H, Mao S, Li Q, Wang GT. In situ nanomechanics of GaN nanowires. *Nano letters* 2011, **11**(4): 1618-1622.
- [190] Kiener D, Minor AM. Source Truncation and Exhaustion: Insights from Quantitative in situ TEM Tensile Testing. *Nano Letters* 2011, **11**(9): 3816-3820.
- [191] Guo H, Chen K, Oh Y, Wang K, Dejoie C, Syed Asif S, Warren O, Shan Z, Wu J, Minor A. Mechanics and dynamics of the strain-induced M1–M2 structural phase transition in individual VO<sub>2</sub> nanowires. *Nano letters* 2011, **11**(8): 3207-3213.
- [192] Wu B, Heidelberg A, Boland JJ, Sader JE, Sun X, Li Y. Microstructure-hardened silver nanowires. *Nano letters* 2006, **6**(3): 468-472.

- [193] Celik E, Guven I, Madenci E. Mechanical characterization of nickel nanowires by using a customized atomic force microscope. *Nanotechnology* 2011, **22**(15): 155702.
- [194] Rabe R, Breguet J-M, Schwaller P, Stauss S, Haug F-J, Patscheider J, Michler J. Observation of fracture and plastic deformation during indentation and scratching inside the scanning electron microscope. *Thin Solid Films* 2004, **469**: 206-213.
- [195] Lu Y, Ganesan Y, Lou J. A multi-step method for in situ mechanical characterization of 1-D nanostructures using a novel micromechanical device. *Experimental mechanics* 2010, **50**(1): 47-54.
- [196] Peng C, Zhan Y, Lou J. Size-Dependent Fracture Mode Transition in Copper Nanowires. *Small* 2012, **8**(12): 1889-1894.
- [197] Peng C, Ganesan Y, Lu Y, Lou J. Size dependent mechanical properties of single crystalline nickel nanowires. *Journal of Applied Physics* 2012, **111**(6): 063524.
- [198] PI 95 TEM PicoIndenter User Manual, Hysitron Incorporated. 2011.
- [199] Nakabayashi D, Silva P, Ugarte D. Inexpensive two-tip nanomanipulator for a SEM. *Applied Surface Science* 2007, **254**(1): 405-411.
- [200] He M-R, Shi Y, Zhou W, Chen J, Yan Y, Zhu J. Diameter dependence of modulus in zinc oxide nanowires and the effect of loading mode: In situ experiments and universal core-shell approach. *Applied Physics Letters* 2009, **95**(9): 091912.
- [201] Ke C, Zheng M, Zhou G, Cui W, Pugno N, Miles RN. Mechanical Peeling of Free-Standing Single-Walled Carbon-Nanotube Bundles. *small* 2010, **6**(3): 438-445.

- [202] Zhu Y, Espinosa HD. An electromechanical material testing system for in situ electron microscopy and applications. *Proceedings of the National Academy of Sciences of the United States of America* 2005, **102**(41): 14503-14508.
- [203] Li X, Ling X, Sun L, Liu L, Zeng D, Zheng Q. Measurement of mechanical properties of one-dimensional nanostructures with combined multi-probe platform. *Composites Part B: Engineering* 2012, **43**(1): 70-75.
- [204] Yu M-F, Lourie O, Dyer MJ, Moloni K, Kelly TF, Ruoff RS. Strength and breaking mechanism of multiwalled carbon nanotubes under tensile load. *Science* 2000, **287**(5453): 637-640.
- [205] Kaplan-Ashiri I, Cohen SR, Gartsman K, Ivanovskaya V, Heine T, Seifert G, Wiesel I, Wagner HD, Tenne R. On the mechanical behavior of WS<sub>2</sub> nanotubes under axial tension and compression. *Proceedings of the National Academy of Sciences of the United States of America* 2006, **103**(3): 523-528.
- [206] Ding W, Calabri L, Chen X, Kohlhaas KM, Ruoff RS. Mechanics of crystalline boron nanowires. *Composites Science and Technology* 2006, **66**(9): 1112-1124.
- [207] Gianola DS, Sedlmayr A, Mönig R, Volkert CA, Major RC, Cyrankowski E, Asif S, Warren OL, Kraft O. In situ nanomechanical testing in focused ion beam and scanning electron microscopes. *Review of Scientific Instruments* 2011, **82**(6): 063901.
- [208] Manoharan M, Desai A, Neely G, Haque M. Synthesis and elastic characterization of zinc oxide nanowires. *Journal of Nanomaterials* 2008, **2008**: 49.
- [209] Chen C, Zhu J. Bending strength and flexibility of ZnO nanowires. *Applied physics letters* 2007, **90**(4): 3105.

- [210] Han JH, Saif MTA. In situ microtensile stage for electromechanical characterization of nanoscale freestanding films. *Review of Scientific Instruments* 2006, **77**(4): 045102.
- [211] Kang W, Saif MTA. A novel SiC MEMS apparatus for in situ uniaxial testing of micro/nanomaterials at high temperature. *Journal of Micromechanics and Microengineering* 2011, **21**(10): 105017.
- [212] Desai A, Haque M. Mechanical properties of ZnO nanowires. *Sensors and Actuators A: Physical* 2007, **134**(1): 169-176.
- [213] Haque M, Saif M. Application of MEMS force sensors for in situ mechanical characterization of nano-scale thin films in SEM and TEM. *Sensors and Actuators A: Physical* 2002, **97**: 239-245.
- [214] Guan C, Zhu Y. An electrothermal microactuator with Z-shaped beams. *Journal of Micromechanics and Microengineering* 2010, **20**(8): 085014.
- [215] Kumar S, Alam MT, Haque M. Fatigue insensitivity of nanoscale freestanding aluminum films. *Journal of Microelectromechanical Systems* 2011, **20**(1): 53-58.
- [216] Brown J, Baca A, Bertness K, Dikin D, Ruoff R, Bright V. Tensile measurement of single crystal gallium nitride nanowires on MEMS test stages. *Sensors and Actuators A: Physical* 2011, **166**(2): 177-186.
- [217] Qin Q, Zhu Y. Temperature control in thermal microactuators with applications to in-situ nanomechanical testing. *Applied Physics Letters* 2013, **102**(1): 013101-013101-013105.

- [218] Kearney SP, Phinney LM, Baker MS. Spatially resolved temperature mapping of electrothermal actuators by surface Raman scattering. *Journal of Microelectromechanical Systems* 2006, **15**(2): 314-321.
- [219] Pant B, Choi S, Baumert E, Allen B, Graham S, Gall K, Pierron O. MEMS-based nanomechanics: influence of MEMS design on test temperature. *Experimental mechanics* 2012, **52**(6): 607-617.
- [220] Chang T-H, Zhu Y. A microelectromechanical system for thermomechanical testing of nanostructures. *Applied Physics Letters* 2013, **103**(26): 263114.
- [221] Zhang D, Breguet J-M, Clavel R, Sivakov V, Christiansen S, Michler J. In situ electron microscopy mechanical testing of silicon nanowires using electrostatically actuated tensile stages. *Journal of Microelectromechanical Systems* 2010, **19**(3): 663-674.
- [222] Zhu Y, Chang T-H. A review of microelectromechanical systems for nanoscale mechanical characterization. *Journal of Micromechanics and Microengineering* 2015, **25**(9): 093001.
- [223] Kang W, Saif MTA. In Situ Study of Size and Temperature Dependent Brittle-to-Ductile Transition in Single Crystal Silicon. *Advanced Functional Materials* 2013, **23**(6): 713-719.
- [224] Zhang Y, Han X, Zheng K, Zhang Z, Zhang X, Fu J, Ji Y, Hao Y, Guo X, Wang Z. Direct observation of super-plasticity of beta-SiC nanowires at low temperature. *Advanced Functional Materials* 2007, **17**(17): 3435-3440.

- [225] Wang ZG, Li JB, Gao F, Weber WJ. Tensile and compressive mechanical behavior of twinned silicon carbide nanowires. *Acta Materialia* 2010, **58**(6): 1963-1971.
- [226] Wang J, Lu C, Wang Q, Xiao P, Ke F, Bai Y, Shen Y, Liao X, Gao H. Influence of microstructures on mechanical behaviours of SiC nanowires: a molecular dynamics study. *Nanotechnology* 2012, **23**(2): 025703.
- [227] Gouadec G, Colomban P. Raman Spectroscopy of nanomaterials: How spectra relate to disorder, particle size and mechanical properties. *Progress in Crystal Growth and Characterization of Materials* 2007, **53**(1): 1-56.
- [228] Zhu Y, Moldovan N, Espinosa HD. A microelectromechanical load sensor for in situ electron and x-ray microscopy tensile testing of nanostructures. *Applied physics letters* 2005, **86**(1): 013506.
- [229] Zhang D, Breguet J-M, Clavel R, Sivakov V, Christiansen S, Michler J. Electron Microscopy Mechanical Testing of Silicon Nanowires Using Electrostatically Actuated Tensile Stages. *Journal of Microelectromechanical Systems* 2010, **19**(3): 663-674.
- [230] Li Z, Wang S, Wang Z, Zu X, Gao F, Weber WJ. Mechanical behavior of twinned SiC nanowires under combined tension-torsion and compression-torsion strain. *Journal of Applied Physics* 2010, **108**(1): 013504.
- [231] Kim TY, Han SS, Lee HM. Nanomechanical behavior of beta-SiC nanowire in tension: Molecular dynamics simulations. *Materials Transactions* 2004, **45**(5): 1442-1449.

- [232] Lifshitz R, Roukes ML. Thermoelastic damping in micro- and nanomechanical systems. *Physical Review B* 2000, **61**(8): 5600-5609.
- [233] Schauman.G, Volkl J, Alefeld G. RELAXATION PROCESS DUE TO LONG-RANGE DIFFUSION OF HYDROGEN AND DEUTERIUM IN NIOBIUM. *Physical Review Letters* 1968, **21**(13): 891-&.
- [234] McCluskey MD, Jokela SJ. Defects in ZnO. *Journal of Applied Physics* 2009, **106**(7): 071101.
- [235] Zhang X, Kulik J, Dickey EC. Diffusion in SixGe1-x/Si nanowire heterostructures. *Journal of Nanoscience and Nanotechnology* 2007, **7**(2): 717-720.
- [236] Janotti A, Van de Walle CG. Native point defects in ZnO. *Physical Review B* 2007, **76**(16): 165202.
- [237] Ashby MF. *Materials Selection in Mechanical Design*: Butterworth-Heinemann, 2010.
- [238] Perea DE, Hemesath ER, Schwalbach EJ, Lensch-Falk JL, Voorhees PW, Lauhon LJ. Direct measurement of dopant distribution in an individual vapour-liquid-solid nanowire. *Nature Nanotechnology* 2009, **4**(5): 315-319.
- [239] Wang XD, Song JH, Li P, Ryou JH, Dupuis RD, Summers CJ, Wang ZL. Growth of uniformly aligned ZnO nanowire heterojunction arrays on GaN, AlN, and Al<sub>0.5</sub>Ga<sub>0.5</sub>N substrates. *Journal of the American Chemical Society* 2005, **127**(21): 7920-7923.
- [240] Wu Z, Zhang Y-W, Jhon MH, Gao H, Srolovitz DJ. Nanowire failure: long= brittle and short= ductile. *Nano letters* 2012, **12**(2): 910-914.

- [241] Lopez FJ, Hemesath ER, Lauhon LJ. Ordered Stacking Fault Arrays in Silicon Nanowires. *Nano Letters* 2009, **9**(7): 2774-2779.
- [242] Li X, Wei Y, Lu L, Lu K, Gao H. Dislocation nucleation governed softening and maximum strength in nano-twinned metals. *Nature* 2010, **464**(7290): 877-880.
- [243] Lu K, Lu L, Suresh S. Strengthening materials by engineering coherent internal boundaries at the nanoscale. *Science* 2009, **324**(5925): 349-352.
- [244] Kobler A, Beuth T, Klöffel T, Prang R, Moosmann M, Scherer T, Walheim S, Hahn H, Kübel C, Meyer B, Schimmel T, Bitzek E. Nanotwinned silver nanowires: Structure and mechanical properties. *Acta Materialia* 2015, **92**: 299-308.
- [245] Wang J, Huang H. Novel deformation mechanism of twinned nanowires. *Applied Physics Letters* 2006, **88**(20): 203112.
- [246] Monk J, Hoyt JJ, Farkas D. Metastability of multitwinned Ag nanorods: Molecular dynamics study. *Physical Review B* 2008, **78**(2): 024112.
- [247] Cheng G, Yao S, Sang X, Hao B, Zhang D, Yap YK, Zhu Y. Evolution of Irradiation-Induced Vacancy Defects in Boron Nitride Nanotubes. *Small* 2016, **12**(6): 818–824.
- [248] Xu W, Zhang Y, Cheng G, Jian W, Millett P, Koch C, Mathaudhu S, Zhu Y. Dynamic Void Growth and Shrinkage in Mg under Electron Irradiation. *Materials Research Letters* 2014, **2**(3): 176-183.
- [249] Xu W, Zhang Y, Cheng G, Jian W, Millett PC, Koch CC, Mathaudhu SN, Zhu Y. In-situ atomic-scale observation of irradiation-induced void formation. *Nature Communications* 2013, **4**: 2288.

- [250] Plimpton S. Fast Parallel Algorithms for Short-Range Molecular-Dynamics. *J Comput Phys* 1995, **117**(1): 1-19.
- [251] Williams PL, Mishin Y, Hamilton JC. An embedded-atom potential for the Cu-Ag system. *Modelling and Simulation in Materials Science and Engineering* 2006, **14**(5): 817-833.
- [252] Nose S. A Unified Formulation of the Constant Temperature Molecular-Dynamics Methods. *J Chem Phys* 1984, **81**(1): 511-519.
- [253] Stukowski A. Visualization and analysis of atomistic simulation data with OVITO- the Open Visualization Tool. *Modelling and Simulation in Materials Science and Engineering* 2010, **18**(1): 015012.
- [254] Zhu YT, Liao XZ, Wu XL, Narayan J. Grain size effect on deformation twinning and detwinning. *Journal of Materials Science* 2013, **48**(13): 4467-4475.
- [255] Wang J, Li N, Anderoglu O, Zhang X, Misra A, Huang JY, Hirth JP. Detwinning mechanisms for growth twins in face-centered cubic metals. *Acta Materialia* 2010, **58**(6): 2262-2270.
- [256] Bernstein N, Tadmor E. Tight-binding calculations of stacking energies and twinnability in fcc metals. *Physical Review B* 2004, **69**(9): 094116.
- [257] Ju S, Facchetti A, Xuan Y, Liu J, Ishikawa F, Ye P, Zhou C, Marks TJ, Janes DB. Fabrication of fully transparent nanowire transistors for transparent and flexible electronics. *Nature nanotechnology* 2007, **2**(6): 378-384.

- [258] Wang J, Tian M, Mallouk TE, Chan MH. Microtwinning in template-synthesized single-crystal metal nanowires. *The Journal of Physical Chemistry B* 2004, **108**(3): 841-845.
- [259] Deng C, Sansoz F. Repulsive force of twin boundary on curved dislocations and its role on the yielding of twinned nanowires. *Scripta Materialia* 2010, **63**(1): 50-53.
- [260] Campbell GH, McKeown JT, Santala MK. Time resolved electron microscopy for in situ experiments. *Applied Physics Reviews* 2014, **1**(4): 041101.
- [261] Gao Z, Ding Y, Lin S, Hao Y, Wang ZL. Dynamic fatigue studies of ZnO nanowires by in-situ transmission electron microscopy. *physica status solidi (RRL)-Rapid Research Letters* 2009, **3**(7-8): 260-262.
- [262] Bufford DC, Stauffer D, Mook WM, Syed Asif SA, Boyce BL, Hattar K. High Cycle Fatigue in the Transmission Electron Microscope. *Nano Letters* 2016, **16**(8): 4946-4953.
- [263] Ramachandramoorthy R, Gao W, Bernal R, Espinosa H. High Strain Rate Tensile Testing of Silver Nanowires: Rate-Dependent Brittle-to-Ductile Transition. *Nano Letters* 2016, **16**(1): 255-263.
- [264] Bernal RA, Filleter T, Connell JG, Sohn K, Huang J, Lauhon LJ, Espinosa HD. In Situ Electron Microscopy Four-Point Electromechanical Characterization of Freestanding Metallic and Semiconducting Nanowires. *Small* 2014, **10**(4): 725-733.
- [265] Espinosa HD, Bernal RA, Filleter T. In Situ TEM Electromechanical Testing of Nanowires and Nanotubes. *Small* 2012, **8**(21): 3233-3252.